Università Politecnica delle Marche

Research Doctorate in Life and Environmental Sciences

Curriculum of Biomolecular Sciences

Cycle XXX

Development of new molecular tools for the characterization of human Granulosa cells: new implications for the research on human infertility

Supervisor:

Prof. Elisabetta Giorgini

Co-Supervisor:

Dr. Giorgia Gioacchini

Company Supervisor:

Dr. Andrea Borini

PhD candidate:

Valentina Notarstefano

Supervisor

Prof. Elisabetta Giorgini, PhD

Laboratory of Infrared Spectroscopy

Department of Life and Environmental Sciences

Università Politecnica delle Marche

Ancona, Italy

Co-Supervisor

Dr. Giorgia Gioacchini, PhD

Laboratory of Developmental and Reproductive Biology

Department of Life and Environmental Sciences

Università Politecnica delle Marche

Ancona, Italy

Company Supervisor

Dr. Andrea Borini, PhD, MD

9.baby Family and Fertility Center

Bologna, Italy

A. E. G.

Vis unita fortior

CONTENTS

SUMMARY

Granulosa cells (GCs) play several key roles in folliculogenesis, such as the production of estradiol during follicular growth, the regulation of the advance of meiosis steps and the transcriptional activity in the oocyte, the production of essential nutrients used as energy source during oocyte maturation, the accumulation of secreted metabolites, and the secretion of progesterone after ovulation.

The aim of the PhD project was to investigate human GCs in a multidisciplinary approach, in order to correlate the information on these cells to several aspects related to infertility, to improve the knowledge on mechanisms involved in folliculogenesis and ovarian functions and understand how these processes are impaired by endogenous and exogenous factors.

For all the studies, luteinized GCs were retrieved from patients enrolled in an *in vitro* fertilization program, at Tecnobios Procreazione Fertility Center. The work was organised in seven steps, including establishing protocols, as the basis of targeted studies.

I. Fourier Transform InfraRed Microspectroscopy (FTIRM) analysis of Granulosa Cells: a promising approach for the assessment of good quality human oocytes. The aim of the present section was to find an innovative method for evaluating the quality of human oocytes, by studying GCs. To do this, 55 GCs samples, retrieved from consenting patients, were subjected to FTIRM measurements. IR data were pre-processed and then analysed using 'feature selection' procedures and

univariate/multivariate statistical analyses. Four experimental groups were selected: CP (clinical pregnancy), GCs from oocytes, which gave clinical pregnancy; FF (fertilization fail), GCs from oocytes, which failed fertilization; EDF (embryo development fail), GCs from oocytes, which failed embryo development, and IF (implantation fail), GCs from oocytes, which failed implantation. The 'feature selection' procedures allowed the identification of 17 spectral biomarkers, which showed to be correlated with the corresponding oocyte clinical outcome in an accurate and reliable way.

II. Validation of air-dehydration protocol of GCs for FTIRM. The aim of the present section was to establish a reliable preparation protocol for GCs for FTIRM studies, based on air-drying of GCs on CaF_2 supports. To do this, FTIRM measurements were performed on GCs, and second derivative spectra of 'wet' (analysed in physiological condition in a microfluidic device) and 'dried' (deposited onto CaF_2 supports and air-dried for 30min) GCs were compared. A satisfactory correspondence in the spectral profile was observed, proving that the air-dehydration protocol is a suitable method to prepare GCs for FTIRM analysis.

III. Metabolic changes in cultured hGCs: an innovative FTIRM approach. The aim of the present section was the evaluation of the biochemical alterations induced by *in vitro* culture in GCs. FTIRM measurements were performed on GCs collected from 17 patients immediately after their collection and cultured for 24–48–96 h. the results obtained from FTIRM data showed that lipid metabolism was altered in all cultured

GCs, in terms of total content of triglycerides and fatty acids; also, the amount of phosphorylation was altered. Proteins and carbohydrates, in contrast, were not affected.

IV. A new insight on aging effects in human Granulosa cells: a multidisciplinary FTIR and qPCR approach. The aim was to analyse the biochemical modifications induced by aging on GCs. FTIRM was performed on air-dried GCs divided into two groups: Young (31.2±2.20; n°10) and Old (42.5±1.84; n°10). The results obtained showed that aging affects the biochemical composition of GCs, evidencing a process of age-related oxidative stress: increased lipid content, C=O ester moieties, and =CH groups; decreased protein content, and impaired secondary structure. Results of gene expression analysis were consistent with IR data: an increase of *igfbp3*, *foxo3*, and a decrease of *igf1*, *sirt1* and *sod2* was found.

V. Ovarian endometriosis affects Granulosa Cells Endocannabinoid system (ECS). The aim of the present work was to analyse the expression of molecules associated with the ECS in GCs from patients affected by ovarian endometriosis. To do this, FTIR imaging and quantitative PCR (qPCR) were performed, on GCs previously divided into two groups: CTRL (n°10; women with non-ovarian infertility) and ENDO (n°10; women with ovarian endometriosis). The obtained results showed that endometriosis alters the gene expression of several molecules involved in ECS (*trpv1*, *gpr55*, *cnr1, cnr2*, *nape-pld*, *faah*), and impairs lipid (*pparα*, *pparγ*, *srebp1*, *fasn*) and carbohydrate (*glut1*

and *glut9*) metabolisms. FTIR imaging confirmed the alterations in GCs metabolism.

VI. Could unilateral ovarian endometriosis affect the contralateral ovary? New insights from a multidisciplinary study. The aim was to evaluate how unilateral ovarian endometriosis (UOE) affects the functionality of both the ovaries. FTIRM, Raman MicroSpectroscopy (RMS) and qPCR were performed on GCs previously divided into three groups: CTRL (GCs from 10 healthy women), CONTRAL (GCs from contralateral ovary of 10 women with UOE;) and ENDO (GCs from affected ovary of 10 women with UOE;). FTIRM and RMS data consistently revealed alterations, in both the ovaries, in lipid content and characteristics, protein composition and secondary structure, carbohydrates, and nucleic acids. qPCR confirmed an impairment of lipid (*ppar*α, *ppar*γ and *fasn* increase) and carbohydrate (*glut1* and *glut9* decrease) metabolisms, and methylation process (*dnmt1* and *dnmt3a* increase), in both the ovaries.

VII. How do plasticizers BPA and DGB alter the macromolecular composition of luteinized GCs? The aim was the investigation of the effects of bisphenol-A (BPA) and diethylene glycol dibenzoate (DGB) (1–10–100ng/ml), on GCs. FTIRM measurements were performed on GCs (n°15 women, 32±3.3 years), treated with BPA/DGB for 48h, and air-dried for IR measurements. The results showed that BPA exposure affected the biochemical composition of GCs, in terms of lipids amount and characteristics; proteins decreased and showed

different amino acid composition; phosphate groups from phospholipids and nucleic acids increased. DGB impacts on GCs differently: unsaturation and esterification rates in lipids decreased; proteins and phosphates amounts were altered differently according to dose.

The information obtained on GCs contribute to the understanding of the mechanisms of impairment of folliculogenesis, by a multidisciplinary approach that mainly consisted of supporting spectroscopic analysis with standard qPCR. Thanks to the results, an innovative approach to evaluate oocyte quality by spectral features of GCs was proposed, suggesting the reliability of FTIRM as a clinical feasible and easy diagnostic tool in assisted reproduction routine, in a possible near future.

SOMMARIO

Le cellule della Granulosa (GCs) svolgono molti fondamentali chiave durante il processo della follicologenesi: ad esempio, sono coinvolte nella produzione di estradiolo durante la crescita follicolare, nella regolazione dell'avanzamento degli step della meiosi e dell'attività trascrizionale dell'ovocita, nella produzione di nutrienti essenziali usati come fonte energetica durante la maturazione dell'ovocita, nell'accumulo di metaboliti secreti dall'ovocita, e nella secrezione di progesterone dopo l'ovulazione.

Lo scopo del presente progetto di Dottorato è stato quello di analizzare le GCs umane applicando un approccio multidisciplinare, che correlasse le informazioni ottenute su queste cellule con diversi aspetti legati all'infertilità, per fornire nuove informazioni sui meccanismi coinvolti nella follicologenesi e nelle funzioni ovariche, e per comprendere se e come questi processi possono essere alterati da fattori endogeni ed esogeni.

Per tutti gli studi condotti, le GCs luteinizzate sono state recuperate da pazienti reclutate in un programma di fecondazione *in vitro* presso il centro per la fertilità Tecnobios Procreazione. Il lavoro è stato organizzato in sette step, a partire dalla definizione dei protocolli, fino agli studi applicati.

I. Fourier Transform InfraRed Microspectroscopy (FTIRM) analysis of Granulosa Cells: a promising approach for the assessment of good quality human oocytes. (Analisi tramite Fourier Transform InfraRed Microspectroscopy (FTIRM) delle cellule della Granulosa: un approccio promettente per la valutazione della qualità degli ovociti

umani). Lo scopo di questa sezione era trovare un metodo innovativo per valutare la qualità degli ovociti umani. 55 campioni di GCs sono stati analizzati tramite FTIRM; i dati ottenuti sono stati processati e, tramite delle procedure di 'feature selection', è stata ottenuta la 'biomarker signature' del sistema analizzato. Infine, l'applicazione di metodi di statistica multivariata ha permesso di validare il modello, mentre la statistica univariata è stata utilizzata per investigare ulteriormente il significato biologico dei biomarker spettrali individuati. Sono stati selezionati quattro gruppi sperimentali: **CP** (clinical pregnancy), GCs da ovociti che hanno portato a gravidanza clinica; **FF** (fertilization fail), GCs da ovociti che non sono stati fecondati; **EDF** (embryo development fail), GCs da ovociti che non si sono sviluppati correttamente in embrioni; **IF** (implantation fail), GCs da ovociti che si sono sviluppati in embrioni, ma che hanno fallito l'impianto. Correlando le informazioni spettrali ottenute dall'analisi delle GCs con l'esito clinico dell'ovocita corrispondente, sono stati identificati 17 biomarker spettrali, che si sono rivelati in grado di correlare le GCs con la qualità degli ovociti in maniera accurata e affidabile.

II. Validation of air-dehydration protocol of GCs for FTIRM. (Validazione di un protocollo di disidratazione all'aria delle GCs per la valutazione tramite FTIRM). Lo scopo di questa sezione era quello di stabilire un protocollo affidabile per la preparazione delle GCs per l'analisi tramite FTIRM (Microspettroscopia FTIR), basato sulla

disidratazione delle cellule all'aria su finestre ottiche di CaF_2. Per far questo, sono stati confrontati gli spettri in derivata seconda delle GCs 'wet' (analizzate in condizioni fisiologiche grazie all'utilizzo di in dispositivo di microfluidica) e 'dried' (depositate su supporti di CaF_2 e lasciate disidratare all'aria per 30 minuti). È stata osservata una soddisfacente corrispondenza fra i profili spettrali di GCs 'wet' e 'dried', suggerendo che il protocollo di disidratazione all'aria delle GCs può essere considerato in metodo adeguato per le analisi tramite FTIRM.

III. Metabolic changes in cultured hGCs: an innovative FTIRM approach. (Alterazioni metaboliche in GCs umane mantenute in coltura: un innovativo approccio con FTIRM). Lo scopo della presente sezione era stabilire se la coltura *in vitro* delle GCs in coltura potesse determinare nelle cellule delle alterazioni biochimiche. Per fare questo, le GCs sono state prelevate da 17 pazienti consenzienti e sono state analizzate tramite FTIRM immediatamente dopo il pick-up, o dopo coltura per 24, 48 e 96 ore. L'analisi spettrale ha rivelato come a tutti i tempi di coltura, le GCs mostravano un'alterazione del metabolismo lipidico, in termini di contenuto totale di trigliceridi e acidi grassi; inoltre, il tasso di fosforilazione risultava alterato. Al contrario, il mantenimento in coltura delle GCs non ha determinato effetti né su proteine, né su carboidrati.

IV. A new insight on aging effects in human Granulosa cells: a multidisciplinary FTIR and qPCR approach. (Una nuova prospettiva

sugli effetti dell'invecchiamento sulle GCs umane: un approccio multidisciplinare, condotto con FTIR e qPCR). Lo scopo di questa sezione era la determinazione delle modificazioni biochimiche indotte dall'invecchiamento sulle GCs. Per far questo, le GCs ottenute da 20 pazienti consenzienti, sono state disidratate all'aria e suddivise in due gruppi sperimentali: 'Young' (età di 31.2±2.20) e 'Old' (età di 42.5±1.84). Inoltre, da aliquote delle stesse GCs è stato estratto l'RNA totale per l'espressione genica, eseguita tramite qPCR. L'analisi vibrazionale ha messo in luce variazioni nella composizione biochimica delle GCs, causate dall'invecchiamento; in particolare, è emerso un meccanismo di attivazione di stress ossidativo, individuabile grazie all'aumento del contenuto lipidico totale, dei gruppi carbonilici degli esteri, e dei gruppi =CH. Inoltre, l'età delle pazienti ha modificato il pattern proteico, in termini di contenuto totale e di struttura secondaria. I risultati dell'analisi di espressione genica si sono rivelati coerenti con l'analisi vibrazionale: in particolare, sono stati riscontrati un aumento dell'espressione di *igfbp3* e *foxo3*, e una diminuzione di *igf1*, *sirt1* e *sod2*.

V. Ovarian endometriosis affects Granulosa Cells Endocannabinoid system (ECS). (L'endometriosi ovarica alter ail Sistema endocannabinoide (ECS) delle GCs). Lo scopo di questa sezione era identificare se e come l'endometriosi ovarica potesse alterare l'espressione di molecole dell'ECS nelle GCs di pazienti affette da questa malattia. Per questo studio, l'FTIR imaging e la qPCR sono

state accoppiate per studiare GCs suddivise in due gruppi sperimentali: CTRL (10 pazienti senza diagnosi di infertilità ovarica) e ENDO (10 pazienti con diagnosi di endometriosi ovarica). Entrambe le tecniche utilizzate hanno mostrato profonde alterazioni dell'ECS nelle GCs prelevate da pazienti con endometriosi ovarica; l'espressione genica di molte molecole coinvolte nel funzionamento dell'ECS (*trpv1*, *gpr55*, *cnr1, cnr2*, *nape-pld*, *faah*) hanno mostrato alterazioni significative causate dall'endometriosi; inoltre, anche i metabolismi di lipidi e carboidrati sono risultati modificati (*ppar*α, *ppar*γ, *srebp1*, *fasn* per i lipidi; *glut1* e *glut9* per i carboidrati). L'analisi spettroscopica tramite FTIR imaging ha confermato le alterazioni nelle GCs già evidenziate con qPCR.

VI. Could unilateral ovarian endometriosis affect the contralateral ovary? New insights from a multidisciplinary study. (Può l'endometriosi ovarica unilaterale intaccare l'ovario controlaterale? Nuove prospettive da uno studio multidisciplinare). Lo scopo del presente lavoro era valutare come l'endometriosi ovarica unilaterale potesse influenzare negativamente la funzionalità di entrambi gli ovari della paziente affetta dalla malattia. L'approccio multidisciplinare applicato in questo studio ha visto l'utilizzo di due spettroscopie vibrazionali (FTIRM e RMS, Raman Microspectroscopy) e dell'analisi di espressione genica tramite qPCR. Le GCs sono state suddivise in tre gruppi sperimentali: CTRL (GCs da 10 donne senza diagnosi di infertilità ovarica), CONTRAL (GCs dall'ovario controlaterale di 10

donne con endometriosi ovarica unilaterale) e ENDO (dall'ovario colpito dalla malattia di 10 donne con endometriosi ovarica unilaterale). I dati ottenuti dall'analisi con FTIRM e RMS hanno rivelato in maniera coerente che in entrambi gli ovari, erano presenti profonde alterazioni in termini di contenuto lipidico, caratteristiche degli acidi grassi, composizione proteica e struttura secondaria, carboidrati e acidi nucleici. L'analisi di espressione genica tramite qPCR ha confermato un'alterazione del metabolismo lipidico (aumento di *ppar*α, *ppar*γ e *fasn*), del metabolismo dei carboidrati (diminuzione di *glut1* e *glut9*) e del processo di metilazione del DNA (aumento di *dnmt1* e *dnmt3a*), in entrambi gli ovari.

VII. How do plasticizers BPA and DGB alter the macromolecular composition of luteinized GCs? (In che modo i plastificanti BPA e DGB alterano la composizione macromolecolare delle GCs luteinizzate?) Lo scopo del presente lavoro era indagare gli effetti del bisfenolo A (BPA) e del dietilene glicole dibenzoato (DGB), utilizzati alle dosi 1–10–100ng/ml, sulle GCs umane. Le GCs ottenute da 15 pazienti età 32±3.3 anni, sono state analizzate tramite FTIRM dopo trattamento *in vitro* con BPA/DGB per 48 ore, e poi disidratate su supporti di CaF_2 per le misurazioni IR. L'analisi dei dati ottenuti con FTIRM hanno rivelato che il BPA altera profondamente la composizione biochimica delle GCs, in termini di contenuto lipidico, caratteristiche lipidiche, quantitativo proteico, composizione amminoacidica, contenuto di gruppi fosfato e acidi nucleici. Il DGB

altera le GCs in maniera diversa, modificando i livelli di insaturazione e esterificazione dei lipidi, il contenuto di gruppi fosfato e il contenuto proteico.

Le informazioni ottenute tramite questi lavori sulle GCs possono contribuire ad aumentare la conoscenza sui meccanismi che danneggiano la follicologenesi, tramite un approccio multidisciplinare che ha previsto l'accoppiamento di analisi spettroscopiche e qPCR standard. Grazie ai risultati ottenuti, è stato proposto un metodo innovativo per la valutazione della qualità degli ovociti umani, basato sulle caratteristiche spettrali delle GCs, che ha suggerito la possibilità di utilizzo dell'FTIRM come strumento diagnostico affidabile e di facile utilizzo nella routine delle cliniche di riproduzione assistita, in un prossimo futuro.

INTRODUCTION

1. Folliculogenesis

Folliculogenesis is the process in which a recruited primordial follicle grows and develops into a specialized Graafian follicle, which has two potential fates, to either ovulate its egg to be fertilized, or to die by atresia (Figure 1). The first phase of folliculogenesis, named 'pre-antral' or 'gonadotropin-independent' phase, sees the growth and differentiation of the oocyte, and is mainly modulated by locally produced growth factors. In the second, named 'antral' or 'gonadotropin-dependent' phase, the size of the follicle tremendously increases, under the modulation of follicle stimulating hormone (FSH) and luteinizing hormone (LH) (1).

Pre-antral Follicles

Primordial Follicle. A primordial follicle consists of a small (~15 μm of diameter) oocyte arrested in the dictyotene stage of meiosis, a single layer of squamous granulosa cells (GCs), and a thin basal lamina (1). Some of these follicles are recruited to grow, in a process that continues during a woman life, until the depletion of the primordial follicles pool (menopause) (2). The transition of a primordial follicle to a primary one sees the acquisition of a cuboidal shape by GCs (3). Furthermore, the oocyte starts to grow (4).

Primary Follicle. A primary follicle consists of a growing oocyte, a single layer of one or more cuboidal granulosa cells, and a basal lamina (1). In the

stage of primary follicle, several crucial events occur, such as the expression of FSH receptors in GCs (5), the formation of gap junctions between the oocyte and granulosa cells (6), and zona pellucida (ZP) deposition by the oocyte (1,7).

Secondary Follicle. In the secondary follicle, the oocyte is encircled by a complete ZP, 2-8 layers of GCs, and a theca layer disposed radially around the follicle (1). Thanks to the process of angiogenesis, the secondary follicle is exposed to blood-circulating hormones, such as FSH, LH, and insulin.

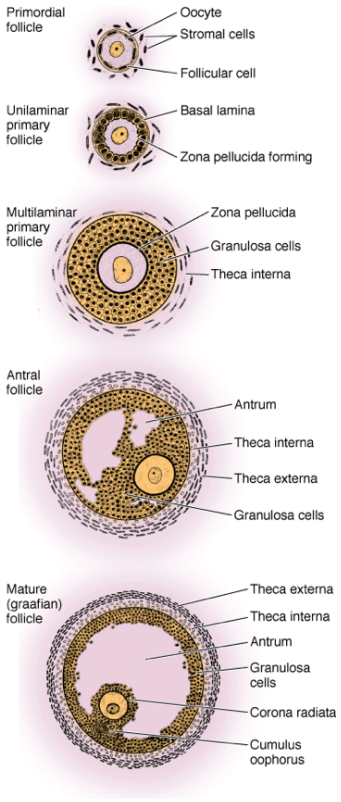

Figure 1. Diagram of developing follicles showing steps in the gonadotropin-independent stages of folliculogenesis, from recruitment of a primordial follicle into the growing pool through its development to the antrum or tertiary (cavitation) stage (From Mescher AL: Junqueira's Basic Histology: Text and Atlas, 12th Edition: http://www.accessmedicine.com. Copyright © McGraw-Hill companies, Inc. All rights reserved).

Antral or Graafian Follicles

One of the key processes characterizing the transition from pre-antral to antral phase is cavitation, consisting in a gradual accumulation of a fluid between GCs, which fills the forming antrum, when the follicle has reached ~400 μm of diameter (8). The follicle that has reached this phase is called tertiary, or Graafian (Figure 2).

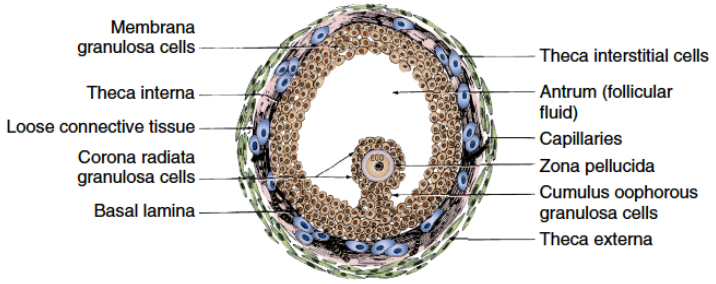

Figure 2. Cross-sectional diagram of a typical healthy Graafian follicle showing the organization of its various cell types (From Erickson GF. Primary cultures of ovarian cells in serum-free medium as models of hormone- dependent differentiation. Mol Cell Endocrinol. 1983;29:21-49.)

During this phase of cavitation, another important process takes place, the differentiation of theca cells, which become steroid-secreting and express LH receptors (9). At this point of folliculogenesis, the oocyte does not grow anymore, as it has reached its full size and its complete development, while the follicle continues to increase its size, sometimes to over 2 cm in diameter (1).

Graafian follicles form a heterogeneous pool of large follicles (400 μm to >2 cm at ovulation), characterized by the presence of the antrum, and are divided into two categories, healthy and atretic, based whether apoptosis occurs or not in GCs. A healthy Graafian follicle is composed of multiple layers of cells: (i) the theca externa, which induces contractions potentially involved in ovulation and atresia (8); (ii) the theca interna, which is composed of 5-8 layers of cells; (iii) GCs, which are disposed in the follicle creating an outer membrane, a periantral domain, a cumulus domain, and a corona radiata domain (Figure 3).

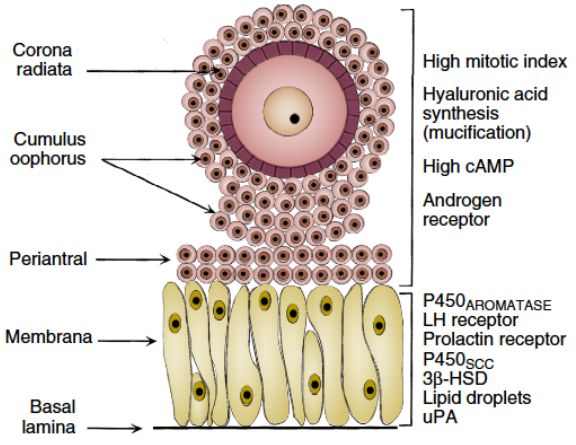

Figure 3. Diagram of the structure-function heterogeneity of the GCs in a healthy Graafian follicle. Depending on their position in the follicle, GCs become different from one another, also in terms of patterns of proliferation and differentiation (From Erickson GF. The graafian follicle: a functional definition. In Adashi EY, ed. Ovulation: evolving scientific and clinical concepts. New York: Springer-Verlag; 2000.)

GCs' populations are different not only on the basis of their position, but also in terms of their cellular functions (10): GCs from corona radiata, cumulus and periantral domain are committed to divide during all the Graafian follicle development, while GCs from the membrana domain stop the mitotic divisions and are able to respond to FSH.

In the pool of Graafian follicles, the dominant one is selected during the late luteal phase, by an unknown mechanism, determining the atresia of the other tertiary follicles (11). Among the features characterizing the dominant Graafian follicle, there is a high mitotic rate of GCs and, hence, a rapid growth of the entire follicle (11). It was suggested that this growth relies on the secondary rise in plasma of FSH, which also increases in the follicular fluid of the dominant follicle (12). The high concentrations of FHS in the follicular fluid determines an increase in the synthesis of estradiol, receptors for progesterone and LH, and the acquisition of the ability to produce progesterone.

Ovulation

Ovulation consists of the rupture of the surface of the ovary by the pre-ovulatory follicle, and by the release of the oocyte-cumulus complex. Oocyte

meiosis, which has been arrested, starts again, under the modulation of the pre-ovulatory surge of LH (1). The resumption of meiosis is associated with a mucification of cumulus cells (CCs), which determines an expansion of the cumulus-oocyte complex and makes possible the transport of the oocyte into the Fallopian tube (13).

Luteogenesis

After ovulation, the follicle becomes corpus luteum: theca interstitial cells and GCs undergo a profound modification and are now named theca lutein and granulosa lutein cells, respectively. The luteogenesis phase is divided into luteinisation and luteolysis. In the first step, a large amount of progesterone and estradiol is produced, thanks to the induction of the expression of the steroidogenic acute regulatory protein (StAR), cytochrome P450 family 11 subfamily A member 1 (CYP11A1), hydroxy-delta-5-steroid dehydrogenase, 3 beta- and steroid delta-isomerase 1 (3β-HSD), cytochrome P450 family 17 subfamily A member 1 (CYP17A1), and cytochrome P450 family 19 subfamily A member 1 (CYP19A1, aromatase) in GCs (14). Luteolysis is determined by the gradual apoptosis in lutein cells.

2. The importance of GCs

The process of acquisition of oocyte competence, defined as the ability of an oocyte to be fertilized and to develop to the blastocyst stage, strictly depends on the follicular microenvironment (15). The progression through all

the folliculogenesis steps heavily rely upon bi-directional interactions between germ cells and the surrounding somatic cells (16). GCs are known to support oocyte growth (17), control the advance of meiosis steps (18), and regulate the oocyte transcriptional activity (19). Furthermore, GCs are responsible for many important follicular functions, such as the production of estradiol during follicular growth, the production of essential nutrients used as an energy source during oocyte maturation (through carbohydrate and lipid metabolism, glucose employment, and lipid oxidation and storage in lipid droplets), the accumulation of oocyte secreted metabolites and the secretion of progesterone after ovulation (20–23). In turn, the oocyte modulates several aspects of GC development including proliferation, differentiation, and extracellular matrix and steroid hormone production (22). Some of the most important functions of GCs are given below.

Glucose metabolism. Glucose is fundamental for mammalian oocytes, but cannot be utilized unless previously transformed into pyruvate by GCs; conversely, GCs display an active glucose metabolism, which provides ATP and metabolites that can be readily utilised by the oocyte, such as pyruvate and lactate (24). Glucose is taken up by GCs via sodium-coupled glucose transporters (SGLTs) or through facilitative glucose transporters (GLUTs) (25).

Lipid metabolism. Among the main functions of GCs, lipid metabolism, consisting of lipid oxidation and storage in lipid droplets, is a crucial factor for the proper follicle development (22). The utilisation of triglycerides and fatty acids for metabolic needs relies on the lipolysis of triacylglycerol within lipid

droplets catalysed by lipases, necessary to oocyte development (26). Fatty acids produced by lipolysis are metabolised by the LH surge-induced β-oxidation for the production of ATP (26).

Amino acids and proteins. Amino acids are the substrates for the synthesis of proteins, nucleotides, GSH, glycoproteins, and several signalling molecules, and are crucial for pH and osmolarity regulation, as heavy metal chelators and as energy substrates (27). It is reported in literature that denuded oocytes have reduced ability to uptake some amino acids (alanine, glycine, histidine and lysine), due to the key role played by GCs and CCs in transferring these molecules to the oocytes (28,29). Together with the building blocks of proteins, also some post-translational modifications rely upon the bidirectional communication of oocytes and GCs: for example, the oocyte protein phosphorylation pattern is modulated by GCs, as proven by culturing oocytes with or without follicular cells (30,31).

Steroid hormones. Sex steroids are crucial for growth and differentiation of reproductive tissues and in the maintenance of fertility, for the follicular and luteal phases, and for uterine receptivity and embryo implantation (32); the de novo production of these hormones from cholesterol, progestins, androgens and estrogens takes place in a sequential manner, following the so-called 'two-cell, two- gonadotropin model', which describes the role of theca cells and GCs in the production of steroids, as a result of the different response of these two cell types to FSH and LH (33). The FSH-induced synthesis of sex steroids is modulated by the oocyte (21,34). Progesterone synthesis involves StAR, p450 cholesterol side-chain cleavage enzyme (p450), and 3β-

hydroxysteroid dehydrogenase (35). Although both theca cells and GCs produce this hormone, the first cell type mainly transforms progesterone into androstenedione, in order to transfer it, as it is or after conversion into testosterone, to GCs, for the synthesis of estradiol (36). The conversion of androgens derived from theca cells into estradiol is catalysed by cytochrome P450 aromatase (37,38). The surge of LH accompanying ovulation transforms theca cells from androgen producing cells to progesterone-producing ones (39).

3. GCs and Assisted Reproductive Technology

With the above concepts in mind, it is clear that an optimal oocyte development heavily relies on a proper follicle development. The Assisted Reproductive Technology (ART) field is active in the search for factors affecting oocyte quality, since less than 7% of oocytes retrieved by in vitro fertilization (IVF) develop into a normal embryo (40). In ART clinical routine, oocyte selection is based on the morphological features of the cytoplasm, meiotic spindle, zona pellucida, polar body and CCs (41). All these criteria for grading and screening oocytes are subjective and controversial and seem not to be related to the intrinsic competence of the oocyte (42–45). Moreover, the current knowledge of the mechanisms determining oocyte quality is still insufficient: what is known is that the relationship between the oocyte and its surrounding somatic cells is more complex than previously thought, and represents a determining factor for later developmental competence, crucial for the success of ART procedures (3). In this light, the improvement of the

oocyte quality assessment, via the identification of markers to be added to the morphological evaluation, must be considered as critical both to achieve higher success rates in ART and to design better therapies for infertility.

Helpful information can be derived from the study of GCs, which play a dominant role in regulating oocyte development and in maintaining the appropriate microenvironment for the acquisition of its competence (16); furthermore, the use of GCs and CCs represents a non-invasive method, since these cells are normally discharged in the ART routine.

In recent years, several studies have focused on finding genes in GCs and CCs that could be correlated with oocyte and embryo quality, but there is a lack of consensus on these selected markers (46): the different study designs and inclusion/exclusion criteria used may influence the results, for example in terms of age (47,48), stimulation protocols (49–51), smoking habits (52,53), and infertility diagnosis (54), as illustrated by the following examples. A study conducted in 2004 by McKenzie and colleagues highlighted that PTGS2, HAS2 and GREM1 gene expression is correlated to embryo morphological and physiological characteristics (55). The analysis of the gene expression profile of CCs derived from oocytes that failed in vitro fertilization revealed the differential expression of 160 genes, with respect to normal embryos (56). Hamel and colleagues found 115 genes differentially expressed between GCs/CCs derived from follicles that resulted in a pregnancy, and GCs/CCs from oocytes that produced embryos that failed early embryo development; among them, 3β-HSD and CYP19A1 were more expressed in GCs and CCs from follicles that led to pregnancy (57). Some other genes whose expression

was reported to be correlated to oocyte maturation, embryo development, or pregnancy are for example: EFNB2 (ephrin B2), CAMK1D (calcium/calmodulin dependent protein kinase ID), GSTA4 (glutathione S-transferase alpha 4) and GSR (glutathione-disulfide reductase) displayed an upregulation in follicles that led to pregnancy (58); PTGS2 (cyclooxygenase 2) and GREM1 (gremlin 1) were upregulated when associated to good quality oocytes, while BDNF (brain-derived neurotrophic factor) was lower when fertilisation was normal (59); BCL2L11 (BCL2 like 11), PCK1 (phosphoenolpyruvate carboxykinase 1) and NFIB (nuclear factor I B) in CCs displayed a significant correlation with embryo potential and successful pregnancy (60). Conversely, Papler and colleagues performed a genome-wide gene expression analysis and did not find gene expression signatures predicting embryo implantation and oocyte fertilization (61).

4. Factors impacting on GCs functions

GCs and aging. Female reproductive aging is the process by which female fecundity is reduced monthly after the age of 30 years and is characterized by a gradual decline both in quality and quantity of the oocytes present in the follicles in the ovarian cortex (62). Female age is one of the key factors affecting clinical outcomes also in in vitro fertilisation (IVF) studies (63). A retrospective study of 2017 on the effects induced by the increasing age on the success rates of ART technology, reported that 38.7% of the cycles performed on women aged 30-35 years, led to clinical pregnancy and 33.3% to live births,

while among women aged 40–44 years, only 23.6% of cycles led to clinical pregnancies and 14.8% to live births (64). Nowadays, subfertility related to female aging has become an important issue for most industrialized societies, mainly because of the increasing delay in childbearing (65,66). Age-induced oxidative stress acts though the impairment of the molecular machinery regulating the response to age-induced stress also in GCs, hence it is considered as a cause of the decline of fertility (67).

GCs and endometriosis. Endometriosis, a chronic gynaecological disease characterised by the presence of epithelial, glandular and stromal endometrial cells in extra-uterine districts (68), is reported to be associated with infertility in 30-50% of women with this diagnosis (69). Among the factors suggested as possible causes of endometriosis-associated infertility, pelvic adhesions, luteinized unruptured follicles, immunological alterations, progesterone resistance, and impairment of folliculogenesis, ovulation, ovum transport, fertilization, and implantation are reported in literature (70,71). Besides these factors, several studies have highlighted that the factor that impacts the most on the subfertility/infertility of women affected by endometriosis is the poor oocyte quality (72). Due to the deep connections between oocyte and GCs, these follicular cells were studied by several groups, highlighting that endometriosis impairs GCs cell cycle (71), increases GCs apoptotic rate (73), reduces antioxidant ability in women with this pathology (74,75), and determines a reduction of the P450 aromatase expression in GCs (76).

GCs and endocrine disruptors. Plasticizers are chemical compounds routinely used to ameliorate plastics in terms of flexibility and workability

(77). Some of them are known to have a hormone-like activity, functioning as endocrine disrupting chemicals (EDCs). EDCs have been reported to interfere with the endocrine system and disturb the normal function of tissues and organs, producing adverse developmental, reproductive, neurological, cardiovascular, metabolic and immune effects (78). For example, bisphenol-A (BPA), one of the most used plasticizer (79–81), is an oestrogen-like compound, since it is able to stimulate the activity of the nuclear oestrogen receptors (ERs), ERα and ERβ (82). In the field of reproduction, BPA was reported to determine implantation failure, lower antral follicle counts, alterations in oviduct and uterine morphology, and abnormal oestrous cyclicity (83). BPA was found in the follicular fluid of women undergoing IVF procedures, raising many concerns, since the presence of EDCs in the fragile microenvironment of the ovarian follicle may be a risk factor for impaired oocyte development, as well as for a correct embryo development (84). Several studies carried out on mammals, showed that BPA affects rat (85), swine (86,87) and murine (88) GCs steroidogenesis; furthermore, BPA exerts a negative effect also on human GCs in vitro: Mansur and colleagues reported that BPA determines a significant decrease in oestradiol and progesterone biosynthesis (89).

5. Vibrational spectroscopies

Fourier Transform Infrared (FTIR) and Raman spectroscopies are fast, label-free vibrational techniques widely applied in life sciences, for

investigating the study of non-homogeneous biological samples, such as cells and tissues, in a non-invasive, label-free and highly specific way.

The analysis of the position, intensity and width of both FTIR and Raman spectral bands allows characterisation, at a molecular level, of functional groups, bonding types, and molecular conformations of the most relevant biological molecules (proteins, lipids, carbohydrates and nucleic acids) and detect the biochemical alterations in tissues and cells affected by various pathologies, or by external agents (90–94). FTIR and Raman spectroscopies are usually considered complementary tools, due to the rule of mutual exclusion, which states that in a symmetric molecule with a centre of inversion, normal vibrational modes cannot be both Infrared and Raman active. Therefore, the parallel use of both of them enables virtually complete information on the spectral features of the investigated samples to be obtained and reliable spectral markers attributable to specific pathologies or alterations to be defined (95,96).

Fourier Transform Infrared spectroscopy allows the examination of the interaction between matter and electromagnetic radiation with an appropriate continuous range of frequencies. In particular, in the mid-IR region (4000–400 cm^{-1}), fundamental vibrations, mainly stretching and bending of chemical bonds, can be detected. The coupling of IR spectrometers with visible microscopes has led to the successful use of this technique for many diagnostic purposes in the life sciences, allowing the detection of subtle biochemical changes caused by specific pathologies, such as tissues affected by tumoral pathologies and stem cells at various differentiation steps (97–99). FTIR

microspectroscopy is successfully applied to investigate tissue samples, since the technique enables the analysis of large sample areas in short time and permits the identification of pathological areas present in the tissue (100–103). To do this, thin sections of samples are required (monolayer cell cultures or 5 mm thick tissues from surgical resection), and IR maps are acquired on previously selected zones. In this way, it is possible to characterize specific subcellular details, giving the possibility to mutually relate the vibrational local features with the morphology of the different compartments of the sample (104–106). Due to the large number of spectral data composing a single map, several programs and statistical tools have been developed to perform multivariate statistical analysis to highlight similarities and differences in the pool of spectra (107–109).

In contrast to FTIR spectroscopy, Raman spectroscopy uses monochromatic light to exploit the phenomena of inelastic scattering, in order to probe the chemical content of a sample (110). Raman spectrometers have also been coupled with visible microscopes, enabling applications of Raman microspectroscopy (RMS) to study biological materials, in several research fields, including of biomedicine, pharmacology, and toxicology (111). RMS spectra contain information about chemical, biological and physical changes of cellular biomolecules, giving a molecular fingerprint of the studied sample (112,113), and RMS has the advantage that it can be performed on cells under physiological conditions, due to the weak contribution of water, with no need for staining (114).

The application of vibrational spectroscopies in several fields of medicine has also included reproductive biology. In particular, the biochemical composition of female gametes, both from oviparous and mammal species, has been investigated (115). Carnevali and colleagues performed FTIRM on zebrafish (*Danio rerio*) ovary sections and single oocytes, in order to characterize the spectroscopic features related to oocyte maturational processes: vibrational IR features were correlated with Selman classification, and the spectral patterns and distribution of vitellogenin and lipovitellin in III and IV oocytes were highlighted (104). The same research group also proposed a study targeted to evidence the effects of *Lactobacillus rhamnosus* and melatonin on the reproductive capabilities of zebrafish, via a multidisciplinary approach that coupled FTIRM and qPCR analyses (105,116). Focal plane array (FPA)-FTIR was applied to investigate aging effects on human oocytes: the chemical maps acquired on single oocytes evidenced a different morphological distribution of lipids, proteins and nucleic acids (117). In literature, the use of RMS on female gametes is described in only few studies, focused on describing the molecular architecture of oocytes from several species (118–120), following the changes occurring during maturation (121), on investigating age-induced effects on mouse oocytes (122), and on analysing the structure of the zona pellucida of ovine oocytes after vitrification (123).

Despite the numerous studies focused on the analysis of GCs, no applications of FTIR and Raman microspectroscopies have been reported to date.

References

1. Conti M, Chang RJ. Folliculogenesis, Ovulation, and Luteogenesis. In: Endocrinology: Adult and Pediatric. Elsevier Inc.; 2016. p. 2179–2191.e3.
2. Hansen KR, Knowlton NS, Thyer AC, Charleston JS, Soules MR, Klein NA. A new model of reproductive aging: the decline in ovarian non-growing follicle number from birth to menopause. Hum Reprod 2008;23(3):699–708.
3. Suh CS, Sonntag B, Erickson GF. The ovarian life cycle: A contemporary view. Rev Endocr Metab Disord 2002;3(1):5–12.
4. Gougeon A, Chainy GB. Morphometric studies of small follicles in ovaries of women at different ages. J Reprod Fertil 1987;81(2):433–42.
5. Oktay K, Briggs D, Gosden RG. Ontogeny of follicle-stimulating hormone receptor gene expression in isolated human ovarian follicles. J Clin Endocrinol Metab 1997;82(11):3748–51.
6. Kidder GM, Mhawi AA. Gap junctions and ovarian folliculogenesis. Reproduction 2002;123(5):613–20.
7. Moos J, Faundes D, Kopf GS, Schultz RM. Composition of the human zona pellucida and modifications following fertilization. Hum Reprod 1995;10(9):2467–71.
8. Erickson GF. The Graafian Follicle: A Functional Definition. In: Adashi EY, editor. Ovulation: Evolving Scientific and Clinical Concepts. New York, NY: Springer New York; 2000. p. 31–48.
9. Erickson GF, Magoffin DA, Dyer CA, Hofeditz C. The ovarian androgen producing cells: a review of structure/function relationships. Endocr Rev 1985;6(3):371–99.
10. Erickson GF, Shimasaki S. The role of the oocyte in folliculogenesis. Trends Endocrinol Metab 2000;11(5):193–8.
11. Gougeon A. Dynamics of follicular growth in the human: a model from preliminary results. Hum Reprod 1986;1(2):81–7.
12. McNatty KP, Hunter WM, MacNeilly AS, Sawers RS. Changes in the concentration of pituitary and steroid hormones in the follicular fluid of human graafian follicles throughout the menstrual cycle. J

Endocrinol 1975;64(3):555–71.
13. Eppig JJ. Oocyte-somatic cell communication in the ovarian follicles of mammals. Semin Dev Biol 1994;5(1):51–9.
14. Carr BR, MacDonald PC, Simpson ER. The role of lipoproteins in the regulation of progesterone secretion by the human corpus luteum. Fertil Steril 1982;38(3):303–11.
15. Al-Edani T, Assou S, Ferrières A, Bringer Deutsch S, Gala A, Lecellier CH, et al. Female aging alters expression of human cumulus cells genes that are essential for oocyte quality. Biomed Res Int 2014;2014:1–10.
16. Kidder GM, Vanderhyden BC. Bidirectional communication between oocytes and follicle cells: ensuring oocyte developmental competence. Can J Physiol Pharmacol 2010;88(4):399–413.
17. Brower PT, Schultz RM. Intercellular communication between granulosa cells and mouse oocytes: Existence and possible nutritional role during oocyte growth. Dev Biol 1982;90(1):144–53.
18. Eppig JJ. Intercommunication between mammalian oocytes and companion somatic cells. BioEssays 1991;13(11):569–74.
19. De La Fuente R, Eppig JJ. Transcriptional activity of the mouse oocyte genome: companion granulosa cells modulate transcription and chromatin remodeling. Dev Biol 2001;229(1):224–36.
20. Chronowska E. High-throughput analysis of ovarian granulosa cell transcriptome. Biomed Res Int 2014;2014.
21. Gilchrist RB, Ritter LJ, Armstrong DT. Oocyte-somatic cell interactions during follicle development in mammals. Anim Reprod Sci 2004;82–83:431–46.
22. Gilchrist RB, Lane M, Thompson JG. Oocyte-secreted factors: Regulators of cumulus cell function and oocyte quality. Hum Reprod Update 2008;14(2):159–77.
23. Downs SM, Mosey JL, Klinger J. Fatty acid oxidation and meiotic resumption in mouse oocytes. Mol Reprod Dev 2009;76(9):844–53.
24. Sutton-Mcdowall ML, Gilchrist RB, Thompson JG. The pivotal role of glucose metabolism in determining oocyte developmental competence. Reproduction 2010;139(4):685–95.
25. Joost H-G, Bell GI, Best JD, Birnbaum MJ, Charron MJ, Chen YT,

et al. Nomenclature of the GLUT/SLC2A family of sugar/polyol transport facilitators. Am J Physiol Endocrinol Metab 2002;282(4):E974-6.

26. Dunning KR, Russell DL, Robker RL. Lipids and oocyte developmental competence: The role of fatty acids and β-oxidation. Reproduction 2014;148(1).
27. Collado-Fernandez E, Picton HM, Dumollard Ré. Metabolism throughout follicle and oocyte development in mammals. Int J Dev Biol 2012;56(10–12):799–808.
28. Eppig JJ, Pendola FL, Wigglesworth K, Pendola JK. Mouse Oocytes Regulate Metabolic Cooperativity Between Granulosa Cells and Oocytes: Amino Acid Transport. Biol Reprod 2005;73:351–7.
29. Pelland AMD, Corbett HE, Baltz JM. Amino Acid transport mechanisms in mouse oocytes during growth and meiotic maturation. Biol Reprod 2009;81(6):1041–54.
30. Colonna R, Cecconi S, Tatone C, Mangia F, Buccione R. Somatic cell-oocyte interactions in mouse oogenesis: Stage specific regulation of mouse oocyte protein phosphorylation by granulosa cells. Dev Biol 1989;133:305–8.
31. Cecconi S, Tatone C, Buccione R, Mangia F, Colonna R. Granulosa cell-oocyte interactions: The phosphorylation of specific proteins in mouse oocytes at the germinal vesicle stage is dependent upon the differentiative state of companion somatic cells. J Exp Zool 1991;258(2):249–54.
32. Messinis IE, Messini CI, Dafopoulos K. Novel aspects of the endocrinology of the menstrual cycle. Reprod Biomed Online 2014;28(6):714–22.
33. Drummond AE. The role of steroids in follicular growth. Reprod Biol Endocrinol 2006;4(1):16.
34. Vanderhyden BC, Tonary AM. Differential regulation of progesterone and estradiol production by mouse cumulus and mural granulosa cells by A factor(s) secreted by the oocyte. Biol Reprod 1995;53(6):1243–50.
35. Niswender GD. Molecular control of luteal secretion of progesterone.

Reproduction 2002;123(3):333–9.

36. Erickson GF, Magoffin DA, Dyer CA, Hofeditz C. The ovarian androgen producing cells: a review of structure/function relationships. Endocr Rev 1985;6(3):371–99.

37. Fitzpatrick SL, Carlone DL, Robker RL, Richards JS. Expression of aromatase in the ovary: down-regulation of mRNA by the ovulatory luteinizing hormone surge. Steroids 1997;62(1):197–206.

38. Simpson ER, Mahendroo MS, Means GD, Kilgore MW, Hinshelwood MM, Graham-Lorence S, et al. Aromatase cytochrome P450, the enzyme responsible for estrogen biosynthesis. Endocr Rev 1994;15(3):342–55.

39. Magoffin DA. Ovarian theca cell. Int J Biochem Cell Biol 2005;37(7):1344–9.

40. Patrizio P, Sakkas D. From oocyte to baby: a clinical evaluation of the biological efficiency of in vitro fertilization. Fertil Steril 2009;91(4):1061–6.

41. Balaban B, Urman B. Effect of oocyte morphology on embryo development and implantation. Reprod Biomed Online 2006;12(5):608–15.

42. Guerif F, Lemseffer M, Leger J, Bidault R, Cadoret V, Chavez C, et al. Does early morphology provide additional selection power to blastocyst selection for transfer? Reprod Biomed Online 2010;21(4):510–9.

43. Balaban B, Urman B, Sertac A, Alatas C, Aksoy S, Mercan R. Oocyte morphology does not affect fertilization rate, embryo quality and implantation rate after intracytoplasmic sperm injection. Hum Reprod 1998;13(12):3431–3.

44. Serhal PF, Ranieri DM, Kinis A, Marchant S, Davies M, Khadum IM. Oocyte morphology predicts outcome of intracytoplasmic sperm injection. Hum Reprod 1997;12(6):1267–70.

45. Ruvolo G, Fattouh RR, Bosco L, Brucculeri AM, Cittadini E. New molecular markers for the evaluation of gamete quality. J Assist Reprod Genet 2013;30(2):207–12.

46. Uyar A, Torrealday S, Seli E. Cumulus and granulosa cell markers of

oocyte and embryo quality. Fertil Steril 2013;99(4):979–97.

47. Tatone C, Amicarelli F. The aging ovary - The poor granulosa cells. Fertil Steril 2013;99(1):12–7.

48. Broekmans FJ, Soules MR, Fauser BC. Ovarian Aging: Mechanisms and Clinical Consequences. Endocr Rev 2009;30(5):465–93.

49. Adriaenssens T, Wathlet S, Segers I, Verheyen G, De Vos A, Van der Elst J, et al. Cumulus cell gene expression is associated with oocyte developmental quality and influenced by patient and treatment characteristics. Hum Reprod 2010;25(5):1259–70.

50. Hamamah S, Matha V, Berthenet C, Anahory T, Loup V, Dechaud H, et al. Comparative protein expression profiling in human cumulus cells in relation to oocyte fertilization and ovarian stimulation protocol. Reprod Biomed Online 2006;13(6):807–14.

51. Haas J, Ophir L, Barzilay E, Yerushalmi GM, Yung Y, Kedem A, et al. GnRH Agonist vs. hCG for Triggering of Ovulation – Differential Effects on Gene Expression in Human Granulosa Cells. PLoS One 2014;9(3):e90359.

52. Sadeu JC, Foster WG. The cigarette smoke constituent benzo[a]pyrene disrupts metabolic enzyme, and apoptosis pathway member gene expression in ovarian follicles. Reprod Toxicol 2013;40:52–9.

53. Gannon AM, Stämpfli MR, Foster WG. Cigarette Smoke Exposure Elicits Increased Autophagy and Dysregulation of Mitochondrial Dynamics in Murine Granulosa Cells1. Biol Reprod 2013;88(3):63.

54. González-Fernández R, Peña Ó, Hernández J, Martín-Vasallo P, Palumbo A, Ávila J. FSH receptor, KL1/2, P450, and PAPP genes in granulosa-lutein cells from in vitro fertilization patients show a different expression pattern depending on the infertility diagnosis. Fertil Steril 2010;94(1):99–104.

55. McKenzie LJ, Pangas SA, Carson SA, Kovanci E, Cisneros P, Buster JE, et al. Human cumulus granulosa cell gene expression: a predictor of fertilization and embryo selection in women undergoing IVF. Hum Reprod 2004;19(12):2869–74.

56. Zhang X, Jafari N, Barnes RB, Confino E, Milad M, Kazer RR. Studies of gene expression in human cumulus cells indicate pentraxin 3 as a

possible marker for oocyte quality. Fertil Steril 2005;83 Suppl 1:1169–79.

57. Hamel M, Dufort I, Robert C, Gravel C, Leveille M-C, Leader A, et al. Identification of differentially expressed markers in human follicular cells associated with competent oocytes. Hum Reprod 2008;23(5):1118–27.

58. Wathlet S, Adriaenssens T, Segers I, Verheyen G, Van Landuyt L, Coucke W, et al. Pregnancy Prediction in Single Embryo Transfer Cycles after ICSI Using QPCR: Validation in Oocytes from the Same Cohort. PLoS One 2013;8(4):e54226.

59. Anderson RA, Sciorio R, Kinnell H, Bayne RAL, Thong KJ, de Sousa PA, et al. Cumulus gene expression as a predictor of human oocyte fertilisation, embryo development and competence to establish a pregnancy. Reproduction 2009;138(4):629–37.

60. Assou S, Haouzi D, Mahmoud K, Aouacheria A, Guillemin Y, Pantesco V, et al. A non-invasive test for assessing embryo potential by gene expression profiles of human cumulus cells: A proof of concept study. Mol Hum Reprod 2008;14(12):711–9.

61. Papler TB, Bokal EV, Lovrecic L, Kopitar AN, Maver A. No specific gene expression signature in human granulosa and cumulus cells for prediction of oocyte fertilisation and embryo implantation. PLoS One 2015;10(3):1–13.

62. Kupka M, D'Hooghe T, Ferraretti AP, de Mouzon J, Erb K, Castilla JA, et al. Assisted reproductive technology in Europe, 2011: results generated from European registers by ESHRE. Hum Reprod 2016;31(2):dev319.

63. Tatone C. Cellular and molecular aspects of ovarian follicle ageing. Hum Reprod Updat 2008;14(2):131–42.

64. O'Brien YM, Ryan M, Martyn F, Wingfield MB. A retrospective study of the effect of increasing age on success rates of assisted reproductive technology. Int J Gynecol Obstet 2017;138(1):42–6.

65. te Velde ER, Pearson PL. The variability of female reproductive aging. Hum Reprod Update 2002;8(2):141–54.

66. Baird DT, Collins J, Egozcue J, Evers LH, Gianaroli L, Leridon H, et

al. Fertility and ageing. Hum Reprod Update 2005;11(3):261–76.

67. Ávila J, González-Fernández R, Rotoli D, Hernández J, Palumbo A. Oxidative Stress in Granulosa-Lutein Cells From In Vitro Fertilization Patients. Reprod Sci 2016;23(12):1656–61.

68. Benagiano G, Brosens I. REVIEW: The history of endometriosis: identifying the disease. Hum Reprod 1991;6(7):963–8.

69. Checa, MA; Gonzalez-Comadran, M; Agramunt, S; Carreras R. Fertility and Endometriosis. Clin Obstet Gynecol 2017;60(3):497–502.

70. Tanbo T, Fedorcsak P. Endometriosis-associated infertility: aspects of pathophysiological mechanisms and treatment options. Acta Obstet Gynecol Scand 2017;96(6):659–67.

71. Toya M, Saito H, Ohta N, Saito T, Kaneko T, Hiroi M. Moderate and severe endometriosis is associated with alterations in the cell cycle of granulosa cells in patients undergoing in vitro fertilization and embryo transfer. Fertil Steril 2000;73(2):344–50.

72. Sanchez AM, Vanni VS, Bartiromo L, Papaleo E, Zilberberg E, Candiani M, et al. Is the oocyte quality affected by endometriosis? A review of the literature. J Ovarian Res 2017;10(43).

73. Fujino K, Yamashita Y, Hayashi A, Asano M, Morishima S, Ohmichi M. Survivin gene expression in granulosa cells from infertile patients undergoing in vitro fertilization–embryo transfer. Fertil Steril 2008;89(1):60–5.

74. Carvalho LFP, Abrão MS, Biscotti C, Sharma R, Nutter B, Falcone T. Oxidative Cell Injury as a Predictor of Endometriosis Progression. Reprod Sci 2013;20(6):688–98.

75. Ngô C, Ché C, Nicco C, Weill B, Chapron C, Dé F, et al. Reactive Oxygen Species Controls Endometriosis Progression. Am J Pathol 2009;175(1):225–34.

76. Sanchez AM, Somigliana E, Vercellini P, Pagliardini L, Candiani M, Vigano P. Endometriosis as a detrimental condition for granulosa cell steroidogenesis and development: From molecular alterations to clinical impact. J Steroid Biochem Mol Biol 2016;155:35–46.

77. Horn O, Nalli S, Cooper D, Nicell J. Plasticizer metabolites in the environment. Water Res 2004;38(17):3693–8.

78. Schug TT, Janesick A, Blumberg B, Heindel JJ. Endocrine disrupting chemicals and disease susceptibility. J Steroid Biochem Mol Biol 2011;127(3–5):204–15.
79. Kang J-H, Kondo F, Katayama Y. Human exposure to bisphenol A. Toxicology 2006;226(2–3):79–89.
80. Crain DA, Eriksen M, Iguchi T, Jobling S, Laufer H, LeBlanc GA, et al. An ecological assessment of bisphenol-A: Evidence from comparative biology. Reprod Toxicol 2007;24(2):225–39.
81. Rubin BS. Bisphenol A: An endocrine disruptor with widespread exposure and multiple effects. J Steroid Biochem Mol Biol 2011;127(1–2):27–34.
82. Matthews JB, Twomey K, Zacharewski TR. In Vitro and in Vivo Interactions of Bisphenol A and Its Metabolite, Bisphenol A Glucuronide, with Estrogen Receptors α and β. Chem Res Toxicol 2001;14(2):149–57.
83. Ziv-Gal A, Flaws JA. Evidence for bisphenol A-induced female infertility: a review (2007–2016). Fertil Steril 2016;106(4):827–56.
84. Ikezuki Y, Tsutsumi O, Takai Y, Kamei Y, Taketani Y. Determination of bisphenol A concentrations in human biological fluids reveals significant early prenatal exposure. Hum Reprod 2002;17(11):2839–41.
85. Zhou W, Liu J, Liao L, Han S, Liu J. Effect of bisphenol A on steroid hormone production in rat ovarian theca-interstitial and granulosa cells. Mol Cell Endocrinol 2008;283(1–2):12–8.
86. Mlynarčíková A, Kolena J, Ficková M, Scsuková S. Alterations in steroid hormone production by porcine ovarian granulosa cells caused by bisphenol A and bisphenol A dimethacrylate. Mol Cell Endocrinol 2005;244(1–2):57–62.
87. Grasselli F, Baratta L, Baioni L, Bussolati S, Ramoni R, Grolli S, et al. Bisphenol A disrupts granulosa cell function. Domest Anim Endocrinol 2010;39(1):34–9.
88. Peretz J, Gupta RK, Singh J, Hernández-Ochoa I, Flaws JA. Bisphenol A impairs follicle growth, inhibits steroidogenesis, and downregulates rate-limiting enzymes in the estradiol biosynthesis pathway. Toxicol Sci 2011;119(1):209–17.

89. Mansur A, Adir M, Yerushalmi G, Hourvitz A, Gitman H, Yung Y, et al. Does BPA alter steroid hormone synthesis in human granulosa cells in vitro? Hum Reprod 2016;31(7):1562–9.
90. Stuart BH. Infrared Spectroscopy: Fundamentals and Applications. 2005.
91. Pilling M, Gardner P. Fundamental developments in infrared spectroscopic imaging for biomedical applications. Chem Soc Rev 2016;45(7):1935–57.
92. Barth A. Infrared spectroscopy of proteins. Biochim Biophys Acta - Bioenerg 2007;1767(9):1073–101.
93. Mantsch HH, Chapman D. Infrared Spectroscopy of Biomolecules. New York, NY: Wiley-Liss; 1996.
94. Lyng F, Faoláin E, Conroy J, Meade A, Knief P, Duffy B, et al. Vibrational spectroscopy for cervical cancer pathology, from biochemical analysis to diagnostic tool. Exp Mol Pathol 2007;82:121–9.
95. Larkin P. Infrared and Raman Spectroscopy. Elsevier; 2011.
96. Owens GL, Gajjar K, Trevisan J, Fogarty SW, Taylor SE, Da Gama-Rose B, et al. Vibrational biospectroscopy coupled with multivariate analysis extracts potentially diagnostic features in blood plasma/serum of ovarian cancer patients. J Biophotonics 2014;7(3–4):200–9.
97. Tosi G, Balercia P, Conti C, Ferraris P, Giorgini E, Lo Muzio L, et al. Microimaging FT-IR of head and neck tumors. V. Odontogenic cystic lesions. Vib Spectrosc 2011;57(1):140–7.
98. Giorgini E, Conti C, Ferraris P, Sabbatini S, Tosi G, Centonze M, et al. FT-IR microscopic analysis on human dental pulp stem cells. Vib Spectrosc 2011;57(1):30–4.
99. Movasaghi Z, Rehman S, Rehman I ur. Fourier Transform Infrared (FTIR) Spectroscopy of Biological Tissues. Appl Spectrosc Rev 2008;43(2):134–79.
100. Krafft C, Sergo V. Biomedical applications of Raman and infrared spectroscopy to diagnose tissues. Spectroscopy 2006;20(5–6):195–218.
101. Gazi E, Gardner P, Lockyer NP, Hart C a, Brown MD, Clarke NW. Direct evidence of lipid translocation between adipocytes and prostate

cancer cells with imaging FTIR microspectroscopy. J Lipid Res 2007;48(8):1846–56.

102. Giorgini E, Sabbatini S, Conti C, Rubini C, Rocchetti R, Re M, et al. Vibrational mapping of sinonasal lesions by Fourier transform infrared imaging spectroscopy. J Biomed Opt 2015;20(12):125003.

103. Baker MJ, Trevisan J, Bassan P, Bhargava R, Butler HJ, Dorling KM, et al. Using Fourier transform IR spectroscopy to analyze biological materials. Nat Protoc 2014;9(8):1771–91.

104. Carnevali O, Conti C, Ferraris P, Garavaglia MG, Gioacchini G, Giorgini E, et al. FT-IR Microspectroscopy on molecular building of Zebrafish oocytes. J Mol Struct 2009;938(1–3):207–13.

105. Giorgini E, Conti C, Ferraris P, Sabbatini S, Tosi G, Rubini C, et al. Effects of Lactobacillus rhamnosus on zebrafish oocyte maturation: An FTIR imaging and biochemical analysis. Anal Bioanal Chem 2010;398(7–8):3063–72.

106. Gioacchini G, Giorgini E, Merrifield DL, Hardiman G, Borini A, Vaccari L, et al. Probiotics Can Induce Follicle Maturational Competence: The Danio rerio Case. Biol Reprod 2012;86(3):65.

107. Walsh MJ, Hammiche A, Fellous TG, Nicholson JM, Cotte M, Susini J, et al. Tracking the cell hierarchy in the human intestine using biochemical signatures derived by mid-infrared microspectroscopy. Stem Cell Res 2009;3(1):15–27.

108. Bonnier F, Byrne HJ. Understanding the molecular information contained in principal component analysis of vibrational spectra of biological systems. Analyst 2012;137(2):322–32.

109. Byrne HJ, Knief P, Keating ME, Bonnier F. Spectral pre and post processing for infrared and Raman spectroscopy of biological tissues and cells. Chem Soc Rev 2016;45(7):1865–78.

110. Keating ME, Byrne HJ. Raman spectroscopy in nanomedicine: current status and future perspective. Nanomedicine (Lond) 2013;8(8):1335–51.

111. Butler HJ, Ashton L, Bird B, Cinque G, Curtis K, Dorney J, et al. Using Raman spectroscopy to characterize biological materials. Nat Protoc 2016;11(4):664–87.

112. Matthäus C, Bird B, Miljković M, Chernenko T, Romeo M. Infrared and Raman Microscopy in Cell Biology. Methods Cell Biol 2008;89(8):275–308.
113. Chan J, Fore S, Wachsmann-Hogiu S, Huser T. Raman spectroscopy and microscopy of individual cells and cellular components. Laser Photonics Rev 2008;2(5):325–49.
114. Notingher I, Verrier S, Romanska H, Bishop AE, Polak JM, Hench LL. In situ characterisation of living cells by Raman spectroscopy. Spectroscopy 2002;16(2):43–51.
115. Giorgini E, Gioacchini G, Sabbatini S, Conti C, Vaccari L, Borini A, et al. Vibrational characterization of female gametes: a comparative study. Analyst 2014;139(20):5049–60.
116. Giorgini E, Gioacchini G, Conti C, Ferraris P, Sabbatini S, Tosi G, et al. The role of melatonin on zebrafish follicle development: An FT-IR imaging approach. Vib Spectrosc 2012;62:279–85.
117. Gioacchini G, Giorgini E, Vaccari L, Ferraris P, Sabbatini S, Bianchi V, et al. A new approach to evaluate aging effects on human oocytes: Fourier transform infrared imaging spectroscopy study. Fertil Steril 2014;101(1):120–7.
118. Wood BR, Chernenko T, Matthäus C, Diem M, Chong C, Bernhard U, et al. Shedding new light on the molecular architecture of oocytes using a combination of synchrotron fourier transform-infrared and raman spectroscopic mapping. Anal Chem 2008;80(23):9065–72.
119. Rusciano G, Pesce G, Salemme M, Selvaggi L, Vaccaro C, Sasso A, et al. Raman spectroscopy of Xenopus laevis oocytes. Methods 2010;51(1):27–36.
120. Heraud P, Marzec KM, Zhang Q, Yuen WS, Carroll J, Wood BR. Label-free in vivo Raman microspectroscopic imaging of the macromolecular architecture of oocytes. Sci Rep 2017;7(1):8945.
121. Davidson B, Murray AA, Elfick A, Spears N. Raman Micro-Spectroscopy Can Be Used to Investigate the Developmental Stage of the Mouse Oocyte. PLoS One 2013;8(7).
122. Bogliolo L, Murrone O, Di Emidio G, Piccinini M, Ariu F, Ledda S, et al. Raman spectroscopy-based approach to detect aging-related

oxidative damage in the mouse oocyte. J Assist Reprod Genet 2013;30(7):877–82.

123. Bogliolo L, Ledda S, Innocenzi P, Ariu F, Bebbere D, Rosati I, et al. Raman microspectroscopy as a non-invasive tool to assess the vitrification-induced changes of ovine oocyte zona pellucida. Cryobiology 2012;64(3):267–72.

Chapter 1

The molecular and functional characterization of human Granulosa cells by FTIR Microspectroscopy correlates with oocyte fate

Gioacchini G, Notarstefano V, Sereni E, Zacà C,
Giorgini E, Vaccari L, Carnevali O, Borini A

Submitted to Cell Reports

Introduction

In Assisted Reproductive Technology (ART) clinical routine, oocyte selection is based on the morphological features of the cytoplasm, polar body and cumulus cells (1). All these criteria for grading and screening oocytes are subjective and controversial and seem not to be related to the intrinsic competence of the oocyte (2–5). Moreover, the current knowledge of the mechanisms determining oocyte quality is still insufficient: what is known is that the relationship between the oocyte and its surrounding somatic cells is more complex than previously thought, and represents a determining factor for later developmental competence, crucial for the success of ART procedures (6). In this light, the improvement of the oocyte quality assessment must be considered as critical both to achieving higher success rates in ART and to designing better therapies for infertility. Helpful information can be derived from the study of Granulosa Cells (GCs), which play a dominant role in regulating oocyte development and in maintaining the appropriate microenvironment for the acquisition of its competence (7). Furthermore, GCs carry out several important functions, such as the production of estradiol during follicular growth and the secretion of progesterone during ovulation (8). They also produce essential nutrients for oocyte development, modulating carbohydrate metabolism, and lipid synthesis, oxidation and storage in lipid droplets, and are used as energy source during oocyte maturation (8,9). Hence, oocyte quality is strongly related to GCs functions, and the identification of specific

molecular markers related to the activity of these cells could be potentially used to predict oocyte quality (10).

Fourier Transform Infrared (FTIR) spectroscopy is a well-established vibrational technique, broadly applied in life sciences for the study of the biomolecular building blocks and composition of cells and tissues samples (11). FTIR spectral bands are analysed in terms of position, intensity and width, making it possible to detect functional groups, bonding types and conformations of the most relevant biological molecules (proteins, lipids, sugars and nucleic acids) (11). In particular, the coupling of IR spectrometers with visible light microscopes has facilitated the application of FTIR Microspectroscopy (FTIRM) in various biomedical fields for diagnostic purposes, providing, at the same time and on the same sample, unique chemical and biological information about the composition and the structural building blocks of the sample (12,13).

The aim of the present study was to assess human oocyte quality by applying, for the first time, FTIRM on luteinized GCs. A comprehensive set of macromolecular data, was obtained according to the position and relative intensities of the vibrational bands composing GCs IR absorption spectra. FTIRM data were submitted to feature selection procedures to identify the most informative biomarkers and hence to obtain the spectral biomarker signature for good quality oocytes. Multivariate statistical tools were applied to validate the identified spectral biomarker signature, hence to confirm the classification of data on the basis of the corresponding clinical outcomes.

Methods

The study, approved by the local Ethic Committee, was carried out in full accordance with ethical principles, including The Code of Ethics of the World Medical Association (Declaration of Helsinki) for experiments involving humans. Patients signed an informed consent for participating to the research.

Enrolment of the patient cohort

A dedicated cohort of 55 patients attending Tecnobios Procreazione for In Vitro Fertilization (IVF) treatment was selected. Enrolment of patients was based on the following inclusion criteria: age < 40 years; no ovarian infertility diagnosis (only tubal, idiopathic and male infertility); regular ovulatory menstrual cycles (25-30 days) with FSH < 10 IU/I on day 3 of the menstrual cycle; sperm sample with a total motility count after treatment ≥ 300.000; number of oocytes retrieved ≥ 8; non-smokers.

Ovarian stimulation protocol

At the onset of menses, patients began gonadotropin stimulation. They received 300 IU/day of recombinant hFSH (Follitropin alfa, Gonal F; Merck, Rome, Italy) for two days and 150 IU/day for four days. The dose was then adjusted according to individual response as assessed by 17β-estradiol (E2) assay and ultrasound scans were performed every other day. To avoid a spontaneous LH surge, patients received a GnRH analogue antagonist. The antagonist injections (Cetrorelix, Cetrotide; Merck, Rome, Italy) at a daily

dose of 0.25 mg started as soon as the leading follicle reached a size of 12-13 mm and continued until HCG administration.

Human chorionic gonadotropin (HCG) (Gonasi HP, Ibsa, Italy) 10000, was administered when at least three follicles reached a maximum diameter of 20 mm, of which at least one was >23 mm. Transvaginal oocyte retrieval was performed under ultrasound guidance 36 hours after HCG administration. The day after oocytes retrieval, each patient started progesterone supplementation with Crinone 8% vaginal gel (Merck) 90 mg twice daily. Supplementation continued until the beta HCG blood test was performed 15 days after embryo transfer. If pregnancy occurred, progesterone supplementation was continued until sonographic confirmation of embryo viability.

GCs sample collection

GCs were obtained from follicles aspirates during oocytes collection. GCs were centrifuged in their follicular fluid at 1100x g for 10 min. The follicular fluid was discarded; the pellet was re-suspended in 2mL of gamete medium (Cook Medical), overlaid on 1 mL pure sperm 50% (obtained by pure sperm 80, Nidacon, and gamete buffer medium) and centrifuged at 1600x g for 13 min to separate it from the red blood cells. After centrifugation, three layers were observed: a top layer containing the follicular fluid, a middle ring-like layer containing the cells derived from the follicular fluid and a bottom layer containing erythrocytes. GCs were recovered in the middle ring-like layer between pure sperm and gamete medium using a Pasteur pipette and placed in 1 mL of NaCl 0.9% solution (Fresenius Kabi). When too many red blood

cells were present, stratification was repeated onto gradient. The GCs were centrifuged at 300x g for 10 minutes. The supernatant was discarded, and the pellet re-suspended in 1 mL of NaCl 0.9% solution and centrifuged again at 300x g for 10 minutes. After additional centrifugation for 5 min at 600x g, the cell pellet was re-suspended in 100 µl of sterile NaCl 0.9% solution.

GCs samples were classified according to the corresponding oocyte clinical outcome into the following experimental groups: **CP**, GCs from oocytes, which gave clinical pregnancy; **FF**, GCs from oocytes, which failed fertilization; **EDF**, GCs from oocytes, which failed embryo development, and **IF**, GCs from oocytes, which failed implantation.

FTIRM data collection

10 µL of GCs suspension (~10^5 cells/ml) were dropped with a Gilson pipette onto CaF_2 UV grade optical windows for IR analysis (38.0x26.0x1.0 mm, Crystran Ltd.) and then let dry at room temperature under biological hood for 30 minutes.

The FTIRM analysis was carried out at the infrared beamline SISSI (Synchrotron Infrared Source for Spectroscopic and Imaging), Elettra Sincrotrone Trieste (Trieste, Italy). A Hyperion 3000 Vis-IR microscope equipped with a nitrogen-cooled HgCdTe detector (MCT_A) and coupled with a Vertex 70 interferometer (Bruker Optics GmbH, Ettlingen, Germany) was used. For each GCs sample, 30 areas of 30x30 µm with densely packed cells monolayer were selected by visible microscopy, on which the corresponding IR spectra were collected in transmission mode, with a

conventional GlowBar source. A 15X Schwarzschild objective (NA=0.4, working distance=24 mm) matched with a 15X condenser in the Mid-IR region were used. Each spectrum was collected with a spectral resolution of 4 cm^{-1} in the IR spectral range 4000-800 cm^{-1} and it was the result of 256 scan averaging. A background spectrum was collected before each sample analysis on a clean zone of the optical window.

FTIRM data processing and analysis

The final absorbance spectra were corrected for water vapour and CO_2 contributions by running the Atmospheric Compensation routine of OPUS software, and vector normalized in the entire spectral range, to mitigate for inhomogeneous thickness of samples (OPUS NT 7.1 software, Bruker Optics GmbH, Germany). Spectra were then cut in the spectral range 4000-1191 cm^{-1} due to the possible presence, at lower wavenumbers, of bands related to contaminants used during the GCs collection step.

To discard outliers, all the spectra acquired for each sample were analysed as follows. The areas of the 2990−2899 cm^{-1} and 1775−1191 cm^{-1} spectral intervals were calculated by drawing a straight line between the aforementioned wavenumber limits and integrating the area above this line (Integration Mode B, OPUS 7.1 software); their sum was defined as the overall cellular biomolecular content (Cell). For each GCs sample, the mean of Cell ± S.D. (Standard Deviation) was calculated, and all the spectra with values outside this range were discarded. Only those GCs samples with at least 15 remaining spectra were further analysed. On each IR spectrum, bands were

firstly analysed in terms of their position and assigned to specific cellular features, as reported in literature (14). Then, for all these bands, the area integrals were obtained by the previously described Integration Method B (Supplementary Table 1) and used to calculate specific band area ratios (Supplementary Table 2), related to the concentration and structure of meaningful biomolecules of GCs.

Spectral Interval (cm^{-1})	**Vibrational mode assignment**	**Cellular functional groups**
2990–2836	Symmetric and asymmetric $CH_{2/3}$ stretching modes, **Lipids**	Saturated alkyl chains of cellular lipids (mainly) and proteins
3027-2995	=CH stretching mode, **CH**	Unsaturated alkyl chains of lipids
2992–2948	Asymmetric CH_3 stretching mode, **CH_3**	Methyl groups of cellular lipids (mainly) and proteins
2946–2889	Asymmetric CH_2 stretching mode, **CH_2**	Methylene groups of cellular lipids (mainly) and proteins
1765-1723	C=O ester moiety stretching, **COO**	Carbonyl ester of fatty acids
1723-1591	Mainly C=O stretching in peptide linkage, Amide I, **AI**	Cellular proteins
1591–1481	Mainly C-N stretching and N-H deformation in peptide linkage, Amide II, **AII**	
1723-1481	Sum of **AI** and **AII**, **Proteins**	
1480-1426	$CH_{2/3}$ bending, **1460**	Methyl and methylene groups of cellular lipids (mainly) and proteins
1426-1372	Mainly CH_3 symmetric stretching of protein chains, **1400**	Methyl groups of cellular lipids (mainly) and proteins
1273-1191	Asymmetric stretching modes of phosphate groups, **Ph1**	Phosphate moieties of nucleic acids (mainly), phospholipids and phosphorylated proteins
2990–2899 & 1775–1191	Sum of all the vibrations indicated above, **Cell**	Overall cellular biomolecular content

Supplementary Table 1. Band area integrals. List of the spectral intervals on which the area integrals were calculated, together with the vibrational mode assignment, the assigned name (bold characters) and the corresponding cellular functional groups.

Banda area ratios	Label	Biological significance
Lipids/Cell	LIP/CELL	Total cellular lipids
Proteins/Cell	PRT/CELL	Total cellular proteins
AI/AII	AI/AII	Protein pattern
Lipids/Proteins	LIP/PRT	Lipids related to protein content
Ph1/Cell	PH1/CELL	Total cellular phosphate groups
Ph1/Proteins	PH1/PRT	Phosphate groups related to protein content
Ph1/Lipids	PH1/LIP	Phosphate groups related to lipid content
COO/Cell	COO/CELL	Total cellular fatty acids
COO/Lipids	COO/LIP	Ester moieties in lipids
1400/Proteins	1400/PRT	Methyl groups related to protein content
1400/Lipids	1400/LIP	Methyl groups related to lipid content
1460/Proteins	1460/PRT	Methyl and methylene groups related to protein content
1400/1460	1400/1460	Methyl and methylene proportion in aliphatic chains
1460/Lipids	1460/LIP	Methyl and methylene groups related to lipid content
CH/Cell	CH/CELL	Unsaturation levels in lipid chains
CH/Lipids	CH/LIP	
CH/CH_3	CH/CH3	
CH_2/Lipids	CH2/LIP	Branching of lipid chains
CH_2/CH_3	CH2/CH3	

Supplementary Table 2. Band area ratios. Band area ratios of the integrals defined in Supplementary Table 1, label used and its biological significance.

Dataset building

All the aforementioned band area ratios listed in Supplementary Table 2 were used to build a dataset balanced according to the limited number of follicles belonging to **CP** experimental group (n. 23): hence, we randomly

selected 23 GCs samples from every other experimental group (**FF**, **EDF** and **IF**), for a total of 92 samples. The validation of this random selection was performed exchanging one by one the samples included in the dataset with others belonging to the same experimental group (data not shown). This dataset, named DS1, was composed of 1043 rows, corresponding to the IR spectra on which band area ratios were calculated (290 for **CP**, 286 for **FF**, 200 for **EDF**, and 267 for **IF**) and of 19 columns, corresponding to the values of band area ratios (reported in Supplementary Table 2).

Derivation of the biomarker signature

To identify the minimal subset of band area ratios (feature selection) necessary and non-redundant to segregate and characterize the experimental groups **CP**, **FF**, **EDF**, and **IF** (defined as biomarker signature), the following statistical approaches were carried out on DS1 (XLSTAT 2017.01, Addinsoft): (i) '*Leave-one-out' method on FDA (Factorial Discriminant Analysis)*: FDA was performed by using all the band area ratios in DS1 and removing them one at a time, to evaluate their relevance in the definition of the experimental groups; (ii) *Variable Characterization method*: this method let characterize the experimental groups, investigating the relations shared with the characterizing features: hence it provides information on whether a feature is necessary or not to describe the experimental groups. To this end, a correlation coefficient is calculated between the categorical variable to characterize (experimental group) and the characterizing feature (band area ratio): if this coefficient is different from 0, a significant dependence exists between the categorical variable (experimental group) and the features (band area ratios). The

statistical significance was determined by the Fisher F-test ($p < 0.05$); (iii) *Logistic Regression method with the Multinomial Logit model:* this method was performed to link a set of selected features (band area ratios) with the probability of occurrence/non-occurrence of an event (the probability that a GCs sample belongs to one of the experimental groups), after classifying the features according to their importance and usefulness to distinguish the experimental groups. The null hypothesis (H0) was tested to define whether the variables (features) bring significant information: in particular, the Likelihood ratio test (-2 Log(Likelihood)), the Score test and the Wald test were performed comparing the model (built on the basis of DS1, composed of observations divided into experimental groups and features) with a simpler model composed of only one given constant. In addition, to determine whether all the selected features bring significant information, a further check was performed, running the Likelihood ratio test and removing a feature at a time: if Pr > LR (where Pr is the probability and LR is the Likelihood Ratio Chi Square) is smaller than a selected significance threshold (0.05), then the feature is necessary to describe the group.

According to the results obtained by the feature selection procedures, a new dataset was built, named DS2, containing the minimal subset of band area ratios (hereafter named biomarkers) describing the differences among the experimental groups **CP**, **FF**, **EDF**, and **IF**.

Univariate statistical analysis

The DS2 dataset was submitted to one-way analysis of variance (ANOVA) followed by Dunnett's multiple comparisons test to determine the presence of statistically significant differences among groups based on each biomarker (OriginPro, version 9.4, OriginLab, Northampton, MA). Statistical significance was set at $p < 0.05$.

Multivariate statistical analysis

To investigate the dependence of the spectral data on all the biomarkers at the same time and to highlight differences among the experimental groups (**CP**, **FF**, **EDF**, and **IF**), the DS2 dataset was also submitted to Permutational Multivariate ANOVA (PERMANOVA) and Factorial Discriminant Analysis (FDA). PERMANOVA is a distribution- and parameter-free multivariate analysis of variance, which uses permutations to estimate the statistical significance (PERMANOVA+ add-on package of the PRIMER software, v. 6). The data included in DS2 were normalized and organized in a Euclidean-distance matrix; the number of permutations was always set at 999. Statistical significance was set at 0.05 and was evaluated by the p value obtained by the permutation procedure for each term, named P(perm) (15), and by the Monte Carlo random draws from the asymptotic permutation distribution, named P(MC) (16). A pair-wise PERMANOVA was also performed to carry out a one-to-one correlation of all the experimental groups. FDA enabled determination of which biomarkers were useful and necessary to discriminate GCs previously classified into the experimental

groups (XLSTAT 2017.01, Addinsoft). Statistical significance was set at $p < 0.05$. The null hypothesis (H0) that the within-class covariance matrices are equal was evaluated by the Box test (carried out both with chi-square and Fisher's F asymptotic approximations) and the Kullback test. Wilks' Lambda test was also used to reject the null hypothesis that the mean vectors of the experimental groups are equal.

In addition, Canonical Analysis of Principal coordinates (CAP) was performed on a new dataset, named DS3, built including only the average values of the biomarkers for each GCs sample, hence composed as follows: n. 23 rows for CP, n. 23 rows for FF, n. 23 rows for EDF group, and n.23 for IF group, for a total of 92 rows. CAP is a constrained ordination method, which tests for significant differences among the *a priori* defined groups in multivariate space (PERMANOVA+ add-on package of the PRIMER software, v. 6), finding the axes through the multivariate cloud of points, which best separate the *a priori* given groups (17). The data included in DS3 were normalized and organized in a Euclidean-distance matrix; the number of permutations was always set at 999. Pearson correlations were used to show linear relationships of spectral data with axes. The p value obtained using permutation procedures let evaluate the *a priori* hypothesis of no difference within experimental groups. The value of the squared canonical correlation (δ_1^2) was used to assess the strength of the association between multivariate data and the hypothesis of group differences. A proper number of principal coordinates axes (m) was chosen automatically by the CAP routine. Lastly, a cross-validation procedure was performed for the chosen value of m (17).

Results

Granulosa cells of 55 patients were analysed, for the first time, by using FTIRM. Four experimental groups were defined: **CP**, GCs from oocytes, which gave clinical pregnancy; **FF**, GCs from oocytes, which failed fertilization; **EDF**, GCs from oocytes, which failed embryo development, and **IF**, GCs from oocytes, which failed implantation.

On each GC sample, the IR spectra were acquired in transmission mode in the spectral range 4000-800 cm^{-1}. Outlier spectra were discarded, and on the remaining ones, the following band area ratios were calculated and related to the concentration and structure of meaningful biomolecules contained in GCs (see Supplementary Table 1 and Supplementary Table 2): LIP/CELL, corresponding to total cellular lipids; PRT/CELL, corresponding to total cellular proteins; AI/AII, corresponding to the protein pattern; LIP/PRT, representing lipid content related to protein content; PH1/CELL, corresponding to total cellular phosphate groups; PH1/PRT, representing phosphate groups content related to protein content; PH1/LIP, representing phosphate groups content related to lipid content; COO/CELL, corresponding to total cellular fatty acids; COO/LIP, representing ester moieties in lipids; 1400/PRT, representing methyl groups related to protein content; 1400/LIP, representing methyl groups related to lipid content; 1460/PRT, representing methyl and methylene groups related to protein content; 1400/1460, corresponding to methyl and methylene proportion in aliphatic chains; 1460/LIP, representing methyl and methylene groups related to lipid content; CH/CELL, CH/LIP and CH/CH3, corresponding to the unsaturation level in

lipid chains; CH2/LIP and CH2/CH3, representing the branching of lipid chains.

Biomarker signature

The DS1 dataset, containing the 19 band area ratios calculated on all the IR spectra (N = 1043) acquired on GCs samples (N = 92), was used for the following feature selection procedures.

'Leave-one-out' method on FDA. FDA was performed both on DS1, including all the 19 band area ratios (features), and on other 19 datasets, obtained by removing from DS1 one feature at a time. Table 1 reports the total percentages of correctness of the classification obtained by comparing the results from all datasets. For 17 investigated features, the total percentage of correctness was lower than the one achieved using all of the band area ratios; conversely, an increase in the correctness of the classification was found for PH1/LIP and 1400/LIP.

	Total % correct
All 19 band area ratios	80.25%
Without PH1/LIP	80.63%
Without 1400/LIP	80.35%
Without LIP/CELL	**80.15%**
Without PRT/CELL	**79.48%**
Without PH1/CELL	**78.81%**
Without COO/CELL	**79.67%**
Without COO/LIP	**79.58%**
Without 1400/PRT	**80.15%**
Without 1460/PRT	**80.24%**
Without 1400/1460	**80.06%**
Without CH/LIP	**79.96%**
Without CH/CELL	**79.87%**
Without CH/CH3	**79.96%**
Without CH2/CH3	**80.15%**
Without CH2/LIP	**78.62%**
Without 1460/LIP	**80.06%**
Without AI/AII	**78.62%**
Without LIP/PRT	**79.39%**
Without PH1/PRT	**78.33%**

Table 1. Percentage of correctness of the classification. List of percentages of correctness obtained with 'leave-one-out' method performed on FDA. Highlighted in bold, the % of correctness lower than the one obtained with all band area ratios.

Variable Characterization method. The characterization of the categorical variable 'experimental group' was performed in order to elucidate the link it shared with the selected features (band area ratios). In this light, the correlation coefficient was calculated between the categorical variable and the characterizing feature, and then its value was analysed by Fisher F-test, in order to evidence a possible dependence existing between the categorical variable (experimental group) and the features (band area ratios). For all the

variables, the overall correlation coefficient resulted significantly different from 0, except for 1400/LIP ($p = 0.243$) and PH1/LIP ($p = 0.367$) (Table 2).

Variable label	Correlation coefficient	*p*
PH1/PRT	0.386	**< 0.0001**
COO/LIP	0.350	**< 0.0001**
1400/PRT	0.344	**< 0.0001**
PRT/CELL	0.310	**< 0.0001**
1460/PRT	0.279	**< 0.0001**
Ph1/CELL	0.271	**< 0.0001**
COO/CELL	0.263	**< 0.0001**
1400/1460	0.195	**< 0.0001**
CH2/LIP	0.159	**< 0.0001**
AI/AII	0.150	**< 0.0001**
LIP/PRT	0.145	**< 0.0001**
1460/LIP	0.130	**< 0.0001**
CH/LIP	0.129	**< 0.0001**
CH/CELL	0.123	**< 0.0001**
LIP/CELL	0.069	**< 0.0001**
CH/CH3	0.052	**< 0.0001**
CH2/CH3	0.011	**0.012**
1400/LIP	0.006	0.243
PH1/LIP	0.004	0.367

Table 2. Results of variable characterization method. Results of variable characterization method. Correlation coefficients and p values for each tested variable. Highlighted in bold, the p values lower than the value of significance, set at 0.05.

Logistic regression method with Multinomial Logit Model. This method was performed to classify the features according to their importance and usefulness for distinguishing the experimental groups. The null hypothesis (H0) was tested to define if all the features bring significant information, by the Likelihood ratio test (-2 Log(Likelihood)), the Score test and the Wald test: the model constructed on the basis of DS1 was compared with a simpler

model composed of only one given constant (H0: Y= 0.274). Supplementary Table 3 reports the results of the three tests, in terms of probability of the Chi-square test (Pr > Chi2) which is always lower than 0.0001, letting conclude that significant information is provided by the variables, and the model based on DS1 is more robust than the one related to the null hypothesis.

Test of the null hypothesis: H0=0.274	
Statistic	Pr > Chi2
-2 Log(Likelihood)	< 0.0001
Score	< 0.0001
Wald	< 0.0001

Supplementary Table 3. Assessment of the quality of the model. Results of the logistic regression method, in terms of probability of Chi square (Chi2) test on the Log Likelihood ratio, the Score and the Wald values.

In addition, to determine whether all the selected features bring significant information, the Likelihood ratio test was performed removing a feature at a time: Pr > LR (where Pr is the probability and LR is the Likelihood Ratio Chi Square) checked for each feature, resulted to be smaller than 0.05. Hence, all the features, except for PH1/LIP and 1400/LIP, are necessary to describe the model (Table 3).

Source	Chi-square (LR)	Pr > LR
PH1/PRT	18.800	**< 0.0001**
COO/LIP	40.344	**< 0.0001**
1400/PRT	165.292	**< 0.0001**
PRT/CELL	45.253	**< 0.0001**
1460/PRT	34.674	**< 0.0001**
Ph1/CELL	57.622	**< 0.0001**
COO/CELL	114.257	**< 0.0001**
1400/1460	42.549	**< 0.0001**
CH2/LIP	40.992	**< 0.0001**
AI/AII	28.540	**< 0.0001**
LIP/PRT	15.436	**< 0.0001**
1460/LIP	17.910	**< 0.0001**
CH/LIP	95.729	**< 0.0001**
CH/CELL	16.413	**< 0.0001**
CH2/CH3	50.999	**0.002**
CH/CH3	356.617	**0.004**
LIP/CELL	114.949	**0.016**
PH1/LIP	4.779	0.189
1400/LIP	5.699	0.210

Table 3. Likelihood ratio test. Each band area ratio was removed at a time and its significant contribution was evaluated using the value Pr>LR. Highlighted in bold, Pr>LR values lower than the selected significance threshold (0.05).

According to the results obtained by the three feature selection procedures ('Leave-one-out' method on FDA, Variable Characterization method, and Logistic regression method with Multinomial Logit Model), the following 17 features were selected as biomarkers and used to build a new dataset, DS2: LIP/CELL, PRT/CELL, AI/AII, LIP/PRT, PH1/CELL, PH1/PRT, COO/CELL, COO/LIP, 1400/PRT, 1460/PRT, 1400/1460, 1460/LIP, CH/CELL, CH/LIP, CH/CH3, CH2/LIP, and CH2/CH3.

Univariate statistical analysis

DS2 dataset was submitted to ANOVA test for analysing the statistical variance of selected biomarkers among the experimental groups **CP**, **FF**, **EDF** and **IF**. The results are summarized in Figure 1. Each group was characterized by specific levels of band area ratios, representative of different biological traits. In particular, GCs from **CP** experimental group showed lower values of the CH2/CH3 and CH2/LIP ratios (Fig. 1L,M), and higher values of the 1400/1460 ratio (Fig. 1H), indicating alterations in the proportion between methyl and methylene groups and more branched lipid chains). In **FF** GCs, higher values of LIP/CELL, CH/CELL, CH/LIP, and CH/CH_3 ratios (respectively, Figs. 1A,I,J,K) were found, representative of an increment of lipids with unsaturated alkyl chains. GCs from **EDF** group showed higher values of PRT/CELL (Fig. 1B) and lower values of COO/CELL, COO/LIP and LIP/PRT (respectively, Figs. 1D,E,P), indicating lower amounts of lipids with respect to proteins; moreover, lower values of PH1/CELL and PH1/PRT (respectively, Figs. 1C,Q) were found suggesting a decrement of phosphate groups with respect to both the total cellular and proteins amounts. **IF** GCs were mostly characterized by higher values of COO/CELL, COO/LIP and 1460/LIP (respectively, Figs. 1D,E,N), suggesting higher amounts of fatty acids; in addition, the increase of the 1400/PRT, 1460/PRT, AI/AII and LIP/PRT ratios (respectively, Figs. 1F,G,O,P) was detected, suggesting a lower amount of proteins with respect to lipid alkyl chains.

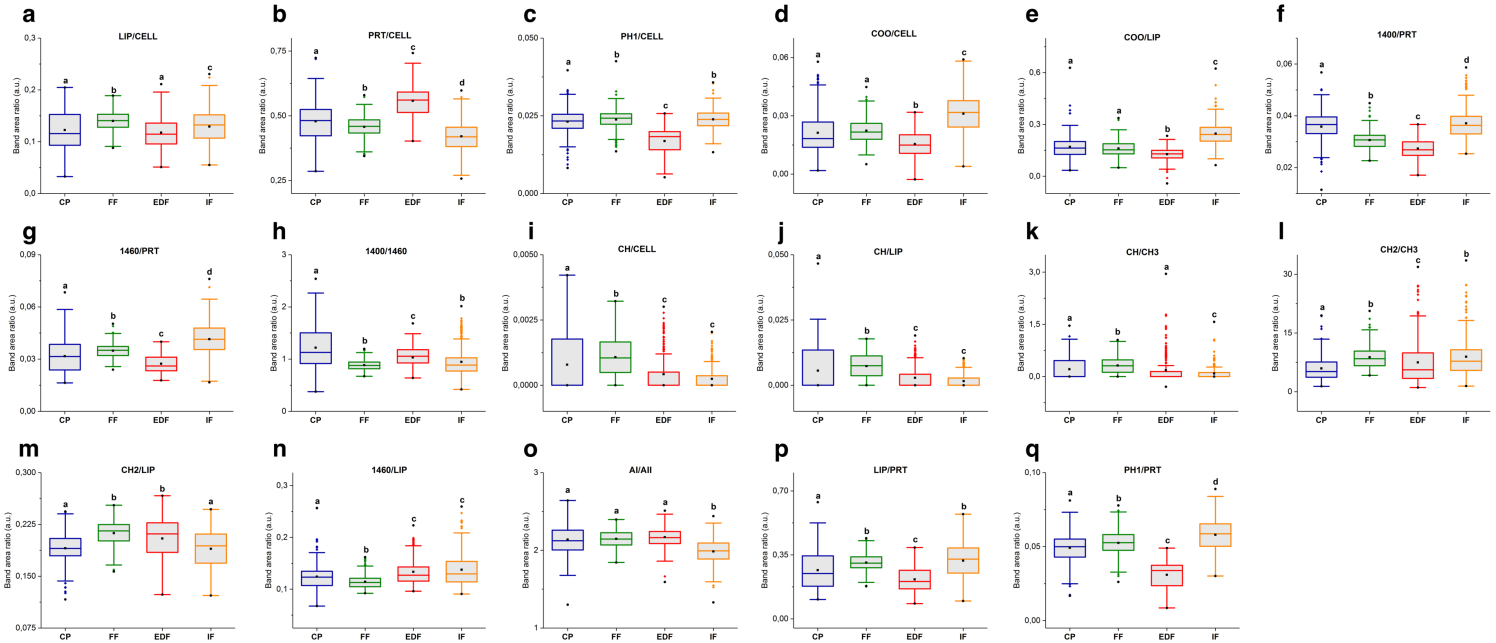
a
LIP/CELL
b
PRT/CELL
c
PH1/CELL
d
COO/CELL
e
COO/LIP
f
1400/PRT
g
1460/PRT
h
1400/1460
i
CH/CELL
j
CH/LIP
k
CH/CH3
l
CH2/CH3
m
CH2/LIP
n
1460/LIP
o
AI/AII
p
LIP/PRT
q
PH1/PRT
Band area ratio (a.u.)
CP
FF
EDF
IF

Figure 1. Results of ANOVA. Box charts show the values of the 17 biomarkers for each experimental group: centre line marks the median, edges indicate the 25th and 75th percentile, whiskers indicate the 5th and the 95th percentile, the black square marks the mean, black circles indicate the minimum and maximum values, coloured diamonds indicate the outliers. Different letters above box charts indicate statistically significant difference among groups. Statistical significance was set at 0.05.

Multivariate statistical analysis

The DS2 dataset was also submitted to multivariate statistical analysis by using PERMANOVA and FDA.

Permutational Analysis of Variance (PERMANOVA). The PERMANOVA analysis indicated a strong discerning effect of the 17 selected biomarkers in the segregation of GCs samples from **CP**, **FF**, **EDF**, and **IF** experimental groups (P(perm) = 0.001, P(MC) = 0.001) (Supplementary Table 4).

Source	**df**	**Pseudo-F**	**P(perm)**	**Unique perms**	**P(MC)**
Group	3	30.885	0.001	998	0.001
Res	2293				
Total	2296				

Construction of Pseudo-F ratio(s) from mean squares

Source	Numerator	Denominator	Num. df	Den.df
Group	1*group	1*Res	3	2293

Supplementary Table 4. PERMANOVA results. The information of interest of PERMANOVA are reported as: *Source*, the sources of variation in the model; *df,* the degrees of freedom; *Pseudo-F*, the pseudo-F ratio; *P(perm)*, permutation P value; *P(MC)*, Monte Carlo P-value.

A pair-wise PERMANOVA was also performed to compare all pairs of experimental groups. Supplementary Table 5 provides pair-wise post-hoc test results, which confirm a statistically significant discerning potential of the 17 selected biomarkers respect to **CP**, **FF**, **EDF**, and **IF** GCs.

Groups	t	P(perm)	Unique perms	P(MC)
CP, IF	8.0024	0.001	999	0.001
CP, FF	4.2377	0.001	997	0.001
CP, EFD	4.9418	0.001	999	0.001
IF, FF	5.5322	0.001	999	0.001
IF, EDF	5.6797	0.001	997	0.001
FF, EDF	2.8348	0.001	998	0.001

Supplementary Table 5. Pair-wise PERMANOVA results. The information of interest of pair-wise PERMANOVA are reported as: *t*, pseudo-*t*, calculated as the square root of pseudo-*F*; *P(perm)*, permutation P value; *P(MC)*, Monte Carlo P-value.

Factorial Discriminant Analysis (FDA). The results obtained from the two Box's tests, carried out by using the chi-square asymptotic approximation and the Fisher's F asymptotic approximation, and by the Kullback test (Supplementary Table 6), confirmed the need to reject the hypothesis that the covariance matrices are equal among the groups.

Box's test (chi-square)		Box's test (Fisher's F)		Kullback test	
-2Log(M)	14486.195	-2Log(M)	14486.195	K (observed value)	7243.098
Chi-square (observed value)	14070.890	F (observed value)	30.648	K (critical value)	509.947
Chi-square (critical value)	590.947	F (critical value)	4231.531	DF	570
DF	459	DF1	459	*p*	< 0.0001
p	< 0.0001	DF2	1939032	alpha	0.05
alpha	0.05	*p*	< 0.0001		
		alpha	0.05		

Supplementary Table 6. Test of the null hypothesis that the covariance matrices are equal between the groups: Box's test, carried out by using the chi-square asymptotic approximation; Box's test, carried out by using the Fisher's F asymptotic approximation; Kullback test.

The interpretation provided for the above cited tests, established that, as the computed p value is lower than 0.05, the null hypothesis H0 that the within-class covariance matrices are equal, should be rejected. F1 and F2 factors, with a cumulative discrimination percentage of 86.887, were used to perform the discriminant analysis. The plot describing how the 17 selected biomarkers correlate with F1 and F2 factors is reported in Supplementary Figure 1.

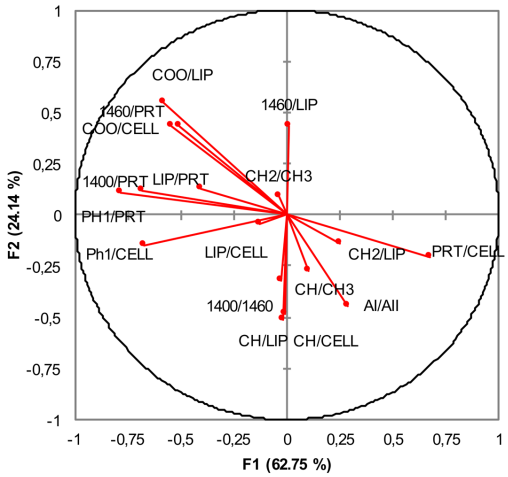

Supplementary Figure 1. FDA correlation chart. Plot showing the correlation of each biomarker with F1 and F2 factors. F1 and F2 have 62.75% and 24.14% of discrimination percentage, respectively, for a cumulative percentage of 86.887%.

GC samples were classified by testing the posterior probability of the observations to belong to one of the experimental groups. The overall success of classification was high (80.06%); in particular, the confusion matrix resulting from the analysis (Supplementary Table 7) reporting the percentage of well characterized observations, showed that the best characterized group resulted to be the **EDF** one (87.50%), followed by **FF** (84.62%), **IF** (80.15%) and then **CP** (70.34%) groups.

from \ to	CP	FF	EDF	IF	Total	% correct
CP	207	47	12	24	290	71.38%
FF	13	243	12	18	286	84.97%
EDF	0	22	177	1	200	88.50%
IF	30	26	1	210	267	78.65%
Total	250	338	202	253	1043	80.25%

Supplementary Table 7. Confusion matrix for the estimation sample. The confusion matrix reports the reclassification of the observations, and shows the percentage of well classified observations, calculated dividing the number of well classified observations by the total number of observations.

The percentages were obtained dividing the number of well classified observations by the total number of observations. Figure 2 shows the observations plotted on the factor axes.

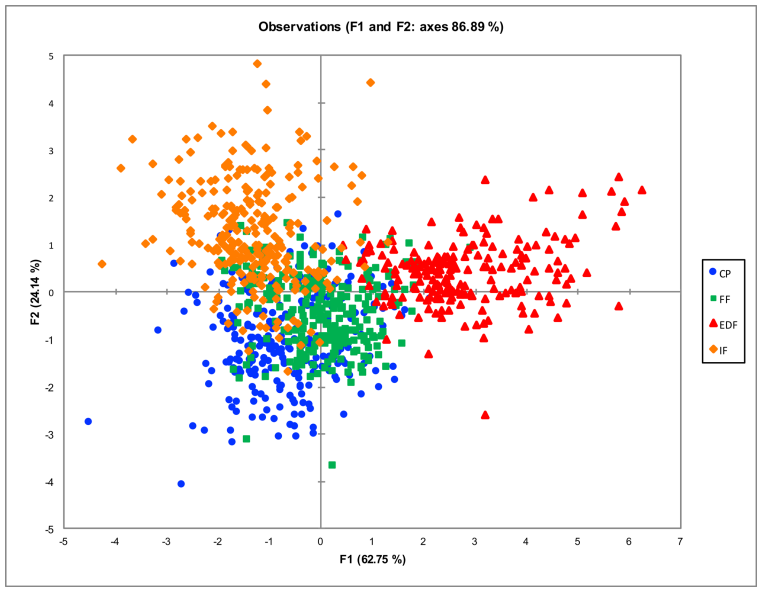

Figure 2. Classification of the observations by FDA. Two-dimensional chart showing the observations plotted on the F1 and F2 factors, with a cumulative discrimination percentage of 86.887.

Canonical Analysis of Principal Coordinates (CAP). CAP analysis was performed by using DS3 dataset (see Materials and Methods). The plot obtained by CAP routine, showing the segregation of the four experimental groups and the Pearson correlations as vectors, is reported in Figure 3.

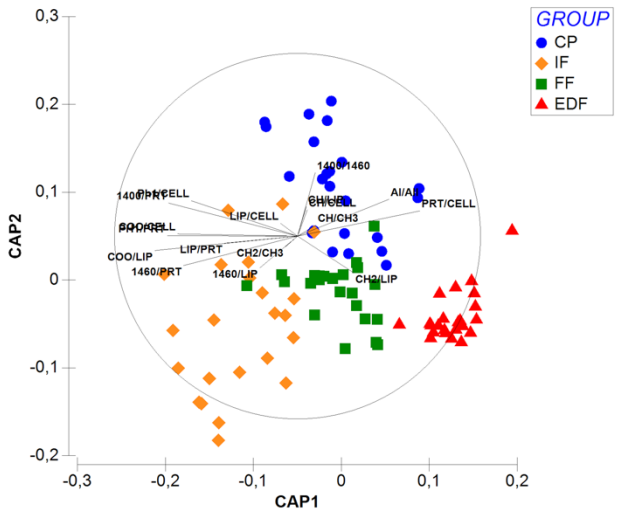

Figure 3. CAP plot. Constrained ordination of the observations plotted on the CAP1 and CAP2 axes, with vector overlay of Spearman rank correlations of each biomarkers with CAP axes.

The cross-validation procedure assigned 69.565% of observations to **CP**, 73.913% to **IF**, 82.609% to **FF** and 91.304% to **EDF**, with a total correctness of 79.35% (Supplementary Table 8).

from \ to	CP	FF	EDF	IF	Total	% correct
CP	16	3	3	1	23	69.565 %
FF	2	19	1	1	23	82.609 %
EDF	0	2	21	0	23	91.304 %
IF	3	3	0	17	23	73.913 %
					Total	79.348 %

Supplementary Table 8. Confusion matrix for cross-validation. The confusion matrix reports the leave-one-out allocation of observations to experimental groups, and shows the percentage of well classified observations, calculated dividing the number of well classified observations by the total number of observations.

Percentages of correctness were calculated dividing the number of well classified observations by the total number of observations. The very large (0.82259) first squared canonical correlation, the p value of 0.001, together with the high cross-validation allocation success, additionally indicate the significance of the 17 selected biomarkers in segregating GCs samples in the experimental groups.

Conclusions

ART is a recognized medical practice leading to the birth of millions of babies. However, the success rate of such practice is still unsatisfactory (18). Furthermore, Patrizio and Sakkas stated that only approximately 5% of fresh oocytes retrieved in ART leads to the birth of a baby (19), and it is still to clarify if the remaining 95% of retrieved oocytes reflects "natural physiological waste" or if we are not able to correctly assess their quality.

In recent years, several studies have been conducted on cumulus and granulosa cell transcriptome, metabolism and other functionalities, to identify molecular biomarkers of oocyte quality (10,20–25); however, there is a lack of consensus on the achieved results (10).

In the present study, an objective and reliable FTIRM-based method was developed to characterize the vibrational fingerprint of Granulosa Cells and to retrospectively relate this spectral information to the corresponding oocyte clinical outcome, in terms of clinical pregnancy (**CP**), fertilization failure (**FF**), embryo development failure (**EDF**), and implantation failure (**IF**). A specific set of inclusion/exclusion criteria for patients enrolling was first established, to avoid bias such as age (26,27), stimulation protocols (22,28,29), smoking habits (30,31), and infertility diagnosis (32).

From GCs spectral analysis, several band area ratios were calculated, describing concentration and structure of the most relevant biomolecules in GCs, including lipids, proteins, and carbohydrates. All these ratios were submitted to a feature selection procedure (performed by 'Leave-one-out' method on FDA, Variable characterization method, and Logistic Regression method with the Multinomial Logit model), with the aim to identify the biomarker signature, defined as the minimal subset of band area ratios necessary and non-redundant to segregate and characterize GCs belonging to **CP**, **FF**, **EDF**, and **IF** experimental groups. This analysis identified 17 band area ratios as spectral biomarkers, singularly analysed by univariate statistics (ANOVA) and then validated by multivariate tools (PERMANOVA, FDA and CAP analysis).

ANOVA analysis pinpointed that each experimental group showed specific spectral traits, ascribable to different biological characteristics of GCs. Hence, these results confirm the close relation between oocyte fate and the follicular microenvironment (20), and shed new light on the specific biochemical alterations in GCs and how they impact on the different clinical outcomes of their companion oocytes. In particular, fertilization failure (**FF**) seemed to be associated with an impairment in GCs lipid metabolism, with higher amount of lipids and unsaturated alkyl chains; embryo development failure (**EDF**) could be ascribable to changes in GCs protein metabolism and phosphate groups, while implantation failure (**IF**) could be related to alterations in GCs lipid and protein metabolism, characterized by an increment of fatty acids and lower amount of proteins. All these results also explained why oocytes from the same patient can undergo different fates depending on the biochemical characteristics of their companion GCs.

ANOVA analysis also confirmed that none of the 17 biomarkers could be singularly used to segregate GCs belonging to the four experimental groups. In this light, multivariate statistical analysis was performed on the complete subset to validate its efficacy. As a first result, PERMANOVA analysis, performed on the four experimental groups, both taken together and pair-wise, evidenced a strong discerning effect of the 17 selected biomarkers in the segregation of GCs samples from **CP**, **FF**, **EDF**, and **IF** experimental groups. The analysis of the plot obtained from FDA evidenced a clear separation along F1 axis (62.75% of discrimination) between **CP** and **IF** GCs from **FF** and **EDF** ones, and hence between GCs from oocytes able or not to develop into

embryos. Furthermore, F2 axis (24.14% of discrimination) segregated **CP** from **IF** GCs, and hence embryos that gave pregnancy from those that failed implantation. Moreover, the analysis of the plot describing how the 17 selected biomarkers correlate with F1 and F2 factors is consistent with the results from ANOVA for almost all the biomarkers. Particularly, **CP** GCs were discriminated by 1400/1460 ratio; COO/LIP, COO/CELL and 1460/PRT ratios resulted discriminant for **IF** GCs, while CH/LIP and CH/CELL segregated **FF** GCs; finally, **EDF** GCs were separated by PH1/PRT and PH1/CELL ratios. The confusion matrix reporting the percentage of well classified observations, showed that GCs from oocytes unable to develop into embryos (**EDF** and **FF**) were better characterized than those from oocytes able to give viable embryos (**IF** and **CP**).

Finally, CAP analysis almost confirmed the results obtained from FDA, demonstrating that the simplified dataset DS3 contains the fundamental information necessary for the correct classification of GCs into the four experimental groups.

Concluding, this innovative method represents a reliable and objective tool to establish in a non-invasive way, the oocyte quality by analysing the biochemical composition of the surrounding Granulosa cells.

References

1. Balaban B, Urman B. Effect of oocyte morphology on embryo development and implantation. Reprod Biomed Online. Januarie 2006;12(5):608–15.
2. Guerif F, Lemseffer M, Leger J, Bidault R, Cadoret V, Chavez C, et al. Does early morphology provide additional selection power to blastocyst selection for transfer? Reprod Biomed Online. Oktober 2010;21(4):510–9.
3. Balaban B, Urman B, Sertac A, Alatas C, Aksoy S, Mercan R. Oocyte morphology does not affect fertilization rate, embryo quality and implantation rate after intracytoplasmic sperm injection. Hum Reprod. Desember 1998;13(12):3431–3.
4. Serhal PF, Ranieri DM, Kinis A, Marchant S, Davies M, Khadum IM. Oocyte morphology predicts outcome of intracytoplasmic sperm injection. Hum Reprod. Junie 1997;12(6):1267–70.
5. Ruvolo G, Fattouh RR, Bosco L, Brucculeri AM, Cittadini E. New molecular markers for the evaluation of gamete quality. J Assist Reprod Genet. 01 Februarie 2013;30(2):207–12.
6. Suh CS, Sonntag B, Erickson GF. The ovarian life cycle: A contemporary view. Rev Endocr Metab Disord. 2002;3(1):5–12.
7. Kidder GM, Vanderhyden BC. Bidirectional communication between oocytes and follicle cells: ensuring oocyte developmental competence. Can J Physiol Pharmacol. April 2010;88(4):399–413.
8. Canipari R. Oocyte-granulosa cell interactions. Hum Reprod Update. 01 Mei 2000;6(3):279–89.
9. Chronowska E. High-throughput analysis of ovarian granulosa cell transcriptome. Biomed Res Int. 2014;2014.
10. Uyar A, Torrealday S, Seli E. Cumulus and granulosa cell markers of oocyte and embryo quality. Fertil Steril. 2013;99(4):979–97.
11. Baker MJ, Trevisan J, Bassan P, Bhargava R, Butler HJ, Dorling KM, et al. Using Fourier transform IR spectroscopy to analyze biological materials. Nat Protoc. Augustus 2014;9(8):1771–91.

12. Wolkers WF, Oldenhof H. In situ FTIR studies on mammalian cells. Spectroscopy. 2010;24(5):525–34.
13. Matthäus C, Bird B, Miljković M, Chernenko T, Romeo M. Infrared and Raman Microscopy in Cell Biology. Methods Cell Biol. 2008;89(8):275–308.
14. Movasaghi Z, Rehman S, Rehman I ur. Fourier Transform Infrared (FTIR) Spectroscopy of Biological Tissues. Appl Spectrosc Rev. 2008;43(2):134–79.
15. Anderson MJ. A new method for non-parametric multivariate analysis of variance. Austral Ecol. Februarie 2001;26(1):32–46.
16. Anderson MJ, Robinson J. Generalized discriminant analysis based on distances. Aust New Zeal J Stat. September 2003;45(3):301–18.
17. Anderson MJ, Willis TJ. Canonical analysis of principal coordinates: a useful method of contrained ordination for ecology. Ecology. 2003;84(2):511–25.
18. Tarín JJ, García-Pérez MA, Cano A. Assisted reproductive technology results: Why are live-birth percentages so low? Mol Reprod Dev. 2014;81(7):568–83.
19. Patrizio P, Sakkas D. From oocyte to baby: a clinical evaluation of the biological efficiency of in vitro fertilization. Fertil Steril. April 2009;91(4):1061–6.
20. Dumesic DA, Meldrum DR, Katz-Jaffe MG, Krisher RL, Schoolcraft WB. Oocyte environment: Follicular fluid and cumulus cells are critical for oocyte health. Fertil Steril. 2015;103(2):303–16.
21. Kim E, Seok HH, Lee S-Y, Lee DR, Moon J, Yoon TK, et al. Correlation between Expression of Glucose Transporters in Granulosa Cells and Oocyte Quality in Women with Polycystic Ovary Syndrome. Endocrinol Metab. 2014;29(1):40–7.
22. Adriaenssens T, Wathlet S, Segers I, Verheyen G, De Vos A, Van der Elst J, et al. Cumulus cell gene expression is associated with oocyte developmental quality and influenced by patient and treatment characteristics. Hum Reprod. 01 Mei 2010;25(5):1259–70.

23. Kordus RJ, LaVoie HA. Granulosa cell biomarkers to predict pregnancy in ART: pieces to solve the puzzle. Reproduction. Februarie 2017;153(2):R69–83.
24. D'Aurora M, Sperduti S, Di Emidio G, Stuppia L, Artini PG, Gatta V. Inside the granulosa transcriptome. Gynecol Endocrinol. 18 Desember 2016;32(12):951–6.
25. Borup R, Thuesen LL, Andersen CY, Nyboe-Andersen A, Ziebe S, Winther O, et al. Competence Classification of Cumulus and Granulosa Cell Transcriptome in Embryos Matched by Morphology and Female Age. Liang C-G, redakteur. PLoS One. 29 April 2016;11(4):e0153562.
26. Tatone C, Amicarelli F. The aging ovary - The poor granulosa cells. Fertil Steril. 2013;99(1):12–7.
27. Broekmans FJ, Soules MR, Fauser BC. Ovarian Aging: Mechanisms and Clinical Consequences. Endocr Rev. Augustus 2009;30(5):465–93.
28. Hamamah S, Matha V, Berthenet C, Anahory T, Loup V, Dechaud H, et al. Comparative protein expression profiling in human cumulus cells in relation to oocyte fertilization and ovarian stimulation protocol. Reprod Biomed Online. Januarie 2006;13(6):807–14.
29. Haas J, Ophir L, Barzilay E, Yerushalmi GM, Yung Y, Kedem A, et al. GnRH Agonist vs. hCG for Triggering of Ovulation – Differential Effects on Gene Expression in Human Granulosa Cells. Zenclussen AC, redakteur. PLoS One. 06 Maart 2014;9(3):e90359.
30. Sadeu JC, Foster WG. The cigarette smoke constituent benzo[a]pyrene disrupts metabolic enzyme, and apoptosis pathway member gene expression in ovarian follicles. Reprod Toxicol. September 2013;40:52–9.
31. Gannon AM, Stämpfli MR, Foster WG. Cigarette Smoke Exposure Elicits Increased Autophagy and Dysregulation of Mitochondrial Dynamics in Murine Granulosa Cells1. Biol Reprod. 01 Maart 2013;88(3):63.
32. González-Fernández R, Peña Ó, Hernández J, Martín-Vasallo P, Palumbo A, Ávila J. FSH receptor, KL1/2, P450, and PAPP genes in granulosa-lutein cells from in vitro fertilization patients show a

different expression pattern depending on the infertility diagnosis. Fertil Steril. Junie 2010;94(1):99–104.

Chapter 2

Validation of an air-dehydration protocol for human Granulosa cells for FTIRM studies

Notarstefano et al.

(manuscript in preparation)

Introduction

Fourier transform infrared microspectroscopy (FTIRM) is a well-established technique to obtain important structural information on the molecular composition of a biological sample, and to perform relative quantification of lipids, proteins, carbohydrates and nucleic acids (1). However, the appropriate preparation of samples is crucial to exploit the full potential of this technology (2).

To date, most of the FTIRM measurements on biological specimens have been performed on dehydrated samples, either fixed or simply air-dried. The spectrum of a fixed cell looks like the one reported in Figure 1, while the most representative cellular bands are listed in Table 1.

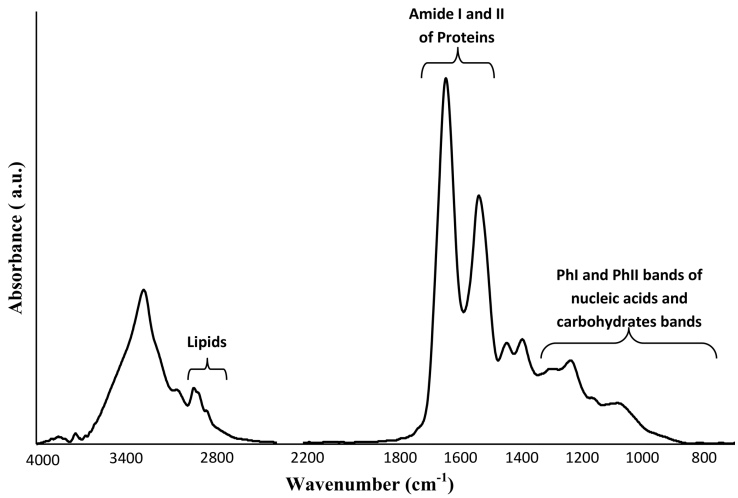

Figure 1. Representative IR spectrum of a fixed cell.

Frequency (cm^{-1})	Assignment	Primary cell constituent
~ 3500	O-H str. of hydroxyl groups	Intracellular water and carbohydrates
~ 3200	N-H str. (Amide A)	Proteins
~ 3010	=C-H str.	Unsaturated aliphatic chains of lipids
3000-2800	Sym. and asym. str. of aliphatic -CH, $-CH_2$ and $-CH_3$ groups	Saturated aliphatic chains of lipids
~ 1730	>C=O str. of ester	Phospholipids
1715-1690	>C=O str. of carbonic acids and nucleotide bases	Amino acid side-chains and nucleic acids
1700-1600	Amide I (80% C=O str., 10% C-N str., 10% N-H def.)	Proteins
1580-1480	Amide II (40% C-N str., 60% N-H def.)	Proteins
1250-1220	PhI, P=O asym. str. of PO_2^- phosphodiester	Nucleic acids backbone
1200-900	C-O-C str., C-O str, C-O-P	Complex network of ring vibrations of carbohydrates
~ 1085	PhII, P=O sym str. of PO_2^- phosphodiester	Nucleic acids backbone

Table 1. Assignment of the most diagnostic vibrational bands, commonly found in FTIR cellular spectra. Abbreviations: str. = stretching; def. = deformation; sym. = symmetric; asym. = asymmetric. Cell constituents to whom some IR-bands are usually associated are also reported. The assignment is done taking into consideration, besides the spectroscopic variables, that the major constituents of a eukaryotic cell are proteins, nucleic acids, carbohydrates and lipids.

The position, width, shape and intensity of a band are diagnostic for the macromolecular content, as well as for the state of order of lipids and folding pattern of proteins and nucleic acids.

Beyond the major simplicity of working with fixed samples, notable limitations have been encountered for FTIRM analysis of cells under

physiological '**wet**' conditions. Recently, the team of SISSI Beamline of Elettra Synchrotron suggested and optimized the exploitation of microfabrication approaches for the realization of fluidics devices dedicated to real-time analysis of living cells. Thanks to these devices, they demonstrated that any dehydration protocol has specific effects on the cellular biochemistry, intended as macromolecular content, folding state of proteins, order of lipid membranes (3–5).

The spectrum of a cell under physiological conditions appears different from that of a dried cell, due to the presence of intracellular water, which accounts for almost 70% of a eukaryotic cell weight (Figure 2). Liquid water has three vibrational modes in the MIR: two stretching modes centred at ~3450 and 3600 cm^{-1}, and a bending mode centred at 1645 cm^{-1} (these contributions can be seen in the water spectrum in Figure 2).

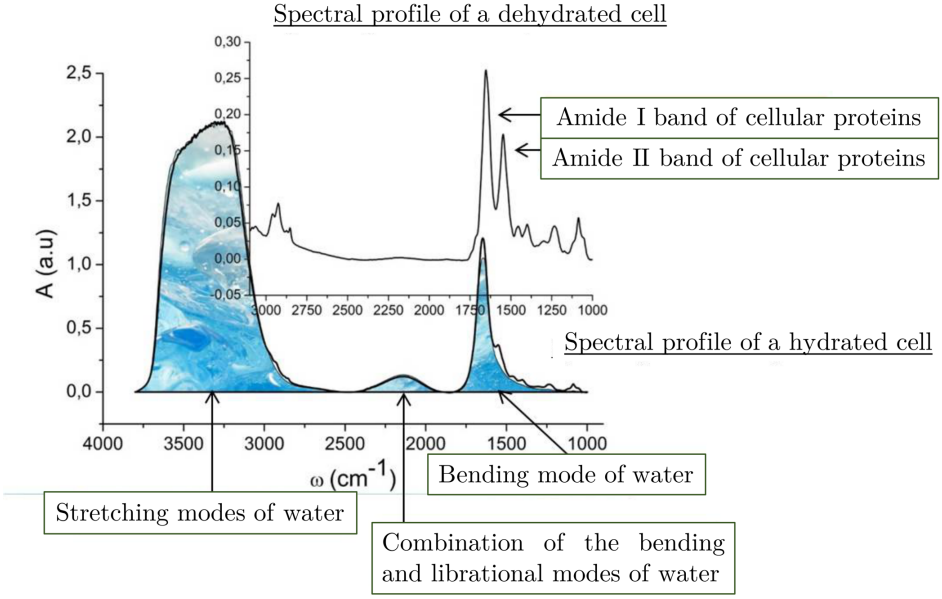

Figure 2. FTIR spectra of a dried cell (background image) and a wet cell (foreground image). The spectral shape of the wet cell is dominated by water spectral features (watery filled spectrum).

While water stretching modes are in a spectral region scarcely diagnostic for the cell, the bending mode completely masks the Amide I band, and partially the Amide II band, therefore limiting the diagnostic capability of the technique in terms of cellular proteins. In order to unmask Amide I profile, removing the water contribution to the cellular spectrum, the optical path of the device has to be lower than 10 μm, which represents the so called "water absorption barrier". Very few scientific reports have been published on FTIRM of living cells, due to the limitation of commercial devices to be used to this aim. Commercial liquid experimental chambers are commonly obtained by spacing apart two IR transparent windows by a plastic spacer, kept in contact by appropriate sample holders. However, such demountable liquid cells do not guarantee a perfect closure and do not ensure a controlled and constant optical path through the whole device, which represents a crucial prerequisite for the accuracy in water subtraction, and therefore data quality, reliability and repeatability. For the purpose of this study, a new microfluidics device has been optimized.

The aim of this study was to assess a fast, user-friendly and reliable preparation protocol for the samples of interest, based on simple air-drying of GCs on appropriate supports. To achieve this, it was fundamental to ascertain

that the dehydration procedure does not affect the most relevant IR spectral bands, by comparing the spectral features of '**wet**' and '**dried**' samples.

Experimental section

The study was approved by the Internal Review Board of Tecnobios Procreazione, in full accordance with the Declaration of Helsinki (World Med. Ass. 2013). To participate in this investigation, each patient signed a written consent, which included the donation of GCs. All samples were anonymous and marked by a code and hence it was impossible to correlate them to a physical person.

Luteinized GCs collection

20 patients enrolled in an *in vitro* fertilization program, were recruited according to the following inclusion criteria: regular ovulatory menstrual cycles; FSH $<$ 10 IU/I on day 3 of the menstrual cycle; non-smokers, and without ovarian infertility nor endometriosis diagnosis. Controlled ovarian stimulation was induced using leuprorelin (Enantone, Takeda, Rome, Italy) and rFSH (Gonal-F, Serono, Rome, Italy, or Puregon Organon, Rome, Italy). HCG at 10,000 IU (Gonasi, Amsa, Rome, Italy) was administered when one or more follicles reached a diameter of ca. 23 mm (6).

At the end of the treatment, a pool of luteinized GCs was collected from all the follicles of each patient, according to the following protocol. The follicular fluid was centrifuged at 1100 x g for 10 min and the pellet was

resuspended in 2 mL of gamete medium, overlaid on 1 mL pure sperm 50% (obtained by pure sperm 80 and gamete buffer medium) and centrifuged again at 1600x g for 13 min to separate GCs from the red blood cells. After centrifugation, GCs were recovered, placed in 1mL of NaCl 0.9% solution and then centrifuged at 300x g for 10 minutes. The supernatant was discarded, and the pellet was resuspended in 1mL of NaCl 0.9% solution and centrifuged again at 300 x g for 10 minutes.

A 10 µl aliquot of each GCs sample was dropped onto a CaF_2 optical window (1-mm thick) and dried for 30 min at RT under a biological hood, and a 10 µl aliquot was dropped in the biocompatible CaF_2 microfluidic device. Further details on sample preparation procedures are reported in the following dedicated paragraphs.

Design, optimization and manufacturing of microfluidic devices for living GCs analysis *(by SISSI Beamline team, Elettra-Synchrotron Trieste)*

For the purposes of the project, new microfluidics devices, transparent to both Visible and Infrared radiation have been designed and built at Elettra-Synchrotron Trieste to perform FTIRM of living GCs in physiological conditions. The two windows composing the device are kept in contact by pressure, generated by a "piston" that is pressed onto the window via a threaded cover. This design allows not only fluid containment, but also circulation of liquids. The fluid flows into the measurement chamber for capillary (the inlet path is connected to a syringe by a PIC capillary); the

excess of liquid from the measurement chamber is aspirated by a syringe pump connected to the outlet via a PIC capillary.

Spectra collection and data analysis of 'dried' GCs

GC samples from the above cited 20 patients have been collected for '**dried**' cell measurements. The same samples have also been measured under physiological conditions. At this stage, information on the patients' anamnesis is not relevant, since a one-to-one correlation has been addressed between '**wet**' and '**dried**' GCs of the same patient. The samples (patients) were generically named with capital letters, followed by the suffix **d** for '**dried**': A_**d**, B_**d**, C_**d**, ...

Sample preparation

GCs suspended in NaCl 0.9% were prepared for FTIRM analysis as follows. 10 µL of GCs suspension (10^5 cells/ml) were dropped with a Gilson pipette onto a CaF_2 UV grade support by Crystran Ltd. (38.0X26.0X1.0mm). Drops were then dried at room temperature under a biological hood. With respect to the protocol proposed in this research, we established that CaF_2 substrate is more suitable for the analysis with respect to silicon IR windows. First, CaF_2 is transparent to visible light, hence allowing both sample visualization and IR data collection in transmission mode. Second, the superior IR transparency of CaF_2 guarantees the acquisition of spectra with a higher Signal to Noise (S/N) ratio. Moreover, data collection on '**wet**' GCs has been carried out by using fluidic devices with CaF_2 optical windows, therefore making the two datasets more comparable.

Data collection

FTIRM measurements were carried out at the SISSI beamline, Elettra-Synchrotron Trieste, equipped with a Vis-IR Hyperion 3000 microscope coupled with a Vertex 70 interferometer (Bruker Optics GmbH, Germany). 50 densely packed GCs monolayer areas (30x30 μm) were selected with visible light, and the corresponding infrared spectra were collected in transmission mode, with a conventional Glow Bar source. A 15X Schwarzschild objective (NA=0.4, working distance=24 mm) matched with a 15X condenser in the Mid-IR region with a single point Hg-Cd-Te (MCT) detector was used. Each spectrum was the result of 256 scans, collected with a spectral resolution of 4 cm^{-1} in the IR spectral range 5000-800 cm^{-1}. The background spectrum was collected every 10 sample points on a clean zone of the optical window, in order to compensate the fluctuations of carbon dioxide and water vapour during the measurement time. The final absorbance spectra were further corrected for water vapour and CO_2 contributions running the Atmospheric Compensation routine of OPUS NT 7.1 software (Bruker Optics GmbH, Germany).

Data analysis

To select 20 statistically representative spectra for each patient, the following procedure was adopted. The 50 raw spectra of each patient were integrated in the spectral ranges 3030-2800 and 1780-900 cm^{-1} and the sum of these areas, commonly considered indicative of the Total Cell Biomass (TCB), was calculated (OPUS NT 7.1 software). The average (AVG) and standard

deviation (STD) of TCB were then evaluated and 20 spectra with a TCB included in the range AVG±STD were selected for the spectral analysis. For each patient, the 20 selected spectra were Second Derivative (DII) transformed (Savitzky-Golay smoothing algorithm, 9 smoothing points), vector normalized in the entire spectral range and averaged to obtain the DII AVG spectrum and the corresponding DII STD. The DII AVG spectra so obtained for '**dried**' GCs, were compared with the corresponding ones of '**wet**' GCs.

Spectra collection and data analysis of 'wet' living GCs

GCs from the previously cited 20 patients were collected for living cell measurements. The same samples were measured after air-drying procedure. At this stage, information on patient anamnesis is not relevant, since a one-to-one correlation was addressed between '**wet**' and '**dried**' GCs of the same patient. The samples (patients) were generically named with capital letters, followed by the suffix **w** for '**wet**': A_**w**, B_**w**, C_**w**, ...

Sample preparation

10 µL of GCs suspension 10^5 cells/ ml in NaCl 0.9% were dropped with a Gilson pipette on the bottom window of the microfluidics device previously described. Once assembled the device and connected it to the physiological solution reservoir (inlet path) and the syringe pump (outlet path), the sample was first visualized and 50 spectra of small cell groups with a lateral resolution of 30x30 µm were selected (Figure 3).

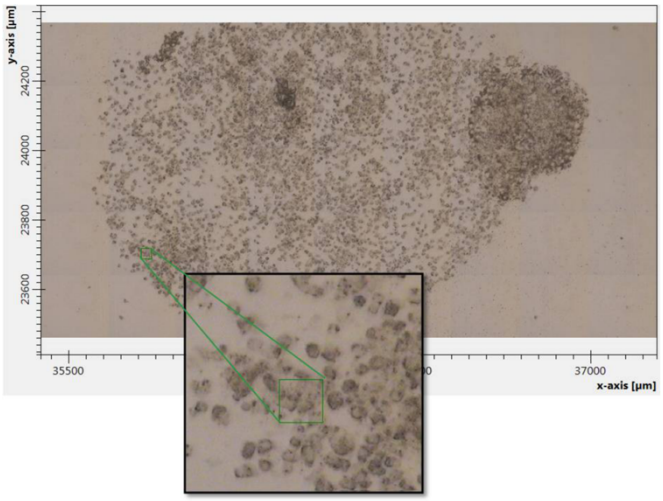

Figure 3. Microphotograph of a living GCs sample inside the microfluidic device. The green square represents the selected area (30x30 µm) on which the IR acquisition was performed.

Data collection

FTIRM measurements were carried out at the SISSI beamline, Elettra-Synchrotron Trieste, equipped with a Vis-IR Hyperion 3000 microscope coupled with a Vertex 70 interferometer (Bruker Optics GmbH, Germany). 50 densely packed GCs monolayer areas (30x30 µm) were measured in transmission mode, with a conventional Glow Bar source. A 15X Schwarzschild objective (NA=0.4, working distance=24 mm) matched with a 15X condenser in the Mid-IR region with a single point Hg-Cd-Te (MCT) detector was used. Each spectrum was the result of 256 scans, collected with a spectral resolution of 4 cm^{-1} in the IR spectral range 5000-800 cm^{-1}. A

spectrum of the physiological solution was collected every 5 close sampled points; in addition, a background spectrum was collected on a clean zone of a CaF_2 optical window (1-mm thick), in order to compensate the fluctuations of carbon dioxide and water vapour during the measurement. The final absorbance spectra were further corrected for water vapour and CO_2 contributions running the Atmospheric Compensation routine of OPUS NT 7.1 software (Bruker Optics GmbH, Germany).

Data analysis

To select 20 statistically representative spectra for each patient, the following procedure was adopted. The 50 raw spectra of each patient were Second Derivative (DII) transformed (Savitzky-Golay smoothing algorithm, 9 smoothing points) and a spectral selection was performed by analysing the region 1280-1150 cm^{-1} (representative of the nucleic acids content and free from water spectral contributions): spectra with poor S/N ratio were discarded. For each patient, a number of 20 spectra was finally chosen. The selected 20 DII spectra were vector normalized in the entire spectral range and averaged to obtain the DII AVG spectrum and the corresponding DII STD for each patient. The DII AVG spectra so obtained for '**wet**' GCs were compared with the corresponding ones of '**dried**' GCs.

Results

In order to confirm the reliability of the air-drying procedure, for each patient a careful comparison between DII average spectra of both '**dried**' and '**wet**' GCs was performed in the spectral range 3040-900 cm^{-1} (Figure 4).

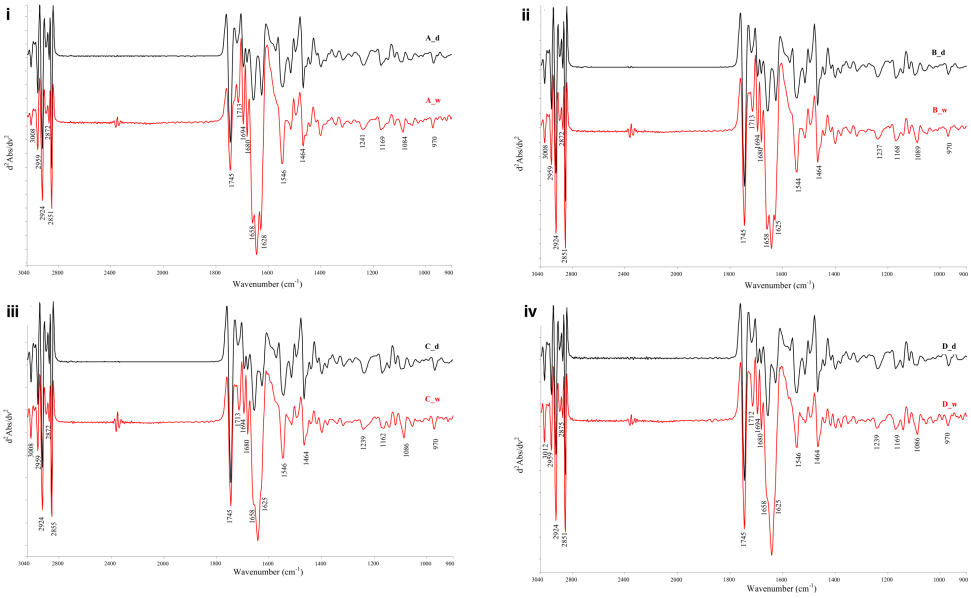

Figure 4. Example of comparison of DII average spectra of both dried (…_**d**) and wet (…_**w**) GCs from patients A (i), B (ii), C (iii), and D (iv), reported in the spectral range 3040-900 cm^{-1}.

The comparison was carried out on DII average spectra, since they normally exhibit a higher resolution of the bands, with respect to spectra in absorbance mode. In particular, it was possible to analyse convoluted absorptions, allowing discrimination of the single component bands (Amide I, Amide II, PhI, PhII, etc., see Table 1). In addition, to avoid the contribution

of water (~3500 cm^{-1}) in '**wet**' samples, the analysis was carried out in the spectral range 3040-900 cm^{-1}.

An impressive correspondence was observed for all the patients, in the spectral profiles from both '**dried**' and '**wet**' GCs. In particular, a complete superimposition was found in the most meaningful biochemical bands: symmetric and asymmetric stretching vibrations of alkyl groups (3008, 2959, 2924, 2872, 2851 cm^{-1}); lipid ester carbonyl stretching (1745 cm^{-1}); thymine carbonyl stretching (1713 cm^{-1}); Amide I (β-sheets: 1694, 1682, 1626 cm^{-1}; α-helices: 1656 cm^{-1}); Amide II (α-helices and random coils: 1546 cm^{-1}); CH_2 bending vibration (1464 cm^{-1}); asymmetric stretching of phosphate moieties (1241 cm^{-1}); CO-P stretching vibration (1171 cm^{-1}); symmetric stretching of phosphate moieties (1086 cm^{-1}), and DNA backbone vibration (969 cm^{-1}).

As expected, all '**wet**' spectra showed an additional band at 1640 cm^{-1}, corresponding to H-O-H deformation of water. This absorption significantly compromises the analysis of Amide I band, meaningful for proteins secondary structure.

Discussion

Many advantages can be highlighted by acquiring IR spectra on '**dried**' samples: the procedure for sample preparation is faster, cheaper and user-friendly; the air-drying procedure does not affect the consistency and reliability of the spectral data; '**dried**' spectra do not show the contribution of water,

which compromises the analysis of diagnostic spectral ranges, such as Amide I.

Thanks to the results we obtained in this one-to-one correlation study, which demonstrated the effectiveness of the air-dehydration protocol of GCs, we decided to use this procedure to prepare the samples for all the FTIRM studies described.

References

1. Doherty J, Cinque G, Gardner P. Single cell analysis using Fourier transform infrared microspectroscopy. Appl Spectrosc Rev 2017;52(6):560–87.
2. Baker MJ, Trevisan J, Bassan P, Bhargava R, Butler HJ, Dorling KM, et al. Using Fourier transform IR spectroscopy to analyze biological materials. Nat Protoc 2014;9(8):1771–91.
3. Birarda G, Grenci G, Businaro L, Marmiroli B, Pacor S, Piccirilli F, et al. Infrared microspectroscopy of biochemical response of living cells in microfabricated devices. Vib Spectrosc 2010;53(1):6–11.
4. Birarda G, Grenci G, Businaro L, Marmiroli B, Pacor S, Vaccari L. Fabrication of a microfluidic platform for investigating dynamic biochemical processes in living samples by FTIR microspectroscopy. Microelectron Eng 2010;87(5–8):806–9.
5. Grenci G, Birarda G, Mitri E, Businaro L, Pacor S, Vaccari L, et al. Optimization of microfluidic systems for IRMS long term measurement of living cells. Microelectron Eng 2012;98:698–702.
6. Borini A, Sciajno R, Bianchi V, Sereni E, Flamigni C, Coticchio G. Clinical outcome of oocyte cryopreservation after slow cooling with a protocol utilizing a high sucrose concentration. Hum Reprod 2005;21(2):512–7.

Chapter 3

Metabolic changes in cultured hGCs: an innovative FTIRM approach

Notarstefano et al.

(manuscript in preparation)

Introduction

Folliculogenesis is a very complex set of biochemical mechanisms, which makes possible follicular development, oocyte maturation, cumulus expansion, and hence ovulation (1). All these processes are strongly influenced both by the oocyte and its somatic cells, which participate in a constant cross-talk, consisting of a continuous and bi-directional exchange of factors, transferred in an extracellular way through the follicular fluid, or by gap junctional coupling. Mural granulosa cells (GCs) carry out many important functions, such as the accumulation of oocyte secreted metabolites, the production of estradiol during follicular growth and the secretion of progesterone after ovulation. They also produce, through carbohydrate and lipid metabolism, glucose employment, and lipid oxidation and storage in lipid droplets, essential nutrients used as an energy source during oocyte maturation (2–5). A dysregulation in the production and consumption of all these molecules can lead to severe cellular damage; an excessive amount of lipids in GCs is reported to determine endoplasmic reticulum stress, mitochondrial dysfunction and apoptosis, leading to decreased rates of oocyte nuclear maturation and fertilization (6,7). In this light, the creation of appropriate *in vitro* models for studying all these processes is desirable (8).

Many attempts have been performed to develop new analytical tools for acquiring information on mechanisms and factors involved in oocyte competence acquisition and quality (9). In this regard, it is clearly necessary to improve the actual knowledge of the macromolecular composition and metabolic processes of GCs. However, a recent study suggested that the in

vitro analysis of these cells could be influenced by culture conditions, which could induce meaningful alterations on their biochemical components (10).

Fourier Transform Infrared spectroscopy is a well-established vibrational technique widely and successfully applied in life sciences for the study of the biomolecular building blocks and composition of cells and tissues. By the analysis of the position, intensity and width of infrared spectral bands, it is possible to investigate functional groups, bonding types and molecular conformations of the most relevant biological molecules (proteins, lipids, sugars and nucleic acids) in a fast and label-free way (11). In particular, the coupling of IR spectrometry with visible light microscopy enables application of this technique to various biomedical fields of research for diagnostic purposes. In fact, Fourier Transform InfraRed Microspectroscopy (FTIRM) allows detection of subtle biochemical changes at a cellular level, providing at the same time and on the same sample, unique chemical and morphological information on the composition and the structural building blocks of all the biomolecules of interest, and hence on cellular activity, metabolism and oxidative stress status (12–14).

In this study, FTIR microspectroscopy was exploited for the first time to analyse, in a fast and reliable way, GCs both immediately after their collection and in vitro cultured for 24, 48 and 96 hours. The analysis of the vibrational data allows definition of the macromolecular composition and structure of fresh GCs. In addition, the biological alterations induced by *in vitro* culture protocols were determined and are discussed in terms of lipid metabolism.

Experimental section

The study was carried out on human GCs and was approved by the Internal Review Board of Tecnobios Procreazione, in full accordance with the Declaration of Helsinki (World Med. Ass. 2013). To participate in this investigation, each patient signed a written consent, which included the donation of GCs. All samples were anonymous and marked by a code and hence it was impossible to correlate them to a physical person.

Sample preparation

17 dedicated consenting patients were recruited according to the following inclusion criteria: medium age 36.8±3.4 years, non-smokers, mean body mass index BMI 19.9±1.8. Patients were enrolled in an in vitro fertilization program because of the following pathologies: male infertility (n. 7); idiopathic infertility (n. 4); low ovarian reserve (n. 4), and diagnosis of endometriosis (n. 2). They were subjected to a controlled ovarian stimulation induced by leuprorelin (Enantone, Takeda, Rome, Italy) and rFSH (Gonal-F, Serono, Rome, Italy, or Puregon Organon, Rome, Italy). HCG at 10,000 IU (Gonasi, Amsa, Rome, Italy) was administered when one or more follicles reached a diameter of ca. 23 mm (15).

GCs were collected from follicles aspirates during oocytes retrieval from each patient, according to the following procedure. Follicular fluid was centrifuged at 1100x g for 10 min and the pellet was resuspended in 2 mL of gamete medium, overlaid on 1 mL pure sperm 50% (obtained by pure sperm 80 and gamete buffer medium) and centrifuged again at 1600x g for 13 min to

separate GCs from the red blood cells. After centrifugation, GCs were recovered, placed in 1 mL of NaCl 0.9% solution and then centrifuged at 300x g for 10 minutes. The supernatant was discarded, and the pellet was resuspended in 1 mL of NaCl 0.9% solution, centrifuged again at 300x g for 10 minutes, and then resuspended in 500 µL of NaCl 0.9% solution. All the retrieved GCs samples were merged in a unique pool. A 10 µl aliquot of this dispersion (considered as control group, **CTRL**) was deposited onto a CaF_2 optical window (1 mm thickness, 13 mm diameter) and dried for 10 min at room temperature under a biological hood for FTIRM analysis. The remaining cells were centrifuged for 5 min at 600x g and resuspended in 3 ml of Dulbecco's modified medium (DMEM)/Ham's F12 (1:1) supplemented with 5% foetal calf serum and an antibiotic-antimycotic solution of penicillin (100 IU/ml) and streptomycin (100 IU/ml). GCs were incubated at 37°C with 5% CO_2 on Petri dishes (BD Biosciences) for 24, 48 and 96 hours (experimental groups named **24H**, **48H** and **96H**). Cells from a single Petri dish were initially centrifuged at 5 min at 600x g, the supernatant was removed, and the cell pellet was resuspended in 5 ml of sterile NaCl 0.9% solution. After additional centrifugation for 5 min at 600x g, the cell pellet was resuspended in 100 µl of sterile NaCl 0.9% solution. A 10 µl aliquot of this suspension was deposited onto a CaF_2 optical window and dried for 10 min at room temperature under a biological hood for FTIRM analysis. All experiments were carried out in triplicate.

FTIRM measurements and data analysis

FTIRM measurements were carried out at the infrared beamline SISSI (Synchrotron Infrared Source for Spectroscopic and Imaging), Elettra Sincrotrone Trieste (Trieste, Italy). A Hyperion 3000 Vis-IR microscope coupled with a Bruker VERTEX 70 interferometer (OPUS 7.1 software package, Bruker Optics, Ettlingen, Germany) was used. The spectrometer was equipped with a HgCdTe (MCT_A) detector operating at liquid nitrogen temperature, which covers the entire IR spectral range from 4000 to 700 cm^{-1}.

On each sample, ~30 areas were selected by visible microscopy on which IR spectra were collected in transmission mode (spatial resolution 30x30 μm^2, spectral resolution 4 cm^{-1}, zero-filling factor of 2 in the spectral range 4000−800 cm^{-1}, scanner velocity 40 kHz, 256 scans). Microscope knife-edge apertures were set at 30×30 μm^2, using a 15X Schwarzschild condenser and objective (NA = 0.4). Background spectra were collected using the same parameters on clean zones of the CaF_2 optical window. All the collected spectra were corrected for the contribution of atmospheric carbon dioxide and water vapour with the compensation routine of OPUS 7.0 software (Bruker Optics GmbH) and then vector normalized. Spectra having at 1660 cm^{-1} a peak height lower than 0.07 a.u. were discarded.

The remaining IR spectra were integrated under the following spectral regions (OPUS 7.1 software): 3000–2836 cm^{-1} (representative of all cellular lipids, LIPIDS); 2970–2948 cm^{-1} ($\nu_{asymm}CH_3$, asymmetric stretching mode of methyl groups, CH3); 2948–2899 cm^{-1} ($\nu_{asymm}CH_2$, asymmetric stretching mode

of methylene groups, CH2); 1780-1715 cm^{-1} (νCOO, stretching mode of triglycerides ester moieties, TRIGLYCERIDES); 1715-1481 cm^{-1} (Amide I and II bands, representative of all cellular proteins, PROTEINS), and 1286–1191 cm^{-1} (ν_{asymm} PO_2^-, asymmetric stretching mode of phosphates, PhI). The sum of the integrated areas 3000–2836 cm^{-1} and 1775–950 cm^{-1} was considered indicative of the total dried cellular biomass (CELL). If not differently reported, band assignment is given on the basis of the review of Movasaghi and colleagues (16).

The absorbance average spectra of all samples as well as their standard deviation (absorbance average spectra ± S.D.) were calculated in the 4000-900 cm^{-1} spectral range, and then a two-point linear baseline was fitted and vector normalized in the same interval. Peak Fitting procedure (Gaussian algorithm) was performed on absorbance average spectra ± S.D. in the 1350-900 cm^{-1} spectral range (GRAMS/AI 7.02, Galactic Industries, Inc., Salem, NH). The number of peaks and the corresponding wavenumbers were carefully determined and fixed according to second derivative results. For each component peak, the mean value of the integrated area was calculated. The sum of the integrated areas of all the underlying bands in the 1350-850 cm^{-1} range was also evaluated (named TOT) and used to calculate specific band area ratios.

Statistical analysis

Normalized infrared spectra were analysed with R Studio (RStudio: Integrated Development for R. RStudio, Inc., Boston, MA) using algorithms

developed in-house. PCA (Principal Components Analysis), commonly used for the analysis of large spectral data sets, was employed a multivariate analysis tool to differentiate the data according to culture times. PCA was performed on all the groups and in a pair-wise way, to improve the identification of the differences among the experimental groups.

Band area ratios were presented as mean ± S.D. Significant differences between experimental groups were determined by means of a factorial analysis of variance (one-way ANOVA), followed by Tukey's multiple comparisons test, using the statistical software package Prism6 (Graphpad Software, Inc. USA). Statistical significance was set at $P < 0.05$.

Furthermore, a non-parametric multivariate analysis of variance (PERMANOVA or NPMANOVA) was performed with the PERMANOVA+ add-on package of the PRIMER software, version 6, according to the software tutorial (17). The dataset used was composed of the ratios obtained from the integrated bands of absorption spectra. All the integration data were normalized and Euclidean-distanced, then the multivariate patterns were checked. The number of permutations was always set at 999. Statistical significance was set at 0.05 and was evaluated by the P value obtained by the permutation procedure for each term (P(perm)) (18) and by the Monte Carlo random draws from the asymptotic permutation distribution (P(MC)) (19). A pair-wise PERMANOVA was also performed to compare all pairs of levels of the factor of interest (groups). In order to highlight and graphically show significant differences among the experimental groups, the same distance matrix of data was subjected to the Canonical Analysis of Principal

Coordinates (CAP) constrained ordination (20), with the culture time as response variable. The a priori hypothesis of no difference within experimental groups was tested evaluating a P value obtained using permutation procedures; the number of permutations was set at 999. The significance of the hypothesis of group differences in relation to the multivariate data was indicated by the value of the first squared canonical correlation (δ_1^2). Lastly, a cross-validation procedure was performed.

Results

GCs, retrieved as a pool from consenting patients enrolled in an in vitro fertilization program, were analysed by FTIRM. In particular, GCs were investigated both immediately after their collection (considered as control group, **CTRL**) and after in vitro culture for 24, 48 and 96 hours (corresponding to **24H**, **48H** and **96H** experimental groups). Only lean patients were enrolled for the study, in order to avoid other contributions on cellular metabolism, due to overweight or obese conditions.

The average absorbance spectra of fresh and cultured GCs are reported in Figure 1. With respect to **CTRL** cells, the spectral profiles of GCs cultured for 24, 48 and 96 hours (**24H**, **48H** and **96H**) showed significant modifications in the 3050-2800 cm^{-1} (asymmetric and symmetric stretching modes of $CH_{2/3}$ of lipids) and 1180-1140 cm^{-1} (stretching modes of C-OP and C-OH bonds) spectral regions as well as in the band at ~1743 cm^{-1}, due to the stretching of COO moieties of triglycerides.

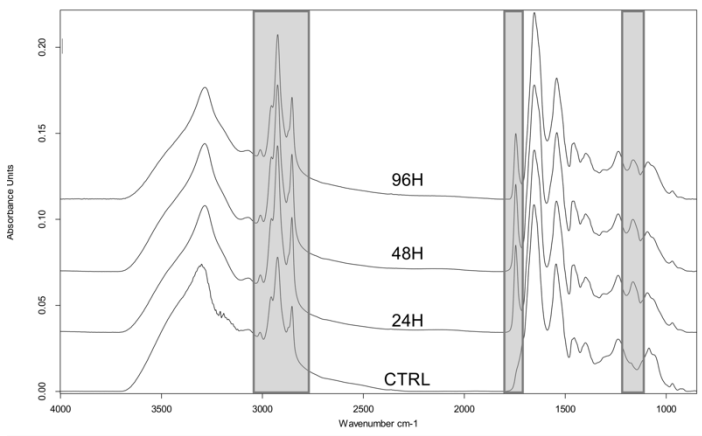

Figure 1. Absorbance average spectra of **CTRL**, **24H**, **48H** and **96H** GCs reported in the spectral range 4000-900 cm^{-1}. Grey areas indicate the 3000-2800 cm^{-1} and 1180-1140 cm^{-1} regions as well as the band at 1743 cm^{-1}.

Multivariate analysis is informative for a detailed understanding of the differences in spectral profiles of the GCs at different culture times, and therefore, PCA was employed to analyse and compare the spectral profiles of experimental groups. Figure 2A shows the PCA scatter plot of GCs spectra from all the four experimental groups. At each culture time (**24H**, **48H** and **96H**), a segregation of GCs from the **CTRL** group was observed. **CTRL** spectra showed a wide distribution in the PCA space, with respect to **24H**, **48H** and **96H** groups. The pair-wise comparisons of **CTRL** vs **24H**, **CTRL** vs **48H** and **CTRL** vs **96H** GCs spectra are showed in Figures 2B, 2C and 2D, respectively. All plots clearly display that PC1 differentiates between the control group and each of the others, and the loadings corresponding to Principal Component 1 of all the PCA tests (Figure 2E), confirmed that the

most visible discriminant features were the same as those previously highlighted on average absorbance spectra.

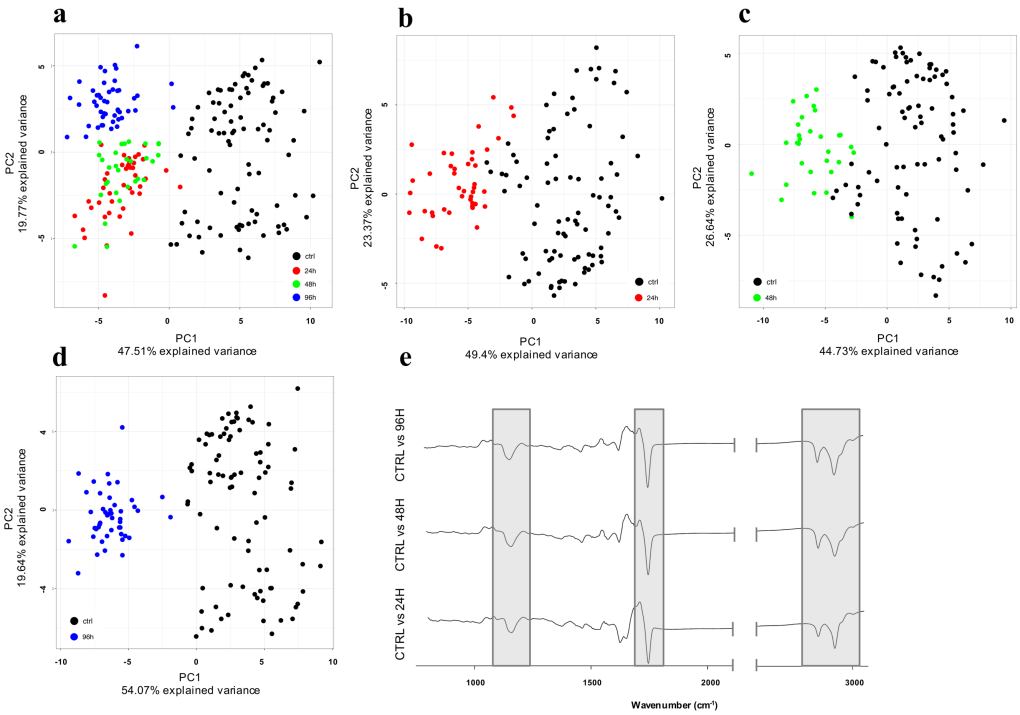

Figure 2. PCA scatter plots of all the experimental groups (**a**), **CTRL** vs **24H** (**b**), **CTRL** vs **48H** (**c**), **CTRL** vs **96H** (**d**). Loadings corresponding to PC1 of **CTRL** vs **24H**, **CTRL** vs **48H** and **CTRL** vs **96H** PCAs (**e**). Grey areas indicate the 3000-2800 cm^{-1} and 1180-1140 cm^{-1} regions, and the band at 1743 cm^{-1}.

Specific band area ratios were calculated for **24H**, **48H** and **96H** cells, by using the area integrals described in the Experimental section and compared with those corresponding to GCs analysed immediately after their collection (**CTRL**) (Figure 3). The analysis of their numerical variation among the

experimental groups leads to the following considerations: (i) the total amount of cellular lipids (LIPIDS/CELL), calculated as the ratio between the integrated area in the 3000–2836 cm^{-1} spectral region (corresponding to CH_2 and CH_3 symmetric and asymmetric stretching modes) and CELL value, showed a significant increase in all cultured GCs (~45% in 24H and 48H, and ~37% in 96H); (ii) the ratio between the integrated area of the band at 1743 cm^{-1} (corresponding to the symmetric stretching of triglycerides ester moieties) and CELL value (TRIGLYCERIDES/CELL) gave a significant and consistent increase at each culture time (~134% in 24H, ~129% in 48H and ~101% in 96H GCs); (iii) by comparing only cultured cells, both LIPIDS/CELL and TRIGLYCERIDES/CELL ratios showed a slight reduction at the longest culture time; (iv) the CH2/CH3 band area ratio significantly increased at all culture times (~23% in all cultured cells); (v) the total amount of cellular proteins (PROTEINS/CELL), calculated as ratio between the integrated area of the 1723-1481 cm^{-1} spectral region (corresponding to Amide I and II bands) and CELL value, did not significantly change in all experimental groups; (vi) the ratio PhI/CELL, calculated as the integrated area of the band at ~1240 cm^{-1} to CELL value, showed a significant decrease in cultured GCs (~28% in 24H, ~33% in 48H and ~18% in 96H GCs).

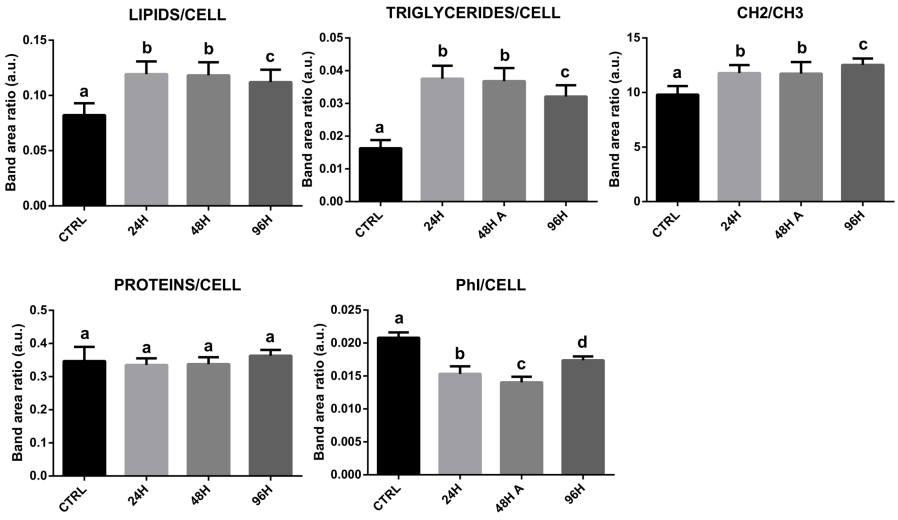

Figure 3. Numerical variation of the following band area ratios, calculated on **CTRL**, **24H**, **48H** and **96H** GCs spectra: LIPIDS/CELL, TRYGLICERIDES/CELL, CH2/CH3, PROTEINS/CELL, and PhI/CELL. Values were reported as mean±SD. Significant differences between experimental groups were determined as described in Materials and Methods (see Statistical Analysis) and reported with different letters.

Peak fitting analysis was carried out in the 1350-850 cm^{-1} spectral region, containing the vibrational modes of phosphates, carbohydrates and nucleic acids. By comparing the fit of **CTRL** cells with those of cultured GCs (**24H**, **48H** and **96H**), only the underlying bands listed below showed statistically significant modifications in the values of area, height and width: 1237 cm^{-1} (ν_{asymm} PO_2^-, asymmetric stretching mode of phosphates, PhI), 1171 cm^{-1} (C-O non H-bonded stretching mode, CO-R), 1151 cm^{-1} (C-O H-bonded stretching mode, CO-H), 1087 cm^{-1} (ν_{symm} PO_2^-, symmetric stretching mode of

phosphates, PhII), and 1054 cm^{-1} (νC-O, δC-O bonds in carbohydrates, GLYCO).

By analysing the numerical variation of specific band area ratios (Figure 4), the following conclusions can be drawn: (i) the value PhI/TOT, calculated as ratio between the integrated area of the band at 1237 cm^{-1} (ν_{asymm} PO_2^-, asymmetric stretching mode of phosphates) and the sum of all the bands in the 1350-850 cm^{-1} interval (named TOT), significantly decreased at each culture time (~22% in **24H**, **48H** and **96H**), as already observed in PhI/CELL; (ii) the value CO-R/TOT, calculated as ratio between the integrated area of the band at 1171 cm^{-1} (ν C-O non H-bonded) and TOT, was always significantly higher in all cultured cells with respect to **CTRL** ones, with a decreasing trend on going from **24H** to **96H** GCs (~260% in 24H, ~220% in 48H and ~160% in 96H); (iii) the ratio CO-H/TOT, calculated by dividing the integrated area of the band centred at 1151 cm^{-1} (ν C-O H-bonded) by TOT, showed the same trend as the CO-R/TOT ratio, with significantly higher values (~5-6 times) in all cultured cells with respect to **CTRL** ones; (iv) the ratio PhII/TOT, obtained dividing the integrated area of the band at 1087 cm^{-1} (ν_{symm} PO_2^-, symmetric stretching mode of phosphates) by TOT, significantly decreased in cultured cells in 24H and 48H, and then slightly increased in 96H ones; (v) the value GLYCO/TOT, calculated as the ratio between the integrated area of the band centred at 1054 cm^{-1} (νC-O and δC-O of carbohydrates, stretching and bending modes of C-O groups of carbohydrates) and TOT, showed a decrease in cultured cells at

24H and **48H**, and then a slight increase in **96H** ones, but none of these alterations were significant.

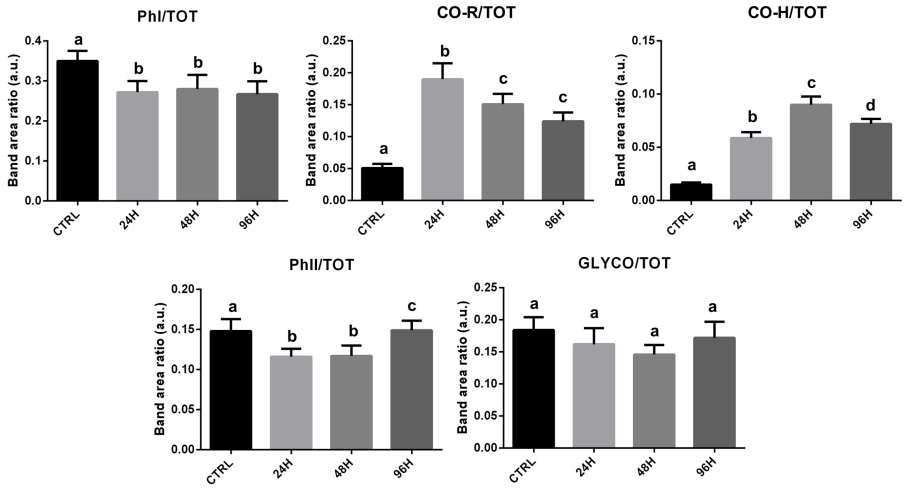

Figure 4. Numerical variation of the following band area ratios, calculated by Gaussian fit on **CTRL**, **24H**, **48H** and **96H** GCs average spectra: PhI/TOT, CO-R/TOT, CO-H/TOT, PhII/TOT. Values were reported as mean±SD. Significant differences between experimental groups were determined as described in Materials and Methods (see Statistical Analysis) and reported with different letters.

The PERMANOVA analysis performed on the integration data showed a significant difference among all the groups, as reported by both P(perm) and P(MC) (Table 1a). A pair-wise PERMANOVA was also performed to compare the 4 experimental groups in pairs. Table 1b illustrates the results of the pair-wise post-hoc results, which confirm the statistically significant difference among GCs on the basis of culture time.

Source	df	Pseudo-F	P(perm)	Unique perms	P(MC)
Gr	3	139.24	0.001	998	0.001
Res		485			
Total		488			
Groups		t	P(perm)	Unique perms	P(MC)
CTRL, 24H		15.035	0.001	998	0.001
CTRL, 48H		14.516	0.001	997	0.001
CTRL, 96H		12.034	0.001	998	0.001
24H, 48H		2.547	0.002	999	0.004
24H, 96H		5.7921	0.001	998	0.001
48H, 96H		5.7818	0.001	998	0.001

Table 1. Output for PERMANOVA test, displaying degrees of freedom (df), Pseudo-F, P(perm), number of permutations (Unique perms) and P(MC). Results obtained by pair-wise PERMANOVA, displaying the *pseudo-t* value (t), P(perm), the number of permutations (unique perms) and P(MC).

The CAP constrained ordination of the integration data shows a clear separation of the control group from all the other ones. Spectral data were normalized and organized in a Euclidean-distance matrix; the number of permutations was set at 999. To assess the statistical significance associated with the discriminative potential of the analysis, we evaluated the first and the second squared canonical correlation (δ_1^2 and δ_2^2) and the P: the first two squared canonical correlations are very large (0.9953 and 0.823), meaning that the canonical axes CAP1 and CAP2 generate a very good separation of

the experimental groups; the P is equal to 0.001 (Figure 5). The cross-validation procedure correctly assigned 100% **CTRL**s, 87.097% **24H**s, 96.552% **48H**s, and 100% **96H**s, with a total correctness of 96.144%.

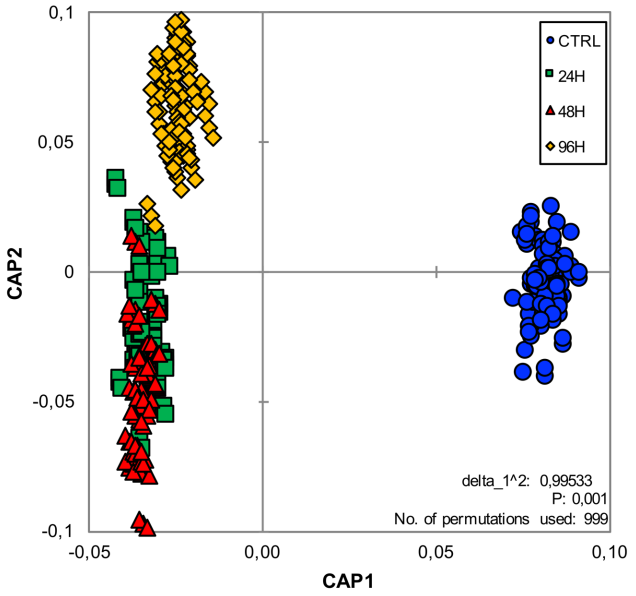

Figure 5. Canonical ordination for the discriminant analysis of spectral data of GCs at different culture time. The values of δ_1^2 (0.99533), P (0.001) and number of permutations (999) are highlighted.

Discussion

GCs have been proposed and widely used as an *in vitro* model to assess normal and abnormal ovarian functionality, and to acquire knowledge on the mechanisms and factors involved in oocyte competence acquisition and quality (8,9,21). In fact, GCs carry out many important functions inside the follicle,

including the production of essential nutrients used as an energy source during oocyte maturation, through carbohydrate and lipid metabolism, glucose employment, and lipid oxidation and storage in lipid droplets (2–5). The impairment of their lipid metabolism, leading for example to an excessive amount of lipids, determines several damaging effects not only in GCs, but also in the oocyte, which displays decreased rates of nuclear maturation and fertilization (6,7). Hence, the use of GCs as *in vitro* models makes it necessary to elucidate the culture-induced alterations in their metabolic processes and molecular architecture, in order to avoid biases in the experimental procedures. In effect, a differential uptake/utilization of lipids by *in vitro* cultured GCs has been already described by a recent study from Singh and colleagues (10).

In this light, using FTIRM, we defined the macromolecular composition and structure of fresh GCs, and we highlighted the biochemical changes induced on these follicular cells by *in vitro* culture for 24, 48 and 96 hours. **CTRL** spectra showed a wider distribution in the PCA space, with respect to the other experimental groups, which could be associated with the biological variability of samples. The results of PCA showed a clear segregation of **CTRL** spectra from all the other experimental groups, both taken together, or separately. It is noteworthy that the *in vitro* culture of GCs causes alterations that minimize spectral differences related to the biological variability. The loadings corresponding to PC1 of the three pair-wise PCAs highlight that the most discriminant spectral features among the experimental groups are always those associated to lipids, as already reported by Singh and colleagues (10). In this study, the analysis of fresh and cultured GCs,

performed by FTIRM, confirms the overall increase of cellular lipids, and highlight a major amount of triglycerides and fatty acids, as a result of lipid accumulation. Among the main functions of GCs, lipid metabolism, consisting of lipid oxidation and storage in lipid droplets, is a crucial factor for the proper follicle development (4). The utilisation of triglycerides and fatty acids for metabolic needs relies on the lipolysis of triacylglycerol within lipid droplets, necessary to oocyte development (22). It is also known that lipid utilisation, particularly consisting of β-oxidation, is lower in cumulus-oocyte complexes matured *in vitro* (23). Hence, our results suggest that *in vitro* culture of GCs does not interrupt their functions of lipid accumulation, but impacts on their ability to utilize these molecules.

Besides supporting the lipid metabolic needs of the oocyte, GCs also play a crucial role in regulating the pattern protein phosphorylation in the oocyte, as proved by culturing oocytes with or without follicular cells (24,25). The decrease in terms of phosphate groups in cultured GCs, evidenced in this study, could suggest a mechanism by which the absence of the companion oocyte reduces this post-translational activity.

It is known that GCs normally produce, by glycolysis, pyruvate from glucose, to be transferred to the oocyte for its maturation (26). No significant change was evidenced in this study, in terms of carbohydrate metabolism, suggesting that this process is not modulated by the presence of the oocyte.

In conclusion, the metabolic changes of GCs induced by *in vitro* culture described in this study evidence a not usual condition in cell culture practice,

which indeed relies on the possibility of maintaining cells *in vitro* without expecting changes. This is true for the majority of cell types, including tumoral cells, whose metabolism and activity are almost completely aimed at cell division and proliferation (Giorgini et al., submitted to Journal of Biophotonics). Conversely, GCs metabolism changes in culture, possibly because of the absence of the companion oocyte, whose metabolism and functionalities are regulated by these cells, and, in turn, it also regulates follicular cells, in a bidirectional and continuous way.

References

1. Suh CS, Sonntag B, Erickson GF. The ovarian life cycle: A contemporary view. Rev Endocr Metab Disord 2002;3(1):5–12.
2. Chronowska E. High-throughput analysis of ovarian granulosa cell transcriptome. Biomed Res Int 2014;2014.
3. Gilchrist RB, Ritter LJ, Armstrong DT. Oocyte-somatic cell interactions during follicle development in mammals. Anim Reprod Sci 2004;82–83:431–46.
4. Gilchrist RB, Lane M, Thompson JG. Oocyte-secreted factors: Regulators of cumulus cell function and oocyte quality. Hum Reprod Update 2008;14(2):159–77.
5. Downs SM, Mosey JL, Klinger J. Fatty acid oxidation and meiotic resumption in mouse oocytes. Mol Reprod Dev 2009;76(9):844–53.
6. Wu LL-Y, Dunning KR, Yang X, Russell DL, Lane M, Norman RJ, et al. High-Fat Diet Causes Lipotoxicity Responses in Cumulus–Oocyte Complexes and Decreased Fertilization Rates. Endocrinology 2010;151(11):5438–45.
7. Yang X, Wu LL, Chura LR, Liang X, Lane M, Norman RJ, et al. Exposure to lipid-rich follicular fluid is associated with endoplasmic reticulum stress and impaired oocyte maturation in cumulus-oocyte complexes. Fertil Steril 2012;97(6):1438–43.
8. Havelock JC, Rainey WE, Carr BR. Ovarian granulosa cell lines. Mol Cell Endocrinol 2004;228(1–2):67–78.
9. Uyar A, Torrealday S, Seli E. Cumulus and granulosa cell markers of oocyte and embryo quality. Fertil Steril 2013;99(4):979–97.
10. Singh P, Amin M, Keller E, Simerman A, Aguilera P, Briton-Jones C, et al. A novel approach to quantifying ovarian cell lipid content and lipid accumulation in vitro by confocal microscopy in lean women undergoing ovarian stimulation for in vitro fertilization (IVF). J Assist Reprod Genet 2013;30(5):733–40.
11. Baker MJ, Trevisan J, Bassan P, Bhargava R, Butler HJ, Dorling KM, et al. Using Fourier transform IR spectroscopy to analyze biological materials. Nat Protoc 2014;9(8):1771–91.

12. Petibois C, Desbat B. Clinical application of FTIR imaging: New reasons for hope. Trends Biotechnol 2010;28(10):495–500.
13. Wolkers WF, Oldenhof H. In situ FTIR studies on mammalian cells. Spectroscopy 2010;24(5):525–34.
14. Matthäus C, Bird B, Miljković M, Chernenko T, Romeo M. Infrared and Raman Microscopy in Cell Biology. Methods Cell Biol 2008;89(8):275–308.
15. Borini A, Sciajno R, Bianchi V, Sereni E, Flamigni C, Coticchio G. Clinical outcome of oocyte cryopreservation after slow cooling with a protocol utilizing a high sucrose concentration. Hum Reprod 2005;21(2):512–7.
16. Movasaghi Z, Rehman S, Rehman I ur. Fourier Transform Infrared (FTIR) Spectroscopy of Biological Tissues. Appl Spectrosc Rev 2008;43(2):134–79.
17. Anderson MJ, Gorley RN, Clarke KR. PERMANOVA+ for PRIMER: Guide to Software and Statistical Methods. Plymouth, UK 2008;1–214.
18. Anderson MJ. A new method for non-parametric multivariate analysis of variance. Austral Ecol 2001;26(1):32–46.
19. Anderson MJ, Robinson J. Generalized discriminant analysis based on distances. Aust New Zeal J Stat 2003;45(3):301–18.
20. Anderson MJ, Willis TJ. Canonical analysis of principal coordinates: a useful method of contrained ordination for ecology. Ecology 2003;84(2):511–25.
21. Richardson MC, Davies DW, Watson RH, Dunsford ML, Inman CB, Masson GM. Cultured human granulosa cells as a model for corpus luteum function: relative roles of gonadotrophin and low density lipoprotein studied under defined culture conditions. Hum Reprod 1992;7(1):12–8.
22. Dunning KR, Russell DL, Robker RL. Lipids and oocyte developmental competence: The role of fatty acids and β-oxidation. Reproduction 2014;148(1).
23. Spindler RE, Pukazhenthi BS, Wildt DE. Oocyte metabolism predicts the development of cat embryos to blastocyst in vitro. Mol Reprod Dev 2000;56(2):163–71.
24. Colonna R, Cecconi S, Tatone C, Mangia F, Buccione R. Somatic cell-oocyte interactions in mouse oogenesis: Stage specific regulation of mouse

oocyte protein phosphorylation by granulosa cells. Dev Biol 1989;133:305–8.

25. Cecconi S, Tatone C, Buccione R, Mangia F, Colonna R. Granulosa cell-oocyte interactions: The phosphorylation of specific proteins in mouse oocytes at the germinal vesicle stage is dependent upon the differentiative state of companion somatic cells. J Exp Zool 1991;258(2):249–54.
26. Roberts R, Franks S, Hardy K. Culture environment modulates maturation and metabolism of human oocytes. Hum Reprod 2002;17(11):2950–6.

Chapter 4

A new insight on aging effects in human Granulosa cells: a multidisciplinary FTIR imaging spectroscopy and qPCR approach

Notarstefano et al.

(manuscript in preparation)

Introduction

Women fecundity is monthly reduced after the age of 30 years, according to a mechanism called female reproductive aging, which is thought to be determined by a gradual decline both in quality and quantity of the oocytes present in the follicles in the ovarian cortex, resulting in a reduction of fecundity (1). Also, in *in vitro* fertilisation (IVF) studies, female age was clearly determined to be one of the key factors affecting clinical outcomes (2). A retrospective study of 2017 on the effects induced by the advancing age on the success rates of Assisted Reproductive Technology (ART), reported that among women aged 30–35 years, 38.7% of the cycles led to clinical pregnancy and 33.3% to live births. In contrast, among women aged 40–44 years, only 23.6% of cycles led to clinical pregnancies and 14.8% to live births (3). Nowadays, subfertility related to female aging has become an important issue for most industrialized societies, mainly because of the increasing delay in childbearing (4,5). This has inevitably become a matter of active research in the field of ART aimed at the treatment of couple infertility, with consideration of the understanding of the causes of age-related decline of ovarian functions (2). In effect, the process of acquisition of oocyte competence, defined as the ability of an oocyte to be fertilized and to develop to the blastocyst stage, strictly depends on the follicular microenvironment (6). All the processes involved in folliculogenesis heavily rely upon bi-directional interactions between germ cells and the surrounding somatic cells (7). Granulosa cells (GCs) are known to support oocyte growth (8), control the advance of meiosis steps (9), and regulate the oocyte transcriptional activity (10). In turn, the oocyte modulates several aspects of GC development

including proliferation, differentiation, and extracellular matrix and steroid hormone production (11). Due to these connections, reproductive aging is evidently interconnected with the quality of GCs surrounding the oocyte.

The aging process is also strongly associated with radical mechanisms that induce modifications in macromolecules such as lipids, proteins, and DNA, leading to an oxidative damage in several tissues (12). Oxidative stress (OS) arises when the cell concentration of reactive oxygen species (ROS) increases, as a result of an imbalance between the production of pro-oxidants and antioxidants. This condition is partly correlated with an impairment of mitochondrial functions, as reviewed by May-Panloup and colleagues (13). ROS modulate the whole reproductive functions, such as oocyte maturation, steroidogenesis, corpus luteal functions, luteolysis, fertilization, embryo development, and pregnancy (14,15). OS affecting GCs plays a role in the modulation of ovarian senescence, hence in the age-related decline of fertility (16).

Fourier Transform Infrared (FTIR) spectroscopy is a well-established spectroscopic technique, broadly applied in life sciences for the study of the biomolecular building and composition of cells and tissues samples. FTIR spectral bands are analysed in terms of position, intensity and width, making it possible to detect functional groups, bonding types and conformations of the most relevant biological molecules (proteins, lipids, sugars and nucleic acids) (17). In particular, the coupling of IR spectrometers with visible light microscopes facilitates the application of FTIR in various biomedical fields for diagnostic purposes, thanks to the possibility to map, in a fast and label-free

way, non-homogeneous samples, retrieving subtle biochemical changes at a cellular level. In this sense, FTIR spectroscopy provides at the same time and on the same sample, unique chemical and morphological information about the composition and the structural building blocks of all the biomolecules of interest, which can be directly related to cellular activity, metabolism and oxidative stress status (18–20).

In a previous work, we obtained, for the first time, the infrared molecular fingerprint of human oocytes retrieved from patients with different age: alterations in plasma membrane, protein pattern, nucleic acids and metabolic processes were observed in oocytes from 39-year- old patients (21). Encouraged by these results, in the present study, we analysed the alterations occurring in human GCs in women of different ages by exploiting FTIR Imaging spectroscopy and qPCR analysis.

Experimental section

The study was carried out on human GCs and was approved by the Internal Review Board of Tecnobios Procreazione, in full accordance with the Declaration of Helsinki (World Med. Ass. 2013). To participate in this investigation, each patient signed a written consent, which included the donation of GCs. All samples were anonymous and marked by a code and hence it was impossible to correlate them to a physical person.

Luteinized GCs sample collection

20 patients enrolled in an in vitro fertilization program, were recruited according to the following inclusion criteria: regular ovulatory menstrual cycles; FSH < 10 IU/I on day 3 of the menstrual cycle; non-smokers, and without ovarian infertility nor endometriosis diagnosis. Controlled ovarian stimulation was induced using leuprorelin (Enantone, Takeda, Rome, Italy) and rFSH (Gonal-F, Serono, Rome, Italy, or Puregon Organon, Rome, Italy). HCG at 10,000 IU (Gonasi, Amsa, Rome, Italy) was administered when one or more follicles reached a diameter of ca. 23 mm (22). At the end of the treatment, from each patient, a pool of luteinized GCs was collected from all the follicles, according to the following protocol. The follicular fluid was centrifuged at 1100 x g for 10 min and the pellet was resuspended in 2 mL of gamete medium, overlaid on 1 mL pure sperm 50% (obtained by pure sperm 80 and gamete buffer medium) and centrifuged again at 1600x g for 13 min to separate GCs from the red blood cells. After centrifugation, GCs were recovered, placed in 1mL of NaCl 0.9% solution and then centrifuged at 300x g for 10 minutes. The supernatant was discarded, and the pellet was resuspended in 1mL of NaCl 0.9% solution and centrifuged again at 300 x g for 10 minutes.

An aliquot of each GCs sample was immediately frozen in liquid nitrogen and stored at -80°C till q-PCR analysis. The remaining aliquots of GCs samples were deposited without any fixation process onto CaF_2 optical windows (1-mm thick, 13-mm diameter) and air-dried for 30 min for the vibrational analysis, which was carried out within 24 hours. Previous

experiments carried out in our laboratories evidenced that samples prepared as above, showed a good stability in time, providing homogeneous and reliable data sets.

GCs samples were divided into two groups based on patients age: **Young**, n. 10 GCs from women of 27-34 years old (mean age 31.2±2.20); **Old**, n. 10 GCs from women of 40-46 years old (mean age 42.5±1.84).

FTIR imaging measurements and data analysis

FTIR measurements were carried out by using a Bruker VERTEX 70 interferometer coupled with a Hyperion 3000 Vis-IR microscope at the IR beamline SISSI, ELETTRA synchrotron. The spectrometer was equipped with a liquid nitrogen cooled bidimensional Focal Plane Array (FPA) detector which enabled simultaneous acquisition of 4096 spectra (64x64 pixels, pixel size ~2.56 μm) on an area of 164x164 μm, to perform the imaging analysis. On each sample, the visible image was acquired with a 15X condenser/objective, and then IR maps were obtained in transmission mode (164x164 μm^2, 256 scans for each detector pixel with a spectral resolution of 4 cm^{-1}). Background spectra were acquired on clean regions of CaF_2 optical windows. During all the measurements, the microscope camera was purged with nitrogen in order to avoid atmospheric contamination (H_2O and CO_2). Nevertheless, raw spectra of all IR maps were corrected for the contribution of atmospheric carbon dioxide and water vapour with the Atmospheric Compensation routine of OPUS 7.0 software (Bruker Optics GmbH) and then vector normalized in the 4000–900 cm^{-1} spectral range. For each sample, the total absorbance

cartogram, representing the total intensity of the infrared absorption, was generated by integrating over the spectral range 3050–900 cm^{-1} (OPUS 7.1 software package, Bruker Optics, Ettlingen, Germany). In addition, to evaluate the topographical distribution of lipids, proteins, phosphates and carbohydrates, false colour images were calculated by integrating the IR maps under the following spectral regions: 3050–2800 cm^{-1} (CH_2 and CH_3 moieties of lipids, LIPIDS), 1723–1481 cm^{-1} (Amide I and II bands of proteins, PROTEINS), 1273–1191 cm^{-1} (asymmetric stretching mode of phosphates, PH1), and 1137–1022 cm^{-1} (symmetric stretching mode of phosphates, and C-O stretching mode in carbohydrates, PH2-GLYCO).

To avoid problems owing to the non-homogeneous layer of cells on CaF_2 optical windows, and to possible scattering effects due to the presence of NaCl, on each IR map 10 areas (~20x20 μm^2) were chosen, containing only mono layer cells, from which the average IR spectra were extracted. Spectra having at 1660 cm^{-1} a peak height lower than 0.07 a.u. were discarded; less than 10% of initial spectra were cut off in all the experimental groups.

These selected IR spectra were first submitted to multivariate analysis to differentiate them according patients' age. PCA (Principal Components Analysis) was carried out by using an in-house developed algorithm with R Studio (RStudio: Integrated Development for R. RStudio, Inc., Boston, MA). Then, the same IR spectra were integrated under the following spectral regions (OPUS 7.1 software package, Bruker Optics, Ettlingen, Germany): 3050–2800 cm^{-1} (representative of all cellular lipids, LIPIDS); 1723–1481 cm^{-1} (Amide I and II bands, representative of all cellular proteins, PROTEINS); 1273–1191

cm^{-1} (ν_{asym} PO_2^-, asymmetric stretching mode of phosphates, PH1), and 1137–1022 cm^{-1} (ν_{sym} PO_2^-, symmetric stretching mode of phosphates and C-O stretching mode in carbohydrates, PH2-GLYCO). The sum of the integrated areas 3050–2800 and 1765–950 cm^{-1} was considered indicative of the total cell dried biomass (CELL). If not differently reported, band assignment is given on the basis of the review of Movasaghi and colleagues (23).

The convoluted 3050–2800 cm^{-1} and 1723–1481 cm^{-1} spectral ranges were also analysed by a Peak Fitting procedure. In this regard, absorbance average spectra were interpolated in the aforementioned ranges, two-point baseline corrected and fitted with a Gaussian algorithm (GRAMS/AI 7.02, Galactic Industries, Inc., Salem, NH). To identify the underlying component bands, the number of peaks together with their centre values was carefully identified according to second derivative results. Mean values of area and wavelength were obtained for each component peak.

RNA extraction and cDNA synthesis

Total RNA extraction from GCs was performed using Minikit RNAeasy® (Qiagen) extraction kits, following the manufacturer's protocol. Total RNA extracts were eluted in 20 μL of RNAse-free water. Final RNA concentrations were determined with a NanoDrop™ 1000 Spectrophotometer (Thermo Scientific) and RNA integrity was verified by Gel Red (Biotium, UK) staining of 28S and 18S ribosomal RNA fragments on 1% agarose gel. RNA was stored at -80°C until use. Total RNA was treated with DNAse (10 IU at 37°C for 10 min, MBI Fermentas); a total amount of 2 μg of RNA was used for cDNA

synthesis, employing the SuperScript-II cDNA Synthesis Kit (Invitrogen, Life Technologies).

Real-time polymerase chain reaction

Relative quantification of gene expression was performed with the SYBR Green method in a CFX96 Real-Time PCR system (Bio-Rad). Duplicate PCRs were carried out for each sample analyzed. Reactions were set mixing 1 μL diluted (1/10) cDNA, 5 μL of 2× SYBR Green PCR Master Mix (Bio-Rad), containing SYBR Green as a fluorescent intercalating agent, 0.1 μM of forward and reverse primers, and 3.8 μL of milliQ water.

The thermal profile was as follows: enzyme activation at 95°C for 3 min; 45 cycles of denaturation (10 sec at 95°C), followed by 20 sec annealing at 60°C for *gapdh*, *rpl13a*, *igfbp3*, and 56°C for *foxo3*, *sirt3*, *sirt1*, *igf1*, *sod2*, and 20 sec elongation at 72°C. Fluorescence was monitored at the end of each cycle. Dissociation curves for primer specificity and absence of primer-dimer formation check were performed and consistently showed a single peak. Glyceraldehyde-3-phosphate dehydrogenase (*gapdh*) and ribosomal protein L13a (*rpl13a*) were used as internal controls to enable result standardization by eliminating variations in mRNA and cDNA quantity and quality (24). These genes were chosen because their mRNA levels did not vary between experimental groups. No amplification products were observed in negative controls and no primer–dimer formations were observed in the control templates. Data were analysed using CFX Manager Software version 3.1 (Bio-Rad). The quantification method was based on a ΔΔCt calculation

implemented with the Pfaffl equation, to improve accuracy by accounting for varied reaction efficiencies depending on primers (25,26). Modification of gene expression is represented with respect to zero. Primer sequences used are reported in Table 1.

Gene	Forward primer (5' – 3')	Reverse primer (5' – 3')	Acc number	Gene ID
gapdh	GTGAAGGTCGGAGTCAACG	GGTGAAGACGGCCAGTGGACTC	NM_002046.5	2597
rpl13a	TCTGGAGGACTGTAAGAGGTATGC	AGACGCACAATCTTGAGAGCAG	NM_012423.3	23521
foxo3	AGAAGTTCCCCAGCGACTTG	TTTGAGGGTCTGCTTTGCCC	NM_001455.3	2309
sirt3	GCATTCCAGACTTCAGATCGC	GTGGCAGAGGCAAAGGTTCC	NM_012239.5	23410
sirt1	CGGTTCCTACTGCGCGA	CCGAACAGAAGGTTATCTGGCT	NM_001142498.1	23411
igf1	TCAGAGCAGATAGAGCCTGC	ATGGTGTGCATCTTCACCTTCAA	NM_001111285.2	3479
sod2	GCCAGGAGAGGAAAGCACCAG	TAGTCGTAGGGCAGGTCGG	NM_001322819.1	6648
igfbp3	AATGCTAGTGAGTCGGAGGA	TACGGCAGGGACCATATTCTG	NM_000598.4	3486

Table 1. List of primers used in gene expression analyses by Real-Time qPCR. *gapdh*: glyceraldehyde-3-phosphate dehydrogenase; *rpl13a*: ribosomal protein L13a; *foxo3*: forkhead box O3; *sirt3*: sirtuin 3; *sirt1*: sirtuin 1; *igf1*: insulin like growth factor 1; *sod2*: superoxide dismutase 2; *igfbp3*: insulin like growth factor binding protein 3.

Statistical analysis

Normally distributed data deriving from integration and Peak Fitting of IR spectra, and from gene expression analysis were presented as mean ± S.D. Significant differences between experimental groups were determined by Student's t-tests, using the statistical software package Prism6 (Graphpad Software, Inc. USA). Statistical significance was set at $p < 0.05$. Asterisks

denote significant differences from the control group (* = $p < 0.05$; ** = $p < 0.01$; *** = $p < 0.001$; **** = $p < 0.0001$).

Results

Human GCs samples retrieved from two groups of patients named **Young** (mean age 31.2±2.20) and **Old** (mean age 42.5±1.84) were analysed using FTIR Imaging spectroscopy and qPCR assays.

Imaging analysis

The topographical distribution of lipids, proteins, phosphates and carbohydrates was first qualitatively assessed in GCs samples by false colour scale images created by integrating IR maps under the following spectral regions: 3050–2800 cm^{-1} (CH_2 and CH_3 moieties of lipids, LIPIDS), 1723–1481 cm^{-1} (Amide I and II bands of proteins, PROTEINS), 1273–1191 cm^{-1} (asymmetric stretching mode of phosphates, PH1), and 1137–1022 cm^{-1} (symmetric stretching mode of phosphates, and C-O stretching mode in carbohydrates, PH2-GLYCO) (Figure 1).

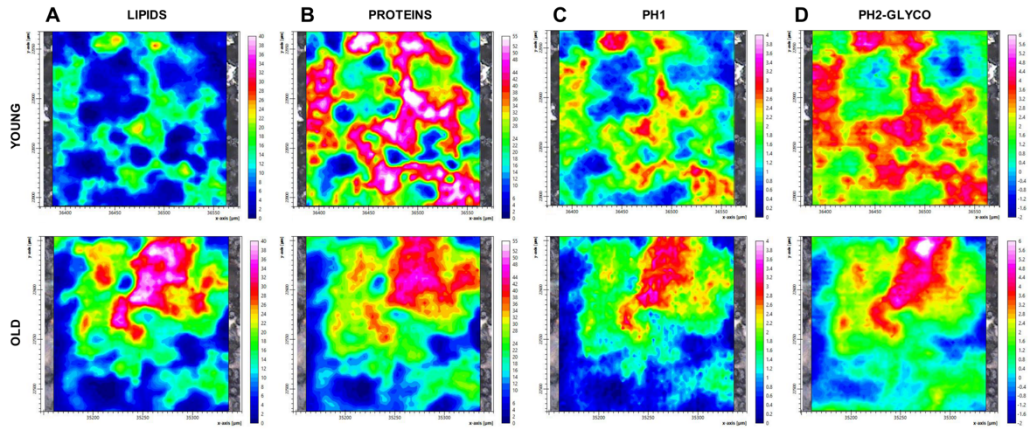

Figure 1. FTIR Imaging spectroscopy. False colour images integrated under the following spectral ranges: (**A**) 3050-2836 cm^{-1} (CH_2 and CH_3 moieties of lipids, **LIPIDS**), (**B**) 1723-1481 cm^{-1} (Amide I and II bands of proteins, **PROTEINS**), (**C**) 1273–1191 cm^{-1} (asymmetric stretching mode of phosphates, **PH1**), and (**D**) 1137–1022 cm^{-1} (symmetric stretching mode of phosphates, and C-O stretching mode in carbohydrates, **PH2-GLYCO**).

The intensity of the signal associated with a specific band provides information on both the presence and the localization of the corresponding molecular/chemical groups. In particular, in **Old** GCs with respect to **Young** ones, a visible increase of lipids and a decrease of the protein content were observed. No variation was detected in phosphates and carbohydrates amount.

Multivariate analysis

For a more detailed understanding of the spectral differences in GCs from patients with different age, **Old** and **Young** IR spectra were submitted to multivariate analysis.

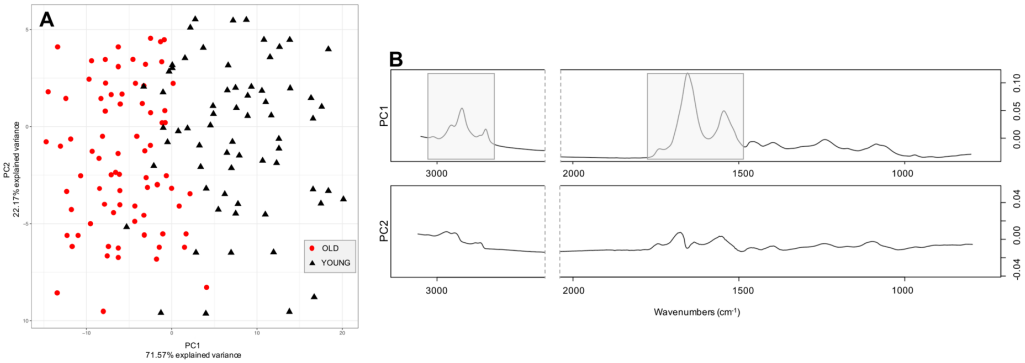

Figure 2. Principal Components Analysis. PCA scatter plot (A) and PC1 and PC2 loadings (B) of **Old** and **Young** experimental groups. Highlighted in grey on PC1 the most visible discriminant features in the 3050-2800 cm^{-1} and 1765-1481 cm^{-1} spectral regions.

Figure 2A shows the PCA scatter plot of GCs spectra from the two experimental groups. A clear segregation of **Old** and **Young** spectra was observed along PC1 axis (71.57 % of the system variance). The analysis of PC1 loading confirmed that the most visible discriminant features were in the 3050-2800 cm^{-1} and 1765-1481 cm^{-1} spectral regions, attributable respectively to lipids and proteins (Figure 2B), as previously highlighted by imaging analysis. No difference was found according to PC2 or other PCs.

Vibrational data analysis

To perform a semi-quantitative analysis on the macromolecular composition of **Old** and **Young** GCs, specific band area ratios were calculated using the aforementioned area integrals described in the Experimental section (Figure 3). The analysis of the numerical variation of these ratios led to the following considerations: (i) the total amount of cellular lipids (LIPIDS/CELL), calculated as the ratio between the integrated area in the 3050–2800 cm^{-1} spectral region (corresponding to CH_2 and CH_3 symmetric and asymmetric stretching modes of lipids) and CELL value, showed a significant increase in **Old** GCs with respect to **Young** ones ($p = 0.0029$, Figure 3A); (ii) the total amount of cellular proteins (PROTEINS/CELL), calculated as ratio between the integrated area of the 1723-1481 cm^{-1} spectral region (corresponding to Amide I and II bands) and CELL value, showed a significant decrease in **Old** GCs with respect to **Young** ones ($p = 0.0006$, Figure 3B); (iii) the ratio PH1/CELL, obtained comparing the integrated area of the band at ~1240 cm^{-1} (corresponding to the asymmetric stretching mode of phosphates) with the CELL value, did not show a significant alteration between the two experimental groups ($p = 0.1103$, Figure 3C); (iv) similarly, the ratio PH2-GLYCO/CELL, calculated comparing the integrated areas of the band at ~1080 cm^{-1} (corresponding to the symmetric stretching mode of phosphates, and the stretching of C-O bonds in carbohydrates) with the CELL value, did not change between the two experimental groups ($p = 0.6335$, Figure 3D).

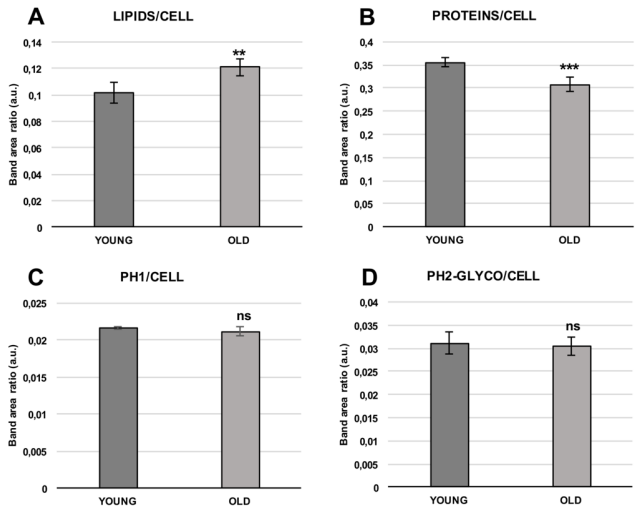

Figure 3. Numerical variations of the following band area ratios for the **Old** and **Young** experimental groups: **LIPIDS/CELL** (spectral region 3050-2800 cm^{-1}) (A); **PROTEINS/CELL** (spectral region 1723-1481 cm^{-1}) (B); **PH1/CELL** (band at ~1240 cm^{-1}) (C); **PH2-GLYCO/CELL** (band at ~1080 cm^{-1}) (D). Asterisks above columns indicate statistical differences among groups (* = $p<0.05$; ** = $p<0.01$; *** = $p<0.001$; **** = $p<0.0001$; Student's t test).

For a deeper analysis of the spectral profile of lipids and proteins in **Old** and **Young** experimental groups, the fit of the 3050–2800 cm^{-1} and 1790–1480 cm^{-1} spectral regions was performed, enabling determination of the position and the area integral of all the underlying bands. In Table 2, the selected underlying bands are reported in terms of position and vibrational assignment.

Spectral region	Wavenumber (cm^{-1})	Assignment	Label		
3050 – 2800 cm^{-1}	3012	=CH stretching vibration	CH	LIPIDS	
	2957	CH_3 asymmetric stretching vibrations	CH3		
	2869	CH_3 symmetric stretching vibrations			
	2925	CH_2 asymmetric stretching vibrations	CH2		
	2852	CH_2 symmetric stretching vibrations			
1790 – 1480 cm^{-1}	1746	C=O ester moieties stretching vibrations	C=O ESTERS		
	1694	β-turn structures vibrational modes	BETA	FOLDED	AI
	1680, 1627, 1613	β-sheet structures vibrational modes			
	1659	α-helix structures vibrational modes	HELIX		
	1640	Random coil structures vibrational modes	RANDOM		

Table 2. Fit of the 3050-2800 cm^{-1} and 1790-1480 cm^{-1} spectral regions. The results of the fit are reported as position and area integral the selected underlying bands.

The statistical analysis of band area ratios calculated using the aforementioned area integrals (Table 2) highlighted the following variations in **Old** GCs with respect to **Young** ones (Figure 4): (i) the ratio CH/LIPIDS significantly increased ($p = 0.0235$, Figure 4A); (ii) the ratio CH/CH2 significantly increased ($p = 0.0013$, Figure 4B); (iii) the ratio CH2/CH3 did not significantly change between the two experimental groups ($p = 0.3499$, Figure 4C); (iv) the ratio C=O ESTERS/AI significantly increased ($p = 0.0225$, Figure 4D); (v) the ratio FOLDED/AI significantly decreased ($p = 0.0049$, Figure 4E); (vi) the ratio HELIX/AI significantly decreased ($p = 0.0009$, Figure 4F); (vii) the ratio BETA/AI significantly decreased ($p = 0.0365$, Figure 4G); (viii) the ratio RANDOM/AI significantly increased, consistently with the opposite trend observed in the FOLDED/AI ratio ($p = 0.0064$, Figure 4H).

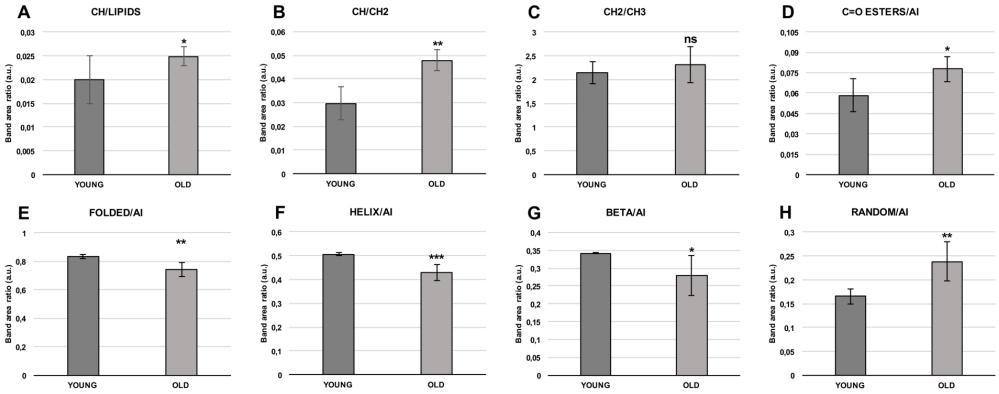

Figure 4. Numerical variations of the following band area ratios for the **Old** and **Young** groups: (A) 3010 cm^{-1} (CH) / peaks in the 3050-2800 cm^{-1} range (LIPIDS); (B) 3010 cm^{-1} (CH) / 2925+2852 cm^{-1} (CH_2); (C) 2925+2852 cm^{-1} (CH_2) / 2957+2869 cm^{-1} (CH_3); (D) 1746 cm^{-1} (C=O ester) / bands in the 1695-1625 cm^{-1} interval (AI); (E) 1659+1694+1680+1627+1613 cm^{-1} (FOLDED) / AI; (F) 1659 cm^{-1} (HELIX) / AI; (G) 1694+1680+1627+1613 cm^{-1} (BETA) / AI; (H) 1640 cm^{-1} (RANDOM) / AI. Asterisks above columns indicate statistical differences among groups (* = $p<0.05$; ** = $p<0.01$; *** = $p<0.001$; ns = not significant; Student's t test).

Gene expression analysis

Figure 5 shows the numerical variations in the expression of the genes of interest. Molecular analysis demonstrated that patient's age affects GCs not only in terms of their importance in the follicular development, but also in their response to oxidative stress. In **Old** GCs, a significant decrease of *igf1* ($p = 0.005$, Figure 5A), *sirt1* ($p = 0.0465$, Figure 5D) and *sod2* ($p = 0.001$, Figure

5F) gene expression was observed with respect to **Young**. Conversely, *igfbp3* ($p < 0.0001$, Figure 5B) and *foxo3* ($p = 0.0233$, Figure 5C) decreased their expression. The variation in *sirt3* relative mRNA levels was not statistically significant ($p = 0.4128$, Figure 5E).

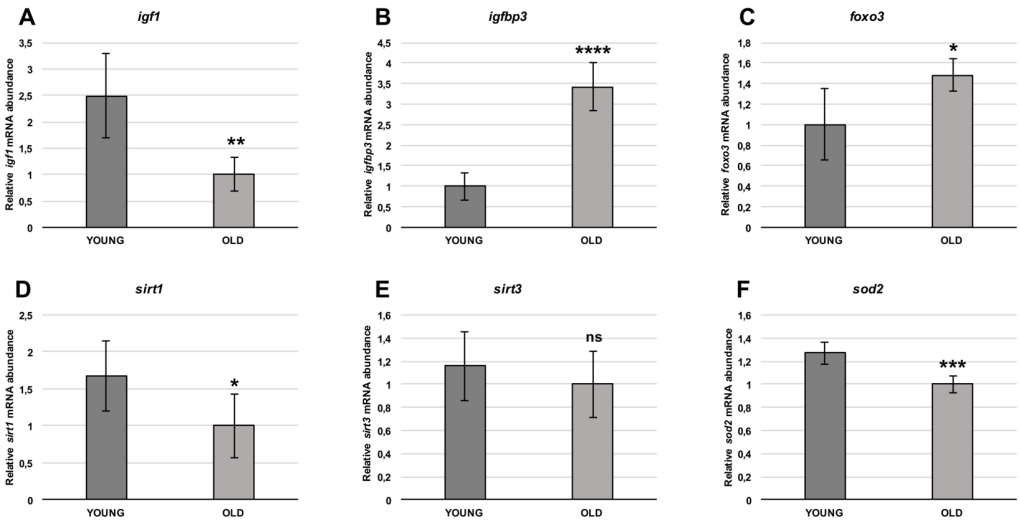

Figure 5. Transcription profiles of investigated genes. (A) *igf1*: insulin like growth factor 1 ($p = 0.005$); (B) *igfbp3*: insulin like growth factor binding protein 3 ($p < 0.0001$); (C) *foxo3*: forkhead box O3 ($p = 0.0233$); (D) *sirt1*: sirtuin 1 ($p = 0.0465$); (E) *sirt3*: sirtuin 3 ($p = 0.4128$); (F) *sod2*: superoxide dismutase 2 ($p = 0.001$). Asterisks above columns indicate statistical differences among groups (* = $p<0.05$; ** = $p<0.01$; *** = $p<0.001$; **** = $p<0.0001$; ns = not significant; Student's t test).

Discussion

In this study, we compared the spectral features and the expression of genes involved in age-induced stress response in human GCs from patients at different age, in order to obtain a deeper insight into the effects of aging on the follicular microenvironment.

False colour images obtained from IR maps allow visualisation of the distribution of lipids, proteins, phosphates and carbohydrates: **Old** GCs are seen to be characterized by a larger amount of lipids, while proteins decreased; aging appeared not to affect the amount of phosphates and carbohydrates. These differences in lipid and protein metabolism were also confirmed by PCA analysis, performed on IR spectra which showed a clear segregation of **Old** and **Young** GCs. Particularly, the loading corresponding to PC1 highlighted the most relevant discriminant features as the lipid region, the protein region, and the ester carbonyl moieties band.

To focus on these differences, a more detailed analysis of lipid and protein spectral regions was performed by calculating meaningful band area ratios. The lipid amount increases in **Old** GCs, and more notably, aging determines a significant increase of C=O ester carbonyl groups and =CH groups. These findings confirm that lipids are a target of cellular oxidation and are in accordance with previous works focused on FTIR investigation of the effects of female aging on human oocytes (21) and, more specifically, on oxidative stress (27,28).

A significant decrease in protein content was detected in **Old** GCs, together with an alteration of secondary structure, as evidenced by the increase of random structures and the decrease of both helix, β-sheet and β-turn ones, taken both individually (HELIX/AI and BETA/AI) or in combination (FOLDED/AI). All these findings are consistent with a process of age-related OS, which alters the main cellular macromolecules. In particular, it is known that aging leads to the loss of efficiency of the so-called Protein Quality

Control (PQC) systems, causing changes in protein structure, partly due to oxidative modifications (29,30).

In order to confirm and clarify the results obtained by FTIR spectroscopy, we performed an expression analysis of several genes involved in cellular pathways activated as a response to age-induced stress in GCs.

The IGF signalling has a role in modulating rates of cell renewal, and in increasing proliferation and metastasis of cancer cells, as reviewed by Pollak and colleagues (31). In this study, the IGF system was investigated due to its crucial role in mammalian reproduction (32). IGFs, the ligands of this system, amplify the actions of FSH on GCs, stimulating cell proliferation and steroidogenesis, the transcription of several genes, the activity of aromatase, and the expression of LH receptor (33,34). IGF-1 was thought to be produced only in the liver and then transported to sites of action, but it showed to be synthesized also in other organs (31): in effect, it is the main IGF produced in animal follicles (35,36), and it was found to be strongly expressed by healthy but not atretic follicles (37); IGF-1 has a key role in the regulation of GCs functions in human GCs (38), in the induction of follicle growth (39), and in steroid secretion (40). The bioavailability and the activity of IGFs depend on specific binding proteins named IGFBPs (31), which, in the ovary, antagonize FSH action by sequestering IGFs produced by GCs (41). The expression of these binding proteins depends on follicle maturation stage and status (32). In the present study, we investigated the expression of *igf1* and *igfbp3*, and we found an opposite trend in their expression according to age: in **Old** GCs, *igf1* significantly decreased its mRNA level, conversely *igfbp3* increased. A similar

trend was found by Klein in follicular fluids of old patients (42), suggesting a reduced local IGF-1 effect, which may impair oocyte maturation.

The regulation of aging effects by the insulin like pathway also involves other molecules, like the transcription factor *foxo3*, which is part of the Forkhead box O subfamily (FOXO), and which is implicated in a wide range of processes, such as metabolism, cellular stress response and aging, and in the ovary, is a crucial regulator and suppressor of follicular activation (43). Our results showed a significant decrease of the expression levels of *foxo3* in **Old** GCs, consistent with the results reported by Castrillon and colleagues, who found that *foxo3a* null mice showed an age-dependent decline in reproductive fitness, becoming sterile by 15 weeks of age (44,45). Moreover, in support to our results, there is the study of Yamamoto and colleagues, who reported a weak negative correlation between *foxo3* mRNA levels in granulosa cells and patients' age (46).

Studies focusing on aging mechanisms performed on yeast led to the detection of sirtuins, a family of conserved enzymes, whose roles affect several functions increasing life span and the health of organisms (47). *Sirtuins* are considered anti-aging genes, since it is now clear that their activation determines an extension of life span (48). We investigated variations in the expression of *sirt1* and *sirt3*, two of the seven human sirtuins, which are localized in the nucleus and in the mitochondria, respectively (49). SIRT1 is involved in many biological functions, such as activation of stress response pathways and alterations in metabolism (30), together with cell senescence, oxidative stress, inflammation and autophagy/apoptosis (50), and acts via

deacetylation of several substrates, such as p53 (51,52) and forkhead proteins (53,54) to influence stress resistance in cells. In the present study, we found a significant decrease in the expression of *sirt1* in **Old** GCs, consistent with the results obtained by Han and colleagues (55). They observed a difference in the expression of *sirt1* related to the ovarian reserve status of the patient; in particular, the expression level was lower in GCs from poor ovarian response (POR) and polycystic ovarian syndrome (PCOS) women, suggesting that the expression levels of *sirt1* in GCs decreased with increasing age and depleted ovarian function. The other sirtuin analysed here is *sirt3*, localized in the mitochondria of mammalian cells (56). Among the functions of SIRT3, there is the regulation of mitochondrial functions, as demonstrated by the increase of respiration and the decrease of reactive oxygen species production following its overexpression (57). Although not statistically significant, we report a decrease in the expression of this gene in **Old** GCs, in accordance with the results of Pacella-Ince and colleagues, who described a decrease in the levels of *sirt3* mRNA in granulosa and cumulus cells from women with reduced ovarian reserve and advanced age (58).

Mitochondrial manganese-superoxide dismutase (SOD2) acts as anti-oxidant. It reduces superoxide anion to hydrogen peroxide and molecular oxygen, and, then, catalase converts hydrogen peroxide to water and molecular oxygen (59). This ability to protect cells against ROS accumulation declines with aging; moreover, mitochondria, in addition to being the major source of ROS, have also been determined to be one of the key targets of aging-related oxidative stress (60). In **Old** GCs, the expression of *sod2* (mitochondrial

manganese-sod) was significantly lower with respect to **Young** ones. This age-related decrease is in accordance with the results of Tatone and colleagues (14), who found a significant decrease of *sod1*, *sod2* and *catalase* in GCs of old patients, supporting the hypothesis that ovarian aging could be due to damages induced by OS on cellular components (61).

In conclusion, the results obtained in this study by coupling FTIR and qPCR analyses highlighted that female aging results in a profound alteration in the biochemical composition of GCs, mainly resulting in alterations in lipid metabolism and peroxidation, and in the impairment of protein quantity and folding. In addition, the occurrence of oxidative stress, and the impairment of the molecular machinery regulating the response to age-induced stress in GCs were also found, leading to a deeper knowledge in the molecular mechanisms involved in ovarian senescence.

References

1. Kupka M, D'Hooghe T, Ferraretti AP, de Mouzon J, Erb K, Castilla JA, et al. Assisted reproductive technology in Europe, 2011: results generated from European registers by ESHRE. Hum Reprod 2016;31(2):dev319.
2. Tatone C. Cellular and molecular aspects of ovarian follicle ageing. Hum Reprod Updat 2008;14(2):131–42.
3. O'Brien YM, Ryan M, Martyn F, Wingfield MB. A retrospective study of the effect of increasing age on success rates of assisted reproductive technology. Int J Gynecol Obstet 2017;138(1):42–6.
4. te Velde ER, Pearson PL. The variability of female reproductive aging. Hum Reprod Update 2002;8(2):141–54.
5. Baird DT, Collins J, Egozcue J, Evers LH, Gianaroli L, Leridon H, et al. Fertility and ageing. Hum Reprod Update 2005;11(3):261–76.
6. Al-Edani T, Assou S, Ferrières A, Bringer Deutsch S, Gala A, Lecellier CH, et al. Female aging alters expression of human cumulus cells genes that are essential for oocyte quality. Biomed Res Int 2014;2014:1–10.
7. Kidder GM, Vanderhyden BC. Bidirectional communication between oocytes and follicle cells: ensuring oocyte developmental competence. Can J Physiol Pharmacol 2010;88(4):399–413.
8. Brower PT, Schultz RM. Intercellular communication between granulosa cells and mouse oocytes: Existence and possible nutritional role during oocyte growth. Dev Biol 1982;90(1):144–53.
9. Eppig JJ. Intercommunication between mammalian oocytes and companion somatic cells. BioEssays 1991;13(11):569–74.
10. De La Fuente R, Eppig JJ. Transcriptional activity of the mouse oocyte genome: companion granulosa cells modulate transcription and chromatin remodeling. Dev Biol 2001;229(1):224–36.
11. Gilchrist RB, Lane M, Thompson JG. Oocyte-secreted factors: Regulators of cumulus cell function and oocyte quality. Hum Reprod Update 2008;14(2):159–77.
12. Sohal RS. Role of oxidative stress and protein oxidation in the aging process. Free Radic Biol Med 2002;33(1):37–44.

13. May-Panloup P, Boucret L, Chao de la Barca J-M, Desquiret-Dumas V, Ferré-L'Hotellier V, Morinière C, et al. Ovarian ageing: the role of mitochondria in oocytes and follicles. Hum Reprod Update 2016;22(6):725–43.
14. Tatone C, Carbone MC, Falone S, Aimola P, Giardinelli A, Caserta D, et al. Age-dependent changes in the expression of superoxide dismutases and catalase are associated with ultrastructural modifications in human granulosa cells. Mol Hum Reprod 2006;12(11):655–60.
15. Agarwal A, Gupta S, Sharma RK. Role of oxidative stress in female reproduction. Reprod Biol Endocrinol 2005;3:28.
16. Ávila J, González-Fernández R, Rotoli D, Hernández J, Palumbo A. Oxidative Stress in Granulosa-Lutein Cells From In Vitro Fertilization Patients. Reprod Sci 2016;23(12):1656–61.
17. Baker MJ, Trevisan J, Bassan P, Bhargava R, Butler HJ, Dorling KM, et al. Using Fourier transform IR spectroscopy to analyze biological materials. Nat Protoc 2014;9(8):1771–91.
18. Petibois C, Desbat B. Clinical application of FTIR imaging: New reasons for hope. Trends Biotechnol 2010;28(10):495–500.
19. Wolkers WF, Oldenhof H. In situ FTIR studies on mammalian cells. Spectroscopy 2010;24(5):525–34.
20. Matthäus C, Bird B, Miljković M, Chernenko T, Romeo M. Infrared and Raman Microscopy in Cell Biology. Methods Cell Biol 2008;89(8):275–308.
21. Gioacchini G, Giorgini E, Vaccari L, Ferraris P, Sabbatini S, Bianchi V, et al. A new approach to evaluate aging effects on human oocytes: Fourier transform infrared imaging spectroscopy study. Fertil Steril 2014;101(1):120–7.
22. Borini A, Sciajno R, Bianchi V, Sereni E, Flamigni C, Coticchio G. Clinical outcome of oocyte cryopreservation after slow cooling with a protocol utilizing a high sucrose concentration. Hum Reprod 2005;21(2):512–7.
23. Movasaghi Z, Rehman S, Rehman I ur. Fourier Transform Infrared (FTIR) Spectroscopy of Biological Tissues. Appl Spectrosc Rev 2008;43(2):134–79.

24. Bustin SA, Benes V, Garson JA, Hellemans J, Huggett J, Kubista M, et al. The MIQE Guidelines: Minimum Information for Publication of Quantitative Real-Time PCR Experiments. Clin Chem 2009;55(4):611–22.
25. Pfaffl MW. A new mathematical model for relative quantification in real-time RT-PCR. Nucleic Acids Res 2001;29(9):45e–45.
26. Vandesompele J, De Preter K, Pattyn F, Poppe B, Van Roy N, De Paepe A, et al. Accurate normalization of real-time quantitative RT-PCR data by geometric averaging of multiple internal control genes. Genome Biol 2002;3(7):research0034.1-0034.11.
27. Rodríguez-Casado A, Alvarez I, Toledano A, de Miguel E, Carmona P. Amphetamine effects on brain protein structure and oxidative stress as revealed by FTIR microspectroscopy. Biopolymers 2007;86(5–6):437–46.
28. Vileno B, Jeney S, Sienkiewicz A, Marcoux PR, Miller LM, Forró L. Evidence of lipid peroxidation and protein phosphorylation in cells upon oxidative stress photo-generated by fullerols. Biophys Chem 2010;152(1–3):164–9.
29. Gregersen N, Bross P, Vang S, Christensen JH. Protein Misfolding and Human Disease. Annu Rev Genomics Hum Genet 2006;7(1):103–24.
30. Haigis MC, Yankner BA. The Aging Stress Response. Mol Cell 2010;40(2):333–44.
31. Pollak MN, Schernhammer ES, Hankinson SE. Insulin-like growth factors and neoplasia. Nat Rev Cancer 2004;4(7):505–18.
32. Adashi EY. Insulin-like growth factors as determinants of follicular fate. J Soc Gynecol Investig 1995;2(6):721–6.
33. McGee EA, Strauss JF. Ovarian Hormone Synthesis. In: Endocrinology: Adult and Pediatric. Elsevier Inc.; 2016. p. 2192–2206.e5.
34. Monget P, Bondy C. Importance of the IGF system in early folliculogenesis. Mol Cell Endocrinol 2000;163(1–2):89–93.
35. Giudice L, Cataldo N, van Vessel HJHM, Yap OW, Chandrasekher Y. Growth Factors in Normal Ovarian Follicle Development. Semin Reprod Med 1996;14(3):179–96.
36. Zhou J, Bondy C. Anatomy of the human ovarian insulin-like growth factor system. Biol Reprod 1993;48(3):467–82.

37. Oliver JE, Aitman TJ, Powell JF, Wilson CA, Clayton RN. Insulin-like growth factor I gene expression in the rat ovary is confined to the granulosa cells of developing follicles. Endocrinology 1989;124(6):2671–9.
38. Mason HD, Margara R, Winston RM, Seppala M, Koistinen R, Franks S. Insulin-like growth factor-I (IGF-I) inhibits production of IGF-binding protein-1 while stimulating estradiol secretion in granulosa cells from normal and polycystic human ovaries. J Clin Endocrinol Metab 1993;76(5):1275–9.
39. Di Blasio AM, Viganó P, Ferrari A. Insulin-like growth factor-II stimulates human granulosa-luteal cell proliferation in vitro. Fertil Steril 1994;61(3):483–7.
40. Yong EL, Baird DT, Yates R, Reichert LE, Hillier SG. Hormonal regulation of the growth and steroidogenic function of human granulosa cells. J Clin Endocrinol Metab 1992;74(4):842–9.
41. Ling NC, Liu XJ, Malkowski M, Guo YL, Erickson GF, Shimasaki S. Structural and functional studies of insulin-like growth factor binding proteins in the ovary. Growth Regul 1993;3(1):70–4.
42. Klein NA, Battaglia DE, Woodruff TK, Padmanabhan V, Giudice LC, Bremner WJ, et al. Ovarian Follicular Concentrations of Activin, Follistatin, Inhibin, Insulin-Like Growth Factor I (IGF-I), IGF-II, IGF-Binding Protein-2 (IGFBP-2), IGFBP-3, and Vascular Endothelial Growth Factor in Spontaneous Menstrual Cycles of Normal Women of Advanced. J Clin Endocrinol Metab 2000;85(12):4520–5.
43. Brenkman AB, Burgering BMT. FoxO3a eggs on fertility and aging. Trends Mol Med 2003;9(11):464–7.
44. Castrillon DH, Miao L, Kollipara R, Horner JW, DePinho RA. Suppression of ovarian follicle activation in mice by the transcription factor Foxo3a. Science (80-) 2003;301(5630):215–8.
45. Hosaka T, Biggs WH, Tieu D, Boyer AD, Varki NM, Cavenee WK, et al. Disruption of forkhead transcription factor (FOXO) family members in mice reveals their functional diversification. Proc Natl Acad Sci U S A 2004;101(9):2975–80.

46. Yamamoto H, Yamashita Y, Saito N, Hayashi A, Hayashi M, Terai Y, et al. Lower FOXO3 mRNA expression in granulosa cells is involved in unexplained infertility. J Obstet Gynaecol Res 2017;43(6):1021–8.
47. Haigis MC, Sinclair D a. Mammalian Sirtuins: Biological Insights and Disease Relevance. Annu Rev Pathol Mech Dis 2010;5(1):253–95.
48. Tissenbaum HA, Guarente L. Increased dosage of a sir-2 gene extends lifespan in Caenorhabditis elegans. Nature 2001;410(6825):227–30.
49. Westphal CH, Dipp MA, Guarente L. A therapeutic role for sirtuins in diseases of aging? Trends Biochem Sci 2007;32(12):555–60.
50. Michan S, Sinclair D. Sirtuins in mammals: insights into their biological function. Biochem J 2007;404(1):1–13.
51. Luo J, Nikolaev AY, Imai S, Chen D, Su F, Shiloh A, et al. Negative control of p53 by Sir2alpha promotes cell survival under stress. Cell 2001;107(2):137–48.
52. Vaziri H, Dessain SK, Ng Eaton E, Imai SI, Frye RA, Pandita TK, et al. hSIR2(SIRT1) functions as an NAD-dependent p53 deacetylase. Cell 2001;107(2):149–59.
53. Brunet A, Sweeney LB, Sturgill JF, Chua KF, Greer PL, Lin Y, et al. Stress-dependent regulation of FOXO transcription factors by the SIRT1 deacetylase. Science (80-) 2004;303(5666):2011–5.
54. Motta MC, Divecha N, Lemieux M, Kamel C, Chen D, Gu W, et al. Mammalian SIRT1 represses forkhead transcription factors. Cell 2004;116(4):551–63.
55. Han Y, Luo H, Wang H, Cai J, Zhang Y. SIRT1 induces resistance to apoptosis in human granulosa cells by activating the ERK pathway and inhibiting NF-κB signaling with anti-inflammatory functions. Apoptosis 2017;0(0):0.
56. Michishita E, Park JY, Burneskis JM, Barrett JC, Horikawa I. Evolutionarily conserved and nonconserved cellular localizations and functions of human SIRT proteins. Mol Biol Cell 2005;16(10):4623–35.
57. Shi T, Wang F, Stieren E, Tong Q. SIRT3, a mitochondrial sirtuin deacetylase, regulates mitochondrial function and thermogenesis in brown adipocytes. J Biol Chem 2005;280(14):13560–7.

58. Pacella-Ince L, Zander-Fox D., Lane M. Mitochondrial SIRT3 and its target glutamate dehydrogenase are altered in follicular cells of women with reduced ovarian reserve or advanced maternal age. Hum Reprod 2014;29(7):1490–9.
59. Scandalios JG. Oxidative stress: molecular perception and transduction of signals triggering antioxidant gene defenses. Braz J Med Biol Res 2005;38(7).
60. Landis GN, Tower J. Superoxide dismutase evolution and life span regulation. Mech Ageing Dev 2005;126(3):365–79.
61. Li Q, Geng X, Zheng W, Tang J, Xu B, Shi Q. Current understanding of ovarian aging. Sci China Life Sci 2012;55(8):659–69.

Chapter 5

Ovarian endometriosis affects Granulosa Cells Endocannabinoid system

Gioacchini et al.

(manuscript in preparation)

Introduction

Granulosa cells (GCs) play a very important role in oocyte maturation supporting competence acquisition and cytoplasmic maturation and keeping the oocyte under meiotic arrest and subsequently by inducing meiotic resumption (1). Despite its importance, the network of molecular signals exchanged between the oocyte and the surrounding GCs is far from being fully understood, although in recent years, many of these signals have been identified and their functions characterized. Among them, molecules belonging to Endocannabinoid system (ECS) have been recently considered (2).

Endocannabinoids are derivatives of fatty acids acting as endogenous ligands of the G-protein coupled cannabinoid receptors CB1 and CB2, mimicking some of the central and peripheral effects of D9–tetrahydrocannabinol (D9–THC), the psychoactive component of marijuana (3,4). In addition to the receptors CB1 and CB2 other endocannabinoid-binding receptors belonging to ECS have been identified (5). Among them are the GPR55 receptor (6) and the non-cannabinoid classified receptor, the transient receptor potential vanilloid 1 (TRPV1) (7). N-arachidonoylethanolamine, known as anandamide (AEA), and 2–arachidonoylglycerol (2–AG) are the best-characterized endocannabinoids (8). The biosynthesis of both AEA and 2–AG takes place through different pathways, but the most important enzymes involved are N–acylphosphatidylethanolamine phospholipase D (NAPE–PLD) for AEA and the diacylglycerol lipase (DAGL) for 2–AG (9,10). The effects of endocannabinoids could be limited by several enzymes, such as the fatty acid

amide hydrolase (FAAH) and the monoacylglyceride lipase (MAGL), which can hydrolyse AEA and 2AG respectively (11,12). Several studies have demonstrated the role of ECS in the female reproductive system and in folliculogenesis (2,13) and its implication on several ovarian pathologies including endometriosis has been demonstrated (14–16).

Endometriosis, one of the most common gynaecological diseases, is associated with subfertility but the molecular mechanisms through which it negatively affects reproduction are not still well identified. The cause of subfertility in endometriosis seems to be multifactorial (17). The lower success with in vitro fertilization (IVF) treatment of women affected by endometriosis (18), could be probably related to the impaired follicular microenvironment rather than reduced endometrial receptivity (19,20). The endocannabinoid system has recently been shown to affect specific mechanisms (inflammation, cell proliferation and cell survival) that are critical to endometriosis establishment and maintenance (21) and alterations of ECS have been shown in eutopic and ectopic endometria of patients with endometriosis (14). However, a possible modulation of GCs' ECS in women affected by ovarian endometriosis is still unexplored. In the present study, we aimed to examine for the first time the effects of ovarian endometriosis on Granulosa Cells Endocannabinoid System related to lipid and carbohydrate metabolism. Taking into account the importance of GCs metabolism in folliculogenesis, the results presented here strengthen the molecular mechanisms activated by endometriosis inducing alteration of ovarian follicle environment.

Experimental section

The study was carried out on human GCs retrieved at Tecnobios Procreazione, in full accordance with the Declaration of Helsinki (World Med. Ass. 2013). To participate in this investigation, each patient signed a written consent, which included the donation of GCs. All samples were anonymous and marked by a code and hence it was impossible to correlate them to a physical person.

Luteinized GCs sample collection

20 patients enrolled in an in vitro fertilization program, were recruited according to the following inclusion criteria: regular ovulatory menstrual cycles; FSH < 10 IU/I on day 3 of the menstrual cycle; non-smokers; 35 ± 2.8 years old. Controlled ovarian stimulation was induced using leuprorelin (Enantone, Takeda, Rome, Italy) and rFSH (Gonal-F, Serono, Rome, Italy, or Puregon Organon, Rome, Italy). HCG at 10,000 IU (Gonasi, Amsa, Rome, Italy) was administered when one or more follicles reached a diameter of ca. 23 mm (22).

At the end of the treatment, from each patient, a pool of luteinized GCs was collected from all the follicles, according to the following protocol. The follicular fluid was centrifuged at 1100x g for 10 min and the pellet was resuspended in 2 mL of gamete medium, overlaid on 1 mL pure sperm 50% (obtained by pure sperm 80 and gamete buffer medium) and centrifuged again at 1600x g for 13 min to separate GCs from the red blood cells. After centrifugation, GCs were recovered, placed in 1mL of NaCl 0.9% solution and

then centrifuged at 300x g for 10 minutes. The supernatant was discarded, and the pellet was resuspended in 1mL of NaCl 0.9% solution and centrifuged again at 300x g for 10 minutes.

An aliquot of each GCs sample was immediately frozen in liquid nitrogen and stored at -80°C till q-PCR analysis.

10 women received the diagnosis of tubal, idiopathic or male infertility, and represented the control group (**CTRL**); 10 women had a diagnosis of unilateral ovarian endometriosis: from these women, we obtained GCs from the endometriosis-affected ovary (**ENDO**).

RNA extraction and cDNA synthesis

Total RNA extraction from GCs was performed using Minikit RNAeasy® (Qiagen) extraction kits, following the manufacturer's protocol. Total RNA extracts were eluted in 20 μL of RNAse-free water. Final RNA concentrations were determined with a NanoDrop™ 1000 Spectrophotometer (Thermo Scientific) and RNA integrity was verified by Gel Red (Biotium, UK) staining of 28S and 18S ribosomal RNA fragments on 1% agarose gel. RNA was stored at -80°C until use. Total RNA was treated with DNAse (10 IU at 37°C for 10 min, MBI Fermentas); a total amount of 2 μg of RNA was used for cDNA synthesis, employing the SuperScript-II cDNA Synthesis Kit (Invitrogen, Life Technologies).

Real-time polymerase chain reaction

Relative quantification of gene expression was performed with the SYBR Green method in a CFX96 Real-Time PCR system (Bio-Rad). Duplicate PCRs were carried out for each sample analyzed. Reactions were set mixing 1 μL diluted (1/10) cDNA, 5 μL of 2 × SYBR Green PCR Master Mix (Bio-Rad), containing SYBR Green as a fluorescent intercalating agent, 0.1 μM of forward and reverse primers, and 3.8 μL of milliQ water.

The thermal profile was as follows: enzyme activation at 95°C for 3 min; 45 cycles of denaturation (10 sec at 95°C), followed by 20 sec annealing at 60°C for all the examined genes and 20 sec elongation at 72°C. Fluorescence was monitored at the end of each cycle. Dissociation curves for primer specificity and absence of primer-dimer formation check were performed and consistently showed a single peak. Glyceraldehyde-3-phosphate dehydrogenase (*gapdh*) and ribosomal protein L13a (*rpl13a*) were used as internal controls to enable result standardization by eliminating variations in mRNA and cDNA quantity and quality (23). These genes were chosen because their mRNA levels did not vary between experimental groups. No amplification products were observed in negative controls and no primer–dimer formations were observed in the control templates. Data were analyzed using CFX Manager Software version 3.1 (Bio-Rad). The quantification method was based on a ΔΔCt calculation implemented with the Pfaffl equation, to improve accuracy by accounting for varied reaction efficiencies depending on primers (24,25). Modification of gene expression is represented with respect to zero. Primer sequences used are reported in Table 1.

Gene	Forward primer (5' – 3')	Reverse primer (5' – 3')	Acc number	Gene ID
gapdh	GTGAAGGTCGGAGTCAACG	GGTGAAGACGGCCAGTGGACTC	NM_002046.5	2597
rpl13a	TCTGGAGGACTGTAAGAGGTATGC	AGACGCACAATCTTGAGAGCAG	NM_012423.3	23521
trpv1	GACTTCAAGGCTGTCTTCATCATCC	CAGGGAGAAGCTCAGGGTGCGC	NM_018727.5	7442
gpr55	ACAGTTTGCAGTCCACATCC	ACGCTTCCGTACATGCTGAC	NM_005683.3	9290
cnr1	CCACTCCCGCAGCCTCCG	ATCAGGCAAAACGCCACCAC	NM_001160226.1	1268
cnr2	GGTGACAGAGATAGCCAATG	GCCAATGAACAGGTATGAGG	NM_001841.2	1269
naple-pld	CAGTAGAACAGTGTGTACGTAGAAG	CACTTCTAGAATGATACCCAAACTC	NM_001122838.1	222236
faah	TATGAGACTGACAACTATACCATGC	CACGAAATCACCTTTGAAGTTCTGT	NM_001441.2	2166
dagl	GTGCCATCCGACATCATTGC	GCGGAGCATCTCTTGTGAAT	NM_006133.2	747
magl	ATGCAGAAAGACTACCCTGGGC	TTATTCCGAGAGAGCACGC	NM_001003794.2	11343
pparα	CTGGAAGCTTTGGCTTTACG	GTTGTGTGACATCCCGACAG	NM_001001928.2	5465
pparγ	TTCAGAAATGCCTTGCAGTG	CACCTCTTTGCTCTGCTCCT	NM_001330615.1	5468
srebp1	TGACCGACATCGAAGGTGAA	AAAGTGCAATCCATGGCTCC	NM_001005291.2	6720
fasn	CAGAGCAGCCATGGAGGAG	TAGAGCCCCGCCTTCCAG	NM_004104.4	2194
glut1	TGGCATCAACGCTGTCTTCT	AGCCAATGGTGGCATACACA	NM_006516.2	6513
glut9	TCCAGAGGGGCATGAAAACTC	CGAGCAGGACCAGTCCAATTT	NM_001001290.1	56606

Table 1. List of primers used in gene expression analyses by Real-Time qPCR. *gapdh*: glyceraldehyde-3-phosphate dehydrogenase; *rpl13a*: ribosomal protein L13a; *trpv1*: transient receptor potential cation channel subfamily V member 1; *gpr55*: G protein-coupled receptor 55; *cnr1*: cannabinoid receptor 1; *cnr2*: cannabinoid receptor 2; *nape-pld*: N-acyl phosphatidylethanolamine phospholipase D; *faah*: fatty acid amide hydrolase; *dagla/b*: diacylglycerol lipase alpha/beta; *magl*: monoglyceride lypase; *pparα*: peroxisome proliferator activated receptor alpha; *pparγ*: peroxisome proliferator activated receptor gamma; *srebp1*: sterol regulatory element binding transcription protein 1; *fasn*: fatty acid synthase; *glut1*: glucose transporter 1 (*slc2a1*: solute carrier family 2 member 1); *glut9*: glucose transporter 9 (*slc2a9*: solute carrier family 2 member 9).

FTIR imaging and data analysis

Fourier Transform InfraRed (FTIR) measurements were carried out by using a Bruker VERTEX 70 interferometer coupled with a Hyperion 3000 Vis-

IR microscope at the IR beamline SISSI, ELETTRA synchrotron. The spectrometer was equipped with a liquid nitrogen cooled bidimensional Focal Plane Array (FPA) detector which enabled the simultaneous acquisition of 4096 spectra (64x64 pixels, pixel size ~2.56 μm) on an area of 164x164 μm, to perform the imaging analysis. On each sample, the visible image was acquired with a 15X condenser/objective, and then IR maps were obtained in transmission mode (164x164 μm^2, 256 scans for each detector pixel with a spectral resolution of 4 cm^{-1}). IR maps were compared with background spectral images taken on clean regions of CaF_2 windows. During all the measurements, the microscope camera was purged with nitrogen in order to avoid atmospheric contamination (H_2O and CO_2). Nevertheless, raw spectra of all IR maps were corrected for the contribution of atmospheric carbon dioxide and water vapour with the compensation routine of OPUS 7.0 software (Bruker Optics GmbH) and then vector normalized in the 4000–900 cm^{-1} spectral range. For each sample, the total absorbance cartogram, representing the total intensity of the infrared absorption, was generated by integrating within the spectral range 3050–900 cm^{-1} (OPUS 7.1 software package, Bruker Optics, Ettlingen, Germany). In addition, to evaluate the presence of lipids, fatty acids, and carbohydrates, false colour images were calculated by integrating the IR maps under the following spectral regions: 3050–2800 cm^{-1} (CH_2 and CH_3 moieties of lipids, LIPIDS), 1780–1715 cm^{-1} (TRIGLYCERIDES), and 1137–1022 cm^{-1} (symmetric stretching mode of phosphates, and C-O stretching mode in carbohydrates, Ph2-GLYCO).

Results

Figure 1 shows the modulation of gene expression of the receptors involved in ECS by the ovarian endometriosis. A significant increase of gene expression was observed for all the receptors investigated here in GCs from patients affected by endometriosis. In particular, a substantial increase of gene expression was evidenced for *trpv1* and *gpr55* receptors ($p<0.0001$) (Figure 1 C-D), while *cnr1* and *cnr2* showed a moderate induction of gene expression ($p<0.5$) (Figure 1 A-B).

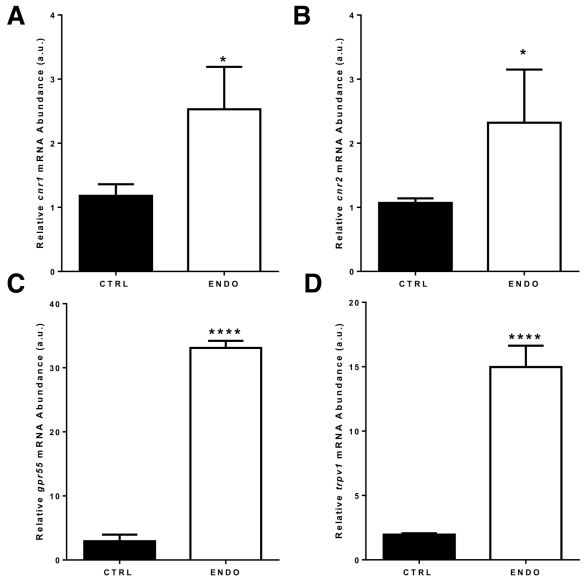

Figure 1. Transcription profiles of investigated genes. Asterisks above columns indicate statistical differences among groups (* = $p<0.05$; ** = $p<0.01$; *** = $p<0.001$; **** = $p<0.0001$; Student's t test). (**A**) ***cnr1***: cannabinoid receptor 1; (**B**) ***cnr2***: cannabinoid receptor 2; (**C**) ***grp55***: G protein-coupled receptor 55; (**D**) ***trpv1***: transient receptor potential cation channel subfamily V member 1.

Figure 2 shows the expression levels of genes coding for key enzymes involved in endocannabinoids (AEA and 2-AG) synthesis and degradation. A significant increase ($p<0.001$) was observed for *nape-pld*, the enzyme involved on AEA synthesis, concomitant with a significantly decrease ($p<0.001$) of *faah*, the enzyme responsible for the AEA degradation (Figure 2 A-B). In contrast, the enzymes involved on both synthesis and degradation of 2-AG, *dagl* ($p=0,6877$) and *magl* ($p=0,0771$) respectively, were not affected by endometriosis. (Figure 2 C-D).

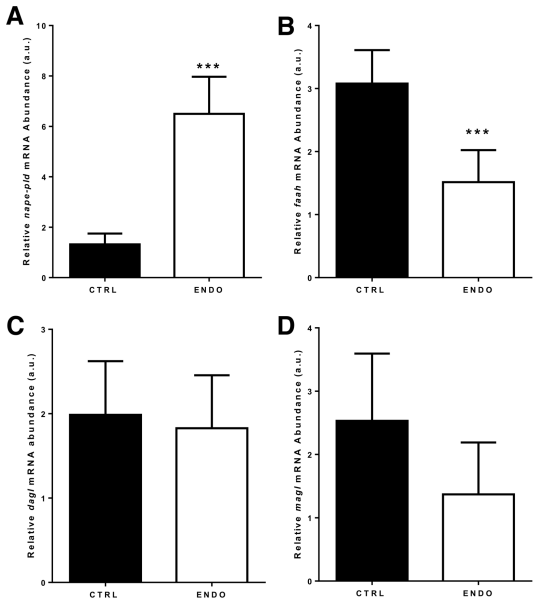

Figure 2. Transcription profiles of investigated genes. Asterisks above columns indicate statistical differences among groups (* = $p<0.05$; ** = $p<0.01$; *** = $p<0.001$; **** = $p<0.0001$; Student's t test). (**A**) ***nape-pld***: N-acyl phosphatidylethanolamine phospholipase D; (**B**) ***faah***: fatty acid amide hydrolase; (**C**) ***dagl***: diacylglycerol lipase; (**D**) ***magl***: monoglyceride lypase.

Figure 3 shows expression levels of genes involved in lipids metabolism. A statistically significant increase was found for all the enzymes involved in lipid metabolism investigated, such as peroxisome proliferator-activated receptors *ppars* α ($p<0.001$) and γ ($p<0.001$), the transcription factor sterol regulatory element-binding protein 1 (*srebp1*) ($p<0.001$) and fatty acid synthase (*fasn*) ($p<0.01$) (Figure 3 A-D).

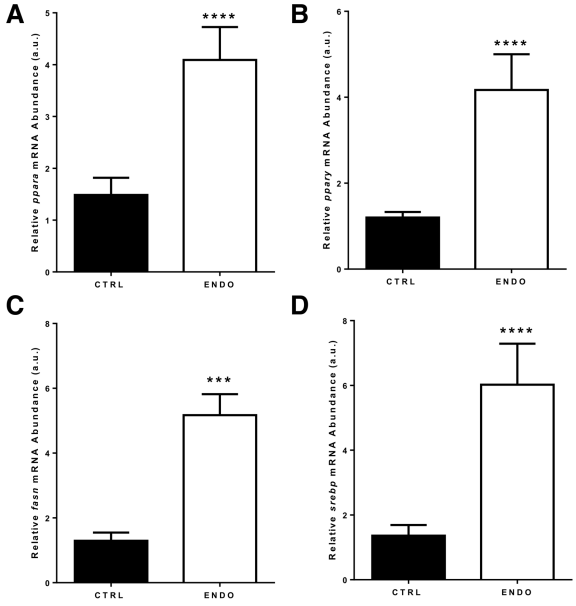

Figure 3. Transcription profiles of investigated genes. Asterisks above columns indicate statistical differences among groups (* = $p<0.05$; ** = $p<0.01$; *** = $p<0.001$; **** = $p<0.0001$; Student's t test). (**A**) ***pparα***: peroxisome proliferator activated receptor alpha; (**B**) ***pparγ***: peroxisome proliferator activated receptor gamma; (**C**) ***fasn***: fatty acid synthase; (**D**) ***srebp1***: sterol regulatory element binding transcription protein 1.

Figure 4 shows quantification and distribution of lipids and triglycerides by FTIR imaging analysis. Chemical maps visually show with a false colour scale, the intensity of the signal associated with a specific integrated band, giving information on both the presence and the localization of the molecule/chemical group under consideration. An increase was found in endometriosis affected patients for total lipids (B) and triglycerides (D) content with the respect to the control ones (A and C).

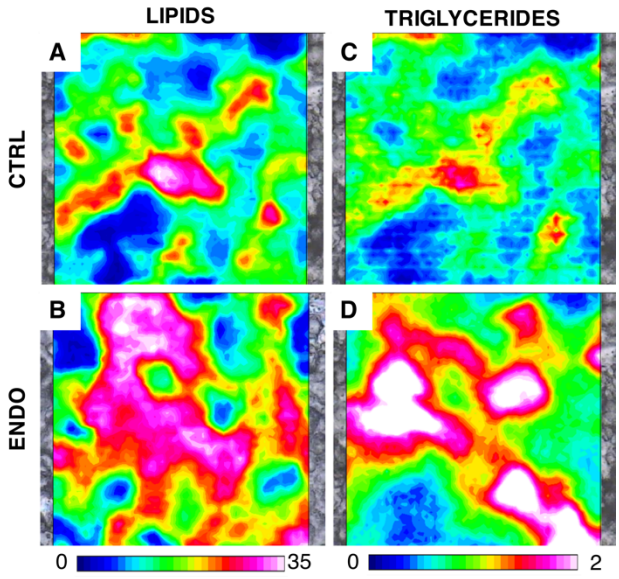

Figure 4. FTIR Imaging spectroscopy. False colour images integrated under the following spectral ranges: (**A**-**B**) 3050-2836 cm^{-1} (CH_2 and CH_3 moieties of lipids, **LIPIDS**), (**C**-**D**) 1780-1715 cm-1 (νCOO, stretching mode of triglycerides ester moieties, **TRIGLYCERIDES**).

Figure 5 shows expression levels of genes involved in glucose transport and carbohydrates quantification and distribution by FTIR imaging analysis. A statistically significant decrease was found for both the glucose transporter investigated, (A) *glut1* ($p<0.01$) and (B) *glut9* ($p<0.001$). Conversely, a total carbohydrate content decrease was found in GCs from endometriosis-affected patients (D) with the respect to the control ones (C).

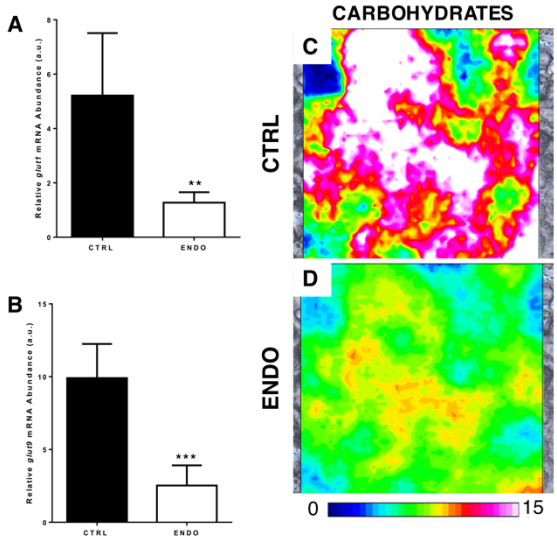

Figure 5. Gene expression. Asterisks above columns indicate statistical differences among groups (* = $p<0.05$; ** = $p<0.01$; *** = $p<0.001$; **** = $p<0.0001$; Student's t test). (**A**) *glut1*: glucose transporter 1; (**B**) *glut9*: glucose transporter 9. **FTIR Imaging spectroscopy**. (**C-D**) False colour images integrated under the spectral range 1090–1022 cm^{-1} (C-O stretching mode in carbohydrates, **CARBOHYDRATES**).

Discussion

It has been established that the proper maturation of an oocyte is the result of mutual interactions of the oocyte with its follicular environment (26). Oocyte competence depends on the quality of the follicular microenvironment, and the presence of adequate bidirectional somatic cell-to-oocyte signalling is a prerequisite for both oocytes and GCs competence (27–32). In this light, the intraovarian paracrine communications are fundamental to the modulation of oocyte growth and maturation and the ability of GCs to maintain a proper and correct metabolism represents a fundamental requirement for this to happen. Oocytes lack the ability to carry out glycolysis and cholesterol biosynthesis, and to transport certain amino acids; thus, the surrounding somatic cells must compensate for these metabolic insufficiencies (33).

It is also known that the persistence of endometriotic lesions results in a status of chronic inflammation within the ovary (34). A variety of bioactive molecules, such as cytokines, growth factors, and apoptotic mediators, have been shown to affect ovulation, fertilization, embryo quality, and implantation. Toya and collaborators demonstrated that these factors can affect GCs cell cycle and in turn adversely affect folliculogenesis (35). Here for the first time we investigated the possible effects of ovarian endometriosis on GCs ECS and in turn on cellular metabolism.

The emerging picture, drawn by recent works, is that the ECS plays a central role in mammalian reproductive organs, probably by modulating their homeostasis via autocrine/paracrine loops. The available evidence supports

the concept that distinct ECS components (i.e., endocannabinoids, their metabolic enzymes and receptors) can respond to fertility signals by cooperating with hormones, cytokines and other signalling molecules, and that the dysregulated (decreased or increased) ECS signalling adversely affects reproduction (36–38). Immunohistochemical examination of normal human ovaries indicated that the ECS was present and widely expressed in the ovarian medulla and cortex, with more pronounced CNRs immunoreactivity in the GCs of primordial, primary, secondary, tertiary follicles, corpus luteum and corpus albicans (2). Instead, the AEA metabolizing enzymes, FAAH and NAPE-PLD, were only found in growing secondary and tertiary follicles, and in corpus luteum and corpus albicans (2). This massive presence of ECS within the ovary demonstrated that this organ is able to produce AEA and that such molecule plays a fundamental role in folliculogenesis, oocyte maturation and ovulation, taking also into account that the oocytes have been shown to express CNR1 and CNR2 receptors (39).

In this regard, AEA may activate different signalling pathways depending on the specific receptor engaged. To date, three endocannabinoid receptors have been shown to bind endocannabinoids at an extracellular site: CNR1, CNR2 and GPR55. The first two are well-characterized (40), and their relevance for reproduction is well defined.

The last receptor, investigate here, is the transient receptor potential vanilloid 1 (TRPV1), which is the natural target of capsaicin, the pungent ingredient of hot peppers (41) and is also the target of AEA, but not 2-AG. The AEA-TRPV1 interaction occurs at a cytosolic binding site, and triggers

a signal transduction that explains how AEA may play a physiological control of several cell functions through TRPV1 (42). TRPV-1 expression is susceptible to modulation by inflammatory and pathological processes and is involved in the signal transduction of a wide range of stimuli, including cell death by apoptosis and autophagy (43,44). Results obtained in the present study clearly demonstrated that ovarian endometriosis induces in GCs an up regulation of all the receptors suggesting that several signalling pathways have been modulated, regulating cell metabolism and survival. The results here presented clearly also demonstrated an upregulation of the ECS represented by modulation of the enzymatic machinery regulating EAE metabolism. It is important to note that the cells have kept several backup routes to produce AEA "on demand" under different conditions and that the N-acyl phosphatidylethanolamine phospholipase D (NAPE-PLD) is the most prominent AEA synthase (45), whereas the fatty acid amide hydrolase (FAAH), that cleaves AEA into ethanolamine and arachidonic acid (ARA), is the main degradative enzyme (46). Both NAPE-PLD and FAAH are involved in the control of folliculogenesis. In this light, the up regulation of NAPE-PLD concomitant with the decrease of FAAH shown here could suggests that, under the stimulus of the presence of endometriotic lesions, GCs not only became more responsive to endogenous endocannabinoids, but also, they increase their capability to synthesize endocannabinoids by themselves.

Additional targets of eCBs are the peroxisome proliferator-activated receptors (PPARs) (47). Various eCBs and related molecules have been found to regulate lipid and glucose metabolism, as well as inflammatory responses,

by activating either PPARα or PPARγ (48), although a role for PPAR-mediated endocannabinoid signalling in reproduction remains unknown. PPARγ expression has been reported in mammalian ovaries with higher levels in GCs and lower levels in theca cells and corpus luteum of rodents and ruminants (49). In particular, PPARγ has been identified in follicles at all stages of development and it has been shown that levels increase during follicle growth and decrease after the LH surge (50,51). Since PPARγ expression is predominant in GCs, it can be hypothesized that its activity influences the GCs/oocyte cross talk, supporting their mutual maturation (52). In this respect, the results obtained here let us hypothesize that the activation of ECS, in particular through the activation of PPARγ, results in lipid metabolism activation as indicated by the increase of all enzymes investigated involved on lipid synthesis and by the lipids and triglycerides accumulation indicated by FTIR imaging analysis.

Glucose is an essential nutrient for mammalian oocyte. It is employed as an energy source via glycolysis and the tricarboxylic acid (TCA) cycle (53). Glucose enters cells either by an active process via sodium-coupled glucose transporters (SGLTs) or through facilitative glucose transporters (GLUTs) (54). Therefore, the expression of GLUTs in the surrounding GCs may be strongly related to the deregulation of glucose metabolism found here, as demonstrated by the decrease of the glucose transporters *glut1* and *glut9* mRNA levels and by the decrease of total carbohydrates content as evidenced by FTIR imaging analysis.

In conclusion, the endocannabinoid system is recognized as key system in regulating cell metabolism and function. In the present study, we report results that reveal a novel molecular network through which endometriosis activates the endocannabinoid system of GCs and in turn affect cell metabolism. All these results further highlight the potential of this system on the detrimental effects of endometriosis on female fertility.

References

1. Sánchez F, Smitz J. Molecular control of oogenesis. Biochim Biophys Acta - Mol Basis Dis 2012;1822(12):1896–912.
2. El-Talatini MR, Taylor AH, Elson JC, Brown L, Davidson AC, Konje JC. Localisation and function of the endocannabinoid system in the human ovary. PLoS One 2009;4(2).
3. Di Marzo V. "Endocannabinoids" and other fatty acid derivatives with cannabimimetic properties: Biochemistry and possible physiopathological relevance. Biochim Biophys Acta - Lipids Lipid Metab 1998;1392(2–3):153–75.
4. Childers SR, Breivogel CS. Cannabis and endogenous cannabinoid systems. Drug Alcohol Depend 1998;51(1–2):173–87.
5. Karasu T, Marczylo TH, Maccarrone M, Konje JC. The role of sex steroid hormones, cytokines and the endocannabinoid system in female fertility. Hum Reprod Update 2011;17(3):347–61.
6. Ross RA. The enigmatic pharmacology of GPR55. Trends Pharmacol Sci 2009;30(3):156–63.
7. Di Marzo V, De Petrocellis L. Endocannabinoids as regulators of transient receptor potential (TRP) channels: A further opportunity to develop new endocannabinoid-based therapeutic drugs. Curr Med Chem 2010;17(14):1430–49.
8. Pertwee RG, Ross RA. Cannabinoid receptors and their ligands. Prostaglandins Leukot Essent Fatty Acids 66(2–3):101–21.
9. Okamoto Y, Tsuboi K, Ueda N. Enzymatic formation of anandamide. Vitam Horm 2009;81:1–24.
10. Ueda N, Tsuboi K, Uyama T, Ohnishi T. Biosynthesis and degradation of the endocannabinoid 2-arachidonoylglycerol. BioFactors 2011;37(1):1–7.
11. Fezza F, De Simone C, Amadio D, Maccarrone M. Fatty acid amide hydrolase: a gate-keeper of the endocannabinoid system. Subcell Biochem 2008;49:101–32.
12. Dinh TP, Carpenter D, Leslie FM, Freund TF, Katona I, Sensi SL, et al. Brain monoglyceride lipase participating in endocannabinoid inactivation. Proc Natl Acad Sci U S A 2002;99(16):10819–24.

13. Wenger T, Ledent C, Csernus V, Gerendai I. The central cannabinoid receptor inactivation suppresses endocrine reproductive functions. Biochem Biophys Res Commun 2001;284(2):363–8.
14. Sanchez AM, Vigano P, Mugione A, Panina-bordignon P, Candiani M. The molecular connections between the cannabinoid system and endometriosis. Mol Hum Reprod 2012;18(12):563–71.
15. Ayakannu T, Taylor AH, Willets JM, Konje JC. The evolving role of the endocannabinoid system in gynaecological cancer. Hum Reprod Update 21(4):517–35.
16. Juan C-C, Chen K-H, Wang P-H, Hwang J-L, Seow K-M. Endocannabinoid system activation may be associated with insulin resistance in women with polycystic ovary syndrome. Fertil Steril 2015;104(1):200–6.
17. de Ziegler D, Borghese B, Chapron C. Endometriosis and infertility: pathophysiology and management. Lancet (London, England) 2010;376(9742):730–8.
18. Barnhart K, Dunsmoor-Su R, Coutifaris C. Effect of endometriosis on in vitro fertilization. Fertil Steril 2002;77(6):1148–55.
19. Simón C, Gutiérrez A, Vidal A, de los Santos MJ, Tarín JJ, Remohí J, et al. Outcome of patients with endometriosis in assisted reproduction: results from in-vitro fertilization and oocyte donation. Hum Reprod 1994;9(4):725–9.
20. Díaz I, Navarro J, Blasco L, Simón C, Pellicer A, Remohí J. Impact of stage III-IV endometriosis on recipients of sibling oocytes: matched case-control study. Fertil Steril 2000;74(1):31–4.
21. Pertwee RG. Emerging strategies for exploiting cannabinoid receptor agonists as medicines. Br J Pharmacol 2009;156(3):397–411.
22. Borini A, Sciajno R, Bianchi V, Sereni E, Flamigni C, Coticchio G. Clinical outcome of oocyte cryopreservation after slow cooling with a protocol utilizing a high sucrose concentration. Hum Reprod 2005;21(2):512–7.
23. Bustin SA, Benes V, Garson JA, Hellemans J, Huggett J, Kubista M, et al. The MIQE Guidelines: Minimum Information for Publication of Quantitative Real-Time PCR Experiments. Clin Chem 2009;55(4):611–22.

24. Pfaffl MW. A new mathematical model for relative quantification in real-time RT-PCR. Nucleic Acids Res 2001;29(9):45e–45.
25. Vandesompele J, De Preter K, Pattyn F, Poppe B, Van Roy N, De Paepe A, et al. Accurate normalization of real-time quantitative RT-PCR data by geometric averaging of multiple internal control genes. Genome Biol 2002;3(7):research0034.1-0034.11.
26. Tanghe S, Van Soom A, Nauwynck H, Coryn M, De Kruif A. Minireview: Functions of the cumulus oophorus during oocyte maturation, ovulation, and fertilization. Mol Reprod Dev 2002;61(3):414–24.
27. Assou S, Anahory T, Pantesco V, Le Carrour T, Pellestor F, Klein B, et al. The human cumulus--oocyte complex gene-expression profile. Hum Reprod 2006;21(7):1705–19.
28. Assou S, Haouzi D, Mahmoud K, Aouacheria A, Guillemin Y, Pantesco V, et al. A non-invasive test for assessing embryo potential by gene expression profiles of human cumulus cells: A proof of concept study. Mol Hum Reprod 2008;14(12):711–9.
29. Assou S, Haouzi D, De Vos J, Hamamah S. Human cumulus cells as biomarkers for embryo and pregnancy outcomes. Mol Hum Reprod 2010;16(8):531–8.
30. Gasca S, Pellestor F, Assou S, Loup V, Anahory T, Dechaud H, et al. Identifying new human oocyte marker genes: a microarray approach. Reprod Biomed Online 2007;14(2):175–83.
31. Ouandaogo ZG, Haouzi D, Assou S, Dechaud H, Kadoch IJ, De Vos J, et al. Human Cumulus Cells Molecular Signature in Relation to Oocyte Nuclear Maturity Stage. PLoS One 2011;6(11):e27179.
32. Ouandaogo ZG, Frydman N, Hesters L, Assou S, Haouzi D, Dechaud H, et al. Differences in transcriptomic profiles of human cumulus cells isolated from oocytes at GV, MI and MII stages after in vivo and in vitro oocyte maturation. Hum Reprod 2012;27(8):2438–47.
33. Su Y-Q, Sugiura K, Eppig JJ. Mouse oocyte control of granulosa cell development and function: paracrine regulation of cumulus cell metabolism. Semin Reprod Med 2009;27(1):32–42.
34. Lessey B, Young S. Integrins and Other Cell Adhesion Molecules in Endometrium and Endometriosis. Semin Reprod Med 1997;15(3):291–9.

35. Toya M, Saito H, Ohta N, Saito T, Kaneko T, Hiroi M. Moderate and severe endometriosis is associated with alterations in the cell cycle of granulosa cells in patients undergoing in vitro fertilization and embryo transfer. Fertil Steril 2000;73(2):344–50.
36. Maccarrone M. Endocannabinoids: Friends and foes of reproduction. Prog Lipid Res 2009;48(6):344–54.
37. Chan H-W, McKirdy NC, Peiris HN, Rice GE, Mitchell MD. The role of endocannabinoids in pregnancy. Reproduction 2013;146(3):R101-9.
38. Cecconi S, Rossi G, Castellucci A, D'Andrea G, Maccarrone M. Endocannabinoid signaling in mammalian ovary. Eur J Obstet Gynecol 2014;178:6–11.
39. Peralta L, Agirregoitia E, Mendoza R, Expósito A, Casis L, Matorras R, et al. Expression and localization of cannabinoid receptors in human immature oocytes and unfertilized metaphase-II oocytes. Reprod Biomed Online 2011;23:372–9.
40. Howlett AC, Barth F, Bonner TI, Cabral G, Casellas P, Devane WA, et al. International Union of Pharmacology. XXVII. Classification of cannabinoid receptors. Pharmacol Rev 2002;54(2):161–202.
41. Starowicz K, Nigam S, Di Marzo V. Biochemistry and pharmacology of endovanilloids. Pharmacol Ther 2007;114(1):13–33.
42. Maccarrone M, Rossi S, Bari M, De Chiara V, Fezza F, Musella A, et al. Anandamide inhibits metabolism and physiological actions of 2-arachidonoylglycerol in the striatum. Nat Neurosci 2008;11(2):152–9.
43. Sukumaran P, Schaar A, Sun Y, Singh BB. Functional role of TRP channels in modulating ER stress and Autophagy. Cell Calcium 2016;60(2):123–32.
44. Brown I, Cascio MG, Rotondo D, Pertwee RG, Heys SD, Wahle KWJ. Cannabinoids and omega-3/6 endocannabinoids as cell death and anticancer modulators. Prog Lipid Res 2013;52(1):80–109.
45. Okamoto Y, Morishita J, Tsuboi K, Tonai T, Ueda N. Molecular characterization of a phospholipase D generating anandamide and its congeners. J Biol Chem 2004;279(7):5298–305.
46. McKinney MK, Cravatt BF. Structure and function of fatty acid amide hydrolase. Annu Rev Biochem 2005;74:411–32.

47. Bensinger SJ, Tontonoz P. Integration of metabolism and inflammation by lipid-activated nuclear receptors. Nature 2008;454(7203):470–7.
48. O'Sullivan SE. Cannabinoids go nuclear: evidence for activation of peroxisome proliferator-activated receptors. Br J Pharmacol 2009;152(5):576–82.
49. Froment P, Gizard F, Defever D, Staels B, Dupont J, Monget P. Peroxisome proliferator-activated receptors in reproductive tissues: from gametogenesis to parturition. J Endocrinol 2006;189(2):199–209.
50. Komar CM, Braissant O, Wahli W, Curry TE. Expression and localization of PPARs in the rat ovary during follicular development and the periovulatory period. Endocrinology 2001;142(11):4831–8.
51. Komar CM. Peroxisome proliferator-activated receptors (PPARs) and ovarian function--implications for regulating steroidogenesis, differentiation, and tissue remodeling. Reprod Biol Endocrinol 2005;3:41.
52. Komar CM, Curry TE. Localization and expression of messenger RNAs for the peroxisome proliferator-activated receptors in ovarian tissue from naturally cycling and pseudopregnant rats. J Control Release 2002;66(5):1531–9.
53. Sutton-Mcdowall ML, Gilchrist RB, Thompson JG. The pivotal role of glucose metabolism in determining oocyte developmental competence. Reproduction 2010;139(4):685–95.
54. Joost H-G, Bell GI, Best JD, Birnbaum MJ, Charron MJ, Chen YT, et al. Nomenclature of the GLUT/SLC2A family of sugar/polyol transport facilitators. Am J Physiol Endocrinol Metab 2002;282(4):E974-6.

Chapter 6

Could unilateral endometriosis affect the contralateral ovary? New insights from a multidisciplinary study

Notarstefano et al.

(manuscript in preparation)

Introduction

Endometriosis is a chronic gynaecological disease characterised by the presence of epithelial, glandular and stromal endometrial cells in extra-uterine regions (1). It is reported that 30% to 50% of women with a diagnosis of endometriosis are also affected by infertility (2). Several factors have been suggested as possible causes of endometriosis-associated infertility: pelvic adhesions, luteinized unruptured follicles, immunologic alterations, progesterone resistance, and impairment of folliculogenesis, ovulation, ovum transport, fertilization, and implantation (3,4). The characteristics of this infertility are variable, and women affected by endometriosis can display a decrease of fertilization, implantation and pregnancy rates (5). Actually, several studies report that the factor that impacts the most on the subfertility/infertility of women affected by endometriosis is the poor oocyte quality (6). Xu and colleagues studied oocytes from patients with minimal or mild endometriosis, finding a significant decrease in quality of these oocytes, which showed alteration in mitochondria quality and quantity (7). As the impaired follicle development appears to be one of the crucial factors in endometriosis, many studies have focused on cumulus cells (CCs) and granulosa cells (GCs). GCs are responsible of many important follicular functions, such as the production of estradiol during follicular growth, the production of essential nutrients used as an energy source during oocyte maturation, the accumulation of oocyte secreted metabolites, and the secretion of progesterone after ovulation (8–11). A dysregulation in these functions can lead to severe cellular damages: for example, an excessive amount of lipids in GCs determines endoplasmic reticulum stress, mitochondrial dysfunction and

apoptosis, causing decreased rates of oocyte nuclear maturation and fertilization (12,13).

The analysis of GCs collected from patients with diagnosis of endometriosis revealed an altered cell cycle in these follicular cells, which could impair folliculogenesis (4). There is evidence that oocyte quality and follicular development are closely related to GCs apoptosis and autophagy (14–17). Nakahara and colleagues described a higher incidence of apoptotic bodies in GCs collected from patients with endometriosis (18); endometriosis is also reported to result in an increase in GCs apoptosis, proportionate to the severity of the disease, resulting in poor oocyte quality (19).

Fourier Transform InfraRed Microspectroscopy (FTIRM) and Raman MicroSpectroscopy (RMS) are powerful vibrational techniques, broadly applied in life sciences for the study of the biomolecular building and composition of cells (20–22). The analysis of FTIRM and RMS spectral bands in terms of position, intensity and width, makes it possible to obtain a unique molecular fingerprint of the most relevant biological molecules (proteins, lipids, sugars and nucleic acids) (23–25). This chemical and morphological information can be directly related to pathogenesis, cellular activity, metabolism and oxidative stress status (26–29). Several studies have applied both FTIRM and RMS to evaluate a wide range of cells, such as tumoral cells (30–32), human oocytes (33), human GCs (Gioacchini et al., 2017, submitted to Cell Reports).

In this light, via a multidisciplinary approach consisting in coupling vibrational microspectroscopies (FTIRM and RMS) and qPCR analysis, we studied several aspects of luteinized human GCs collected from both the ovaries of patients with diagnosis of unilateral ovarian endometriosis. The aim was to investigate how this disease affects GCs biochemical composition, metabolism, and cell death, not only in the ovary affected by endometriotic lesions, but also in the contralateral "healthy" one.

Experimental section

The study was carried out on human GCs at Tecnobios Procreazione, in full accordance with the Declaration of Helsinki (World Med. Ass. 2013). To participate in this investigation, each patient signed a written consent, which included the donation of GCs. All samples were anonymous and marked by a code and hence it was impossible to correlate them to a physical person.

Luteinized GCs sample collection

20 patients enrolled in an in vitro fertilization program, were recruited according to the following inclusion criteria: regular ovulatory menstrual cycles; FSH $<$ 10 IU/I on day 3 of the menstrual cycle; non-smokers; 35$\pm$2.8 of age. Controlled ovarian stimulation was induced using leuprorelin (Enantone, Takeda, Rome, Italy) and rFSH (Gonal-F, Serono, Rome, Italy, or Puregon Organon, Rome, Italy). HCG at 10,000 IU (Gonasi, Amsa, Rome, Italy) was administered when one or more follicles reached a diameter of ca. 23 mm (34).

GCs samples were divided as follow: GCs from 10 women with diagnosis of tubal, idiopathic or male infertility representative of the control group (**CTRL**); GCs from endometriosis-affected ovary (Endometriosis, **ENDO**) and GCs from the contralateral "healthy" ovary (Contralateral, **CONTRAL**) retrieved on the remaining 10 women with a diagnosis of unilateral ovarian endometriosis.

At the end of the treatment, from each patient, a pool of luteinized GCs was collected from all the follicles, according to the following protocol. The follicular fluid was centrifuged at 1100x g for 10 min and the pellet was resuspended in 2 mL of gamete medium, overlaid on 1 mL pure sperm 50% (obtained by pure sperm 80 and gamete buffer medium) and centrifuged again at 1600x g for 13 min to separate GCs from the red blood cells. After centrifugation, GCs were recovered, placed in 1mL of NaCl 0.9% solution and then centrifuged at 300x g for 10 minutes. The supernatant was discarded, and the pellet was resuspended in 1mL of NaCl 0.9% solution and centrifuged again at 300x g for 10 minutes. An aliquot of each GCs sample was immediately frozen in liquid nitrogen and stored at -80°C till qPCR analysis. The remaining aliquots of GCs samples were deposited without any fixation process onto CaF_2 optical windows (1-mm thick) and air-dried for 30 min for FTIRM analysis. GCs were fixed in a 4% PFA solution for 10 min, twice washed in physiological solution, and then stored at 4°C until RMS measurement. Previous experiments carried out in our laboratories evidenced that samples prepared as above, showed a good stability in time, providing homogeneous and reliable data sets.

FTIRM measurements and data analysis

FTIRM measurements were carried out at the infrared beamline SISSI (Synchrotron Infrared Source for Spectroscopic and Imaging), Elettra Sincrotrone Trieste (Trieste, Italy). A Hyperion 3000 Vis-IR microscope coupled with a Bruker VERTEX 70 interferometer (OPUS 7.1 software package, Bruker Optics, Ettlingen, Germany) was used. The spectrometer was equipped with a HgCdTe (MCT_A) detector operating at liquid nitrogen temperature, which covers the entire IR spectral range from 4000 to 700 cm^{-1}.

On each sample, ~30 areas were selected by visible microscopy on which IR spectra were collected in transmission mode (spatial resolution 30x30 μm^2, spectral resolution 4 cm^{-1}, zero-filling factor of 2 in the spectral range 4000−800 cm^{-1}, scanner velocity 40 kHz, 256 scans). Microscope knife-edge apertures were set at 30×30 μm^2, using a 15X Schwarzschild condenser and objective (NA = 0.4). Background spectra were collected using the same parameters on clean zones of the CaF_2 optical window. All the collected spectra were corrected for the contribution of atmospheric carbon dioxide and water vapour with the compensation routine of OPUS 7.0 software (Bruker Optics GmbH). Spectra having at 1660 cm^{-1} a peak height lower than 0.07 a.u. were discharged. The remaining IR spectra were first vector normalized and then submitted to multivariate analysis. PCA (Principal Components Analysis) was carried out by using an in-house developed algorithm with R Studio (RStudio: Integrated Development for R. RStudio, Inc., Boston, MA).

IR spectra were also integrated under the spectral regions reported in Table 1, by using OPUS 7.1 software.

Spectral Interval (cm^{-1})	Vibrational attribution	Cellular features	Ref.
3000–2836	Symmetric and asymmetric $CH_{2/3}$ stretching modes, **Lipids**	Saturated alkyl chains of cellular lipids (mainly) and proteins	(23)
1723-1481	C=O stretching, C-N stretching and N-H deformation in peptide linkage, **Proteins**	Cellular proteins	(35)
1286-1191	Asymmetric stretching modes of phosphate groups, **PhI**	Phosphate moieties of nucleic acids, phospholipids and phosphorylated proteins	(36,37)
1140-1030	Symmetric stretching modes of phosphate groups, and symmetric stretching of C-O groups in carbohydrates, **PhII-GLYCO**	Phosphate moieties, and carbohydrates	(33,37)
3000–2836 & 1775–950	Sum of all the vibrations indicated above, **Cell**	Overall cellular biomolecular content	

Table 1. List of the spectral intervals on which the area integrals were calculated, together with the vibrational attribution, the assigned name (bold characters) and the corresponding cellular features.

Integrated areas were used to calculate the band area ratios reported in Table 2.

Banda area ratios	Biological significance
LIPIDS/CELL	Total cellular lipids
PROTEINS/CELL	Total cellular proteins
PhI/CELL	Total cellular phosphate groups
PhII/CELL	Total cellular phosphate and carbophydrate groups

Table 2. Band area ratios of the integrals defined in Table 1 and their biological significance.

The convoluted 3050–2800 cm^{-1}, 1723–1481 cm^{-1} and 1350-900 cm^{-1} spectral regions were analysed by Peak Fitting procedure: absorbance average spectra of all samples were interpolated in the aforementioned regions, two-point baseline corrected and fitted with a Gaussian algorithm (GRAMS/AI 7.02, Galactic Industries, Inc., Salem, NH) (Table 3). To identify the underlying component bands, the number of peaks together with their centre values were precisely identified according to second derivative results. Mean values of area and wavelength were obtained for each component peak.

Spectral region	Wavenumber (cm^{-1})	Assignment	Label		
3050 – 2800 cm^{-1}	3012	=CH stretching vibration	CH	LIPIDS	
	2957	CH_3 asymmetric stretching vibrations	CH3		
	2869	CH_3 symmetric stretching vibrations			
	2925	CH_2 asymmetric stretching vibrations	CH2		
	2852	CH_2 symmetric stretching vibrations			
1790 – 1480 cm^{-1}	1746	C=O ester moieties stretching vibrations	C=O ESTERS		
	1694	β-turn structures vibrational modes	BETA	FOLDED	AI
	1680, 1627, 1613	β-sheet structures vibrational modes			
	1659	α-helix structures vibrational modes	HELIX		
	1640	Random coil structures vibrational modes	RANDOM		
1350– 900 cm^{-1}	1118	C-OH groups of ribose stretching vibrations	RNA	RNA	TOT
	994	C-O ribose vibration	RNA		
	911	C-C ring vibrations of ribose	RNA		
	1087	PO_2^- symmetric stretching mode of phosphates	PhII		
	1053	C-O stretching and bending mode of carbohydrates	GLYCO		
	924	Left-handed helix DNA vibrations	Z-DNA		

Table 3. Fit of the 3050-2800 cm^{-1}, 1790-1480 cm^{-1} and 1350-900 cm^{-1} spectral regions. The results of the fit are reported as position and area integral the selected underlying bands.

RMS measurements and data analysis

A Horiba Jobin-Yvon LabRAM HR800 spectrometer, equipped with a 532-nm diode laser as source was used. All measurements were acquired by using a x100 objective (Olympus, N.A. 1). The spectrometer was calibrated to the 520.7 cm^{-1} line of silicon prior to spectral acquisition. A 600 lines per mm grating was chosen. A 100 μm confocal pinhole was used for all measurements. The spectra were dispersed onto a 16-bit dynamic range Peltier cooled CCD detector. Point spectra from 50 cells seeded on the glass slide were acquired

for experimental group. The spectral range from 400 to 1800 cm^{-1}, the so-called fingerprint region, was chosen and spectra were acquired for 3x10 seconds at each spot.

RMS spectra were smoothed using 7 smoothing points and baseline-corrected with the polynomial method (2 iterations) (OPUS 7.1 software), and then submitted to multivariate analysis. PCA (Principal Components Analysis) was carried out by using an in-house developed algorithm with R Studio (RStudio: Integrated Development for R. RStudio, Inc., Boston, MA). Spectra were integrated under the bands highlighted as different by the loadings of the PCA (Table 4) (38).

Wavenumber (cm^{-1})	Assignment	Label
1657 / 1659	Amidic C=O stretching mode	PROTEINS
1615	Tyrosine and tryptophan C=C stretching mode	TYR-TRP
1605	Phenylalanine and tyrosine C=C stretching mode	PHE-TYR
1450	CH_2 bending mode	1450
1263	Amidic C-N stretching and N-H bending, mainly due to helix structures	HELIX
1003 / 1005	Phenylalanine symmetric stretching breathing mode	PHE
980	C-C stretching of beta-sheets structures	BETA
852 / 857	Amino acid sidechain C-C stretching of proline	PRO

Table 4. Peak position, assignments and label used of main Raman vibrational modes.

All the intensity values of the bands of interest were divided by the integrated area of the CH2 band, centred at ~1450 cm^{-1}, whose value did not change between the experimental groups.

RNA extraction and cDNA synthesis

Total RNA extraction from GCs was performed using Minikit RNAeasy® (Qiagen) extraction kits, following the manufacturer's protocol. Total RNA extracts were eluted in 20 μL of RNAse-free water. Final RNA concentrations were determined with a NanoDrop™ 1000 Spectrophotometer (Thermo Scientific) and RNA integrity was verified by Gel Red (Biotium, UK) staining of 28S and 18S ribosomal RNA fragments on 1% agarose gel. RNA was stored at -80°C until use. Total RNA was treated with DNAse (10 IU at 37°C for 10 min, MBI Fermentas); a total amount of 2 μg of RNA was used for cDNA synthesis, employing the SuperScript-II cDNA Synthesis Kit (Invitrogen, Life Technologies).

Real-time polymerase chain reaction

Relative quantification of gene expression was performed with the SYBR Green method in a CFX96 Real-Time PCR system (Bio-Rad). Duplicate PCRs were carried out for each sample analysed. Reactions were set mixing 1 μL diluted (1/10) cDNA, 5 μL of 2× SYBR Green PCR Master Mix (Bio-Rad), containing SYBR Green as a fluorescent intercalating agent, 0.1 μM of forward and reverse primers, and 3.8 μL of milliQ water.

The thermal profile was as follows: enzyme activation at 95°C for 3 min; 45 cycles of denaturation (10 sec at 95°C), followed by 20 sec annealing at 60°C for all the investigated genes, and 20 sec elongation at 72°C. Fluorescence was monitored at the end of each cycle. Dissociation curves for primer specificity and absence of primer-dimer formation check were performed and

consistently showed a single peak. Glyceraldehyde-3-phosphate dehydrogenase (*gapdh*) and ribosomal protein L13a (*rpl13a*) were used as internal controls to enable result standardization by eliminating variations in mRNA and cDNA quantity and quality (39). These genes were chosen because their mRNA levels did not vary between experimental groups. No amplification products were observed in negative controls and no primer–dimer formations were observed in the control templates. Data were analysed using CFX Manager Software version 3.1 (Bio-Rad). The quantification method was based on a ΔΔCt calculation implemented with the Pfaffl equation, to improve accuracy by accounting for varied reaction efficiencies depending on primers (40,41). Modification of gene expression is represented with respect to zero. Primer sequences used are reported in Table 5.

Gene	Forward primer (5' – 3')	Reverse primer (5' – 3')	Acc number	Gene ID
gapdh	GTGAAGGTCGGAGTCAACG	GGTGAAGACGGCCAGTGGACTC	NM_002046.5	2597
rpl13a	TCTGGAGGACTGTAAGAGGTATGC	AGACGCACAATCTTGAGAGCAG	NM_012423.3	23521
pparα	CTGGAAGCTTTGGCTTTACG	GTTGTGTGACATCCCGACAG	NM_001001928.2	5465
pparγ	TTCAGAAATGCCTTGCAGTG	CACCTCTTTGCTCTGCTCCT	NM_001330615.1	5468
fasn	CAGAGCAGCCATGGAGGAG	TAGAGCCCCGCCTTCCAG	NM_004104.4	2194
glut1	TGGCATCAACGCTGTCTTCT	AGCCAATGGTGGCATACACA	NM_006516.2	6513
glut9	TCCAGAGGGGCATGAAAACTC	CGAGCAGGACCAGTCCAATTT	NM_001001290.1	56606
dnmt1	CTACCAGGAGAAGGACAGG	CTCACAGACGCCACATCG	NM_001130823.2	1786
dnmt3a	TATGAACAGGCCGTTGGCATC	AAGAGGTGGCGGATGACTGG	NM_001320892.1	1788
birc5	AGGACCACCGCATCTCTACAT	AAGTCTGGCTCGTTCTCAGTG	NM_001012271.1	332
casp3	CTCTGGTTTTCGGTGGGTGT	CGCTTCCATGTATGATCTTTGGTT	NM_001354778.1	836
becn1	GGCTGAGAGACTGGATCAGG	CTGCGTCTGGGCATAACG	NM_003766.4	8678
lc3a	GAGAAGCAGCTTCCTGTTCTGG	GTGTCCGTTCACCAACAGGAAG	NM_032514.3	84557

Table 5. List of primers used in gene expression analyses by Real-Time qPCR. *gapdh*: glyceraldehyde-3-phosphate dehydrogenase; *rpl13a*: ribosomal protein L13a; *pparα*:

peroxisome proliferator activated receptor alpha; *pparγ*: peroxisome proliferator activated receptor gamma; *fasn*: fatty acid synthase; *glut1*: glucose transporter 1 (*slc2a1*: solute carrier family 2 member 1); *glut9*: glucose transporter 9 (*slc2a9*: solute carrier family 2 member 9); *dnmt1*: DNA methyltransferase 1; *dnmt3a*: DNA methyltransferase 3 alpha; *survivin* (*birc5*: baculoviral IAP repeat containing 5); *casp3* (caspase 3); *becn1* (beclin 1); *lc3a* (*map1lc3a*: microtubule associated protein 1 light chain 3 alpha).

Statistical analysis

Normally distributed data deriving from integration of FTIRM and RMS spectra, from Peak Fitting of FTIRM spectra, and from gene expression analysis were presented as mean ± S.D. Significant differences between experimental groups were determined by means of a factorial analysis of variance (one-way ANOVA), followed by Tukey's multiple comparisons test, using the statistical software package Prism6 (Graphpad Software, Inc. USA). Statistical significance was set at $p < 0.05$. Asterisks denote significant differences from the control group (* = $p < 0.05$; ** = $p < 0.01$; *** = $p < 0.001$; **** = $p < 0.0001$).

Results

Human luteinized GCs samples divided into three experimental groups named **CTRL** (diagnosis of tubal, idiopathic or male infertility), **ENDO** (diagnosis of unilateral ovarian endometriosis, GCs collected from the endometriosis-affected ovary), and **CONTRAL** (diagnosis of unilateral ovarian endometriosis, GCs collected from the contralateral “healthy” ovary) were analysed using FTIRM and RMS, and by qPCR assays.

FTIRM measurements and data analysis

PCA was carried out to analyse and compare the spectral profiles of the three experimental groups. Figure 1A shows the PCA scatter plot of GCs spectra from all the three experimental groups. A clear segregation of **CTRL** and **ENDO/CONTRAL** spectra was observed along PC1 axis (73.91 % of the system variance), and the analysis of PC1 loading (Figure 1B) showed the most visible discriminant features, which were also highlighted in the average absorbance spectra (Figure 1C).

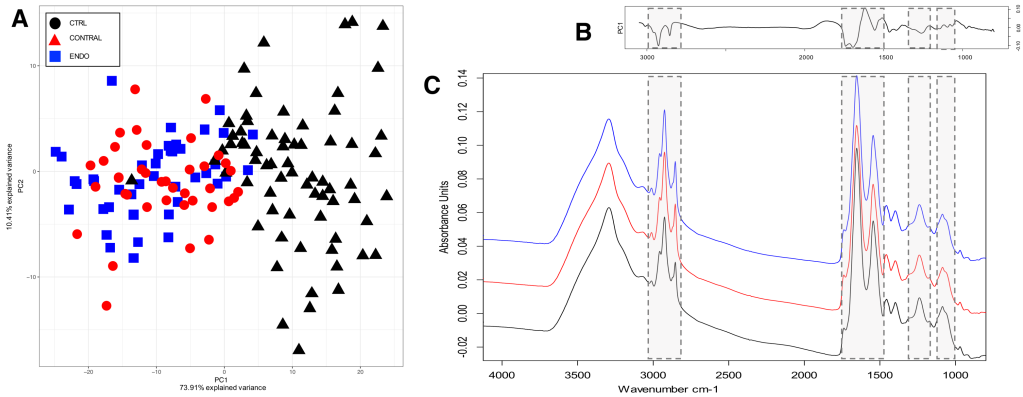

Figure 1. Principal Components Analysis on FTIRM spectra. PCA scatter plot of **CTRL**, **ENDO** and **CONTRAL** experimental groups (A); corresponding loading of PC1 (B); mean spectra of **CTRL** (black), **ENDO** (blue) and **CONTRAL** (red) experimental groups (C). Highlighted regions in (B) and (C) indicate discriminatory features.

To perform a semi-quantitative analysis of the macromolecular composition of **CTRL**, **CONTRAL** and **ENDO** GCs, specific band area

ratios were calculated using the area integrals described in the Experimental section (Figure 2).

The analysis of their numerical variation between the experimental groups led to the following considerations: (i) the total amount of cellular lipids (LIPIDS/CELL) showed a significant increase in **CONTRAL** and **ENDO** GCs with respect to **CTRL** ones (Figure 2A); (ii) the total amount of cellular proteins (PROTEINS/CELL) did not significantly change between the experimental groups (Figure 2B); (iii) the ratio PhI/CELL showed a significant increase in **CONTRAL** and **ENDO** GCs with respect to **CTRL** ones (Figure 2C); (iv) the ratio PhII-GLYCO/CELL did not change between the two experimental groups (Figure 2D).

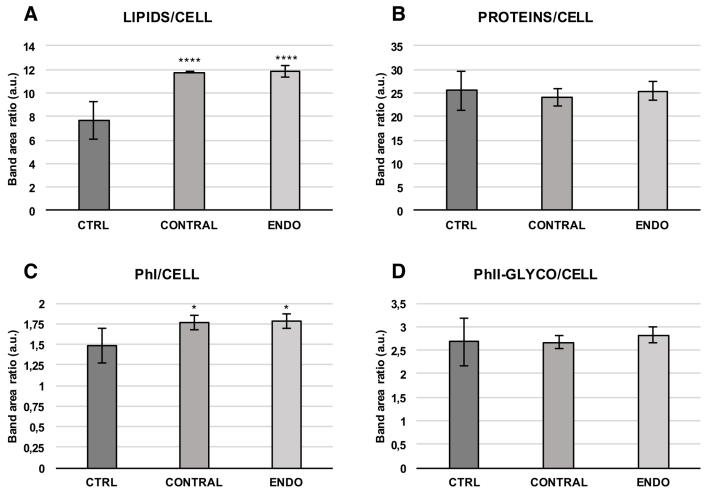

Figure 2. Numerical variations of the following band area ratios for the **CTRL**, **CONTRAL** and **ENDO** experimental groups: LIPIDS/CELL (spectral region 3050-2800

cm^{-1}) (A); PROTEINS/CELL (spectral region 1723-1481 cm^{-1}) (B); PhI/CELL (band at ~1240 cm^{-1}) (C); PhII-GLYCO/CELL (band at ~1080 cm^{-1}) (D). Values are reported as mean±SD. Significant differences were determined as described in the Experimental section (see Statistical analysis). Asterisks above columns indicate statistical differences with respect to **CTRL** (* = $p<0.05$; **** = $p<0.0001$).

For a deeper analysis of the spectral profile of lipids and proteins in **CTRL**, **CONTRAL** and **ENDO** GCs, a fit of the 3050–2800 cm^{-1}, 1790–1480 cm^{-1} and 1350-900 cm^{-1} spectral regions was performed, and the position and the area integral of all the underlying bands were obtained. The statistical analysis of the numerical variations of specific band area ratios (Figure 3), calculated using the area integrals in Table 2, led to the following results: (i) the ratio CH/LIPIDS significantly increased in both **CONTRAL** and **ENDO** GCs (Figure 3A); (ii) the ratio C=O ESTERS/AI significantly increased in both **CONTRAL** and **ENDO** GCs (Figure 3B); (iii) the ratio FOLDED/AI significantly decreased in both **CONTRAL** and **ENDO** GCs with respect to **CTRL** ones (Figure 3C); (iv) the value RANDOM/AI significantly increased in both **CONTRAL** and **ENDO** GCs, consistent with the opposite trend observed in the FOLDED/AI ratio (Figure 3D); (v) the ratio GLYCO/TOT significantly decreased in **CONTRAL** and **ENDO** GCs, with respect to **CTRL** ones (Figure 3E); (vi) the value RNA/PhII significantly decreased in **CONTRAL** and **ENDO** GCs (Figure 3F); (vii) the ratio Z-DNA/PhII significantly increased in both **CONTRAL** and **ENDO** GCs (Figure 3G).

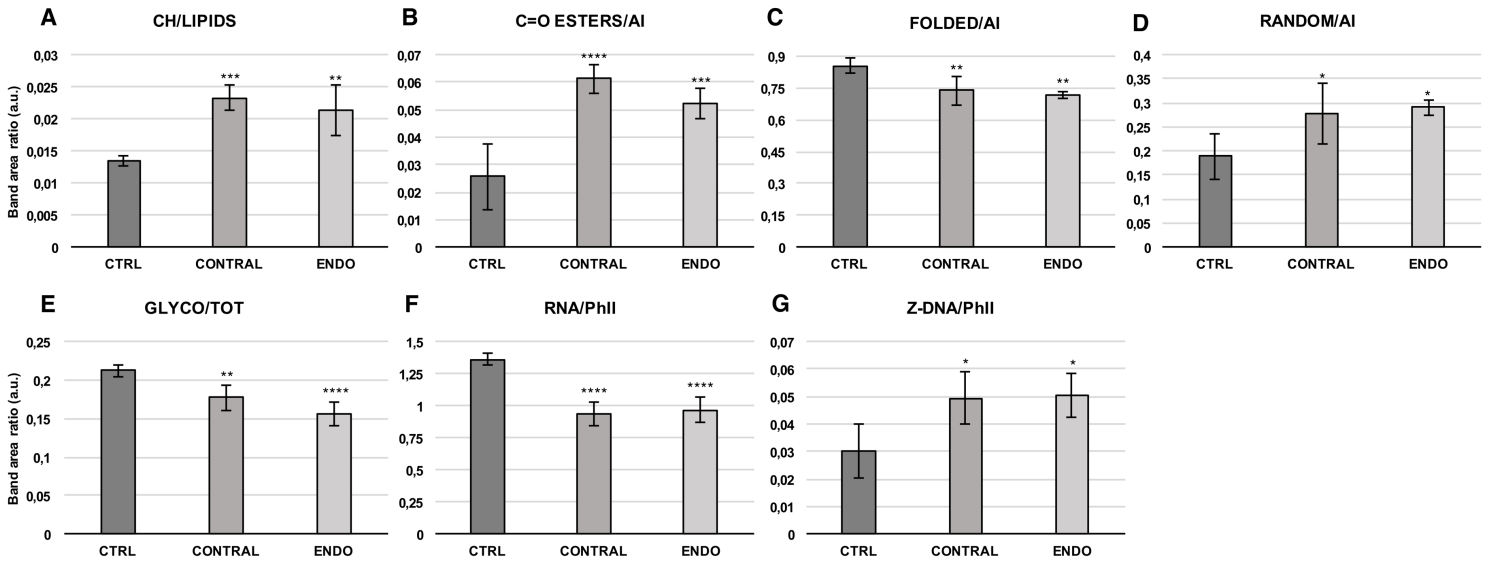
A
CH/LIPIDS
Band area ratio (a.u.)
0,03
0,025
0,02
0,015
0,01
0,005
0
***
**
CTRL
CONTRAL
ENDO
B
C=O ESTERS/AI
0,07
0,06
0,05
0,04
0,03
0,02
0,01
0
****
***
CTRL
CONTRAL
ENDO
C
FOLDED/AI
0,9
0,75
0,6
0,45
0,3
0,15
0
**
**
CTRL
CONTRAL
ENDO
D
RANDOM/AI
0,4
0,35
0,3
0,25
0,2
0,15
0,1
0,05
0
*
*
CTRL
CONTRAL
ENDO
E
GLYCO/TOT
Band area ratio (a.u.)
0,25
0,2
0,15
0,1
0,05
0
**
****
CTRL
CONTRAL
ENDO
F
RNA/PhII
1,5
1,25
1
0,75
0,5
0,25
0
****
****
CTRL
CONTRAL
ENDO
G
Z-DNA/PhII
0,07
0,06
0,05
0,04
0,03
0,02
0,01
0
*
*
CTRL
CONTRAL
ENDO

Figure 3. Numerical variations of the following band area ratios for the **CTRL**, **CONTRAL** and **ENDO** experimental groups: 3010 cm^{-1} (CH) / peaks in the 3050-280 cm^{-1} range (LIPIDS) (A); 1746 cm^{-1} (C=O esters) / bands in the 1695-1625 cm^{-1} interval (AI) (B); 1659 + 1669 + 1694 + 1680 + 1627 + 1613 cm^{-1} (FOLDED) / AI (C); 1640 cm^{-1} (RANDOM) / AI (D); 1053 cm^{-1} (GLYCO) / peaks in the 1350-900 cm-1 region (TOT) (E); 1118 + 994 + 911 cm^{-1} (RNA) / 1087 cm^{-1} (PhII) (F); 924 cm^{-1} (Z-DNA) / (PhII) (G). Asterisks above columns indicate statistical differences with respect to **CTRL** (* = $p<0.05$; ** = $p<0.01$; *** = $p<0.001$; **** = $p<0.0001$; Student's t test).

RMS measurements and data analysis

Raman spectra acquired in the fingerprint region (400–1800 cm^{-1}) were first submitted to multivariate analysis (PCA), which was carried out to highlight the spectral profiles of **CTRL**, **CONTRAL** and **ENDO** GCs. Figure 4A shows the PCA scatter plot of GCs spectra from the three experimental groups. A clear segregation of **CTRL** and **ENDO/CONTRAL** spectra was observed along PC1 axis (60.39 % of the system variance), and the analysis of PC1 loading (Figure 4B) showed the most visible discriminant features, which were also highlighted in absorbance spectra (Figure 4C).

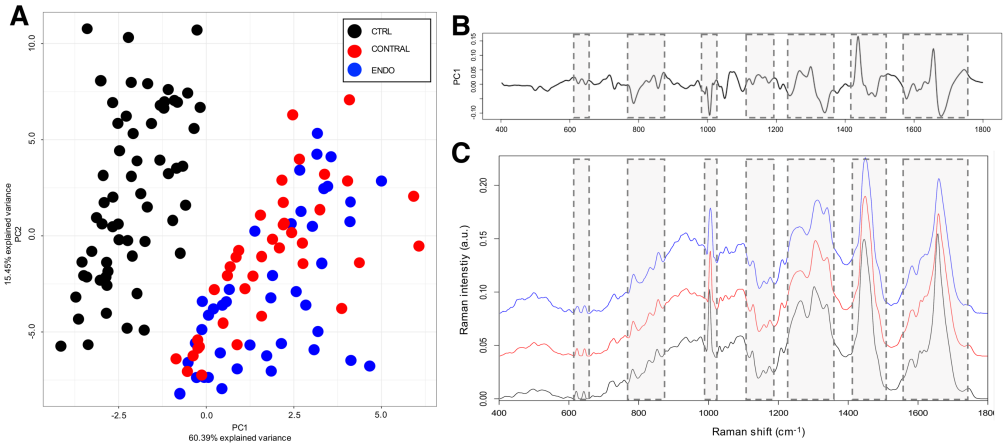

Figure 4. Principal Components Analysis on RMS spectra. PCA scatter plot of **CTRL**, **ENDO** and **CONTRAL** experimental groups (A); corresponding loading of PC1 (B); mean spectra of **CTRL** (black), **ENDO** (blue) and **CONTRAL** (red) experimental groups (C). Highlighted regions in (B) and (C) indicate discriminatory features.

Raman spectra of the three experimental groups were evaluated in terms of position of the bands: red shifts were observed affecting: (i) the band PROTEINS, centred at 1657 cm^{-1} in **CTRL** and at 1659 cm^{-1} in **CONTRAL/ENDO**; (ii) the band PHE, from 1003 cm^{-1} of **CTRL** to 1005 cm^{-1} of **CONTRAL/ENDO**; (iii) the band PRO, centred at 852 cm^{-1} in **CTRL** and at 857 cm^{-1} in **CONTRAL/ENDO**.

The analysis of the numerical variations of specific band area ratios, particularly related to proteins and protein characteristics, led to the following results (Figure 5): (i) the ratio PROTEINS/1450 showed a slight but not significant decrease in **CONTRAL** and **ENDO** GCs with respect to **CTRL**

ones (Figure 5A); (ii) the value TYR-TRP/1450 showed a significant decrease in both the experimental groups linked to endometriosis (Figure 5B); (iii) the ratio PHE-TYR/1450 significantly decreased in **CONTRAL** and **ENDO** GCs (Figure 5C); (iv) the value HELIX/1450 showed a significant decrease in **CONTRAL** and **ENDO** GCs with respect to CTRL ones (Figure 5D); (v) the value PHE/1450 significantly decreased in **CONTRAL** and **ENDO** experimental groups (Figure 5E); (vi) the value BETA/showed a significant decrease in **CONTRAL** and **ENDO** GCs with respect to **CTRL** ones (Figure 5F); (vii) the ratio PRO/1450 significantly increased in **CONTRAL** and **ENDO** GCs (Figure 5G). All the other bands highlighted as different by the PC1 loading were investigated, but did not show significant alterations between the experimental groups (data not shown).

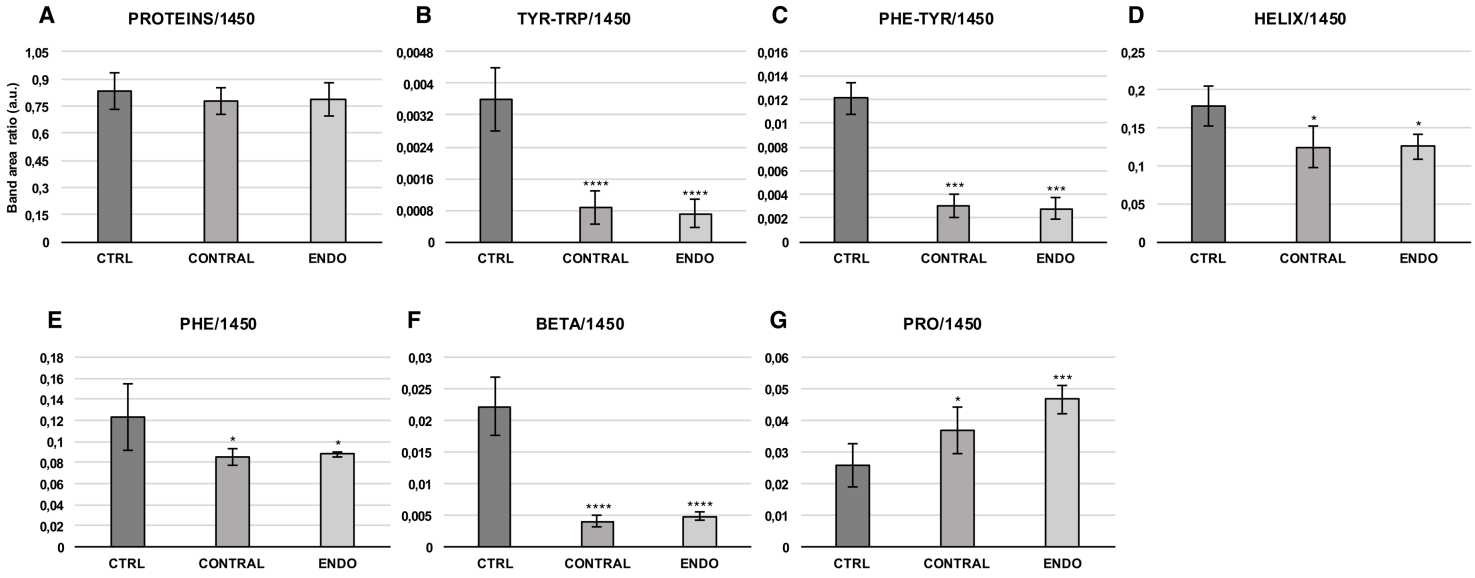
A
PROTEINS/1450
Band area ratio (a.u.)
1,05
0,9
0,75
0,6
0,45
0,3
0,15
0
CTRL
CONTRAL
ENDO
B
TYR-TRP/1450
0,0048
0,004
0,0032
0,0024
0,0016
0,0008
0
****
****
CTRL
CONTRAL
ENDO
C
PHE-TYR/1450
0,016
0,014
0,012
0,01
0,008
0,006
0,004
0,002
0
***
***
CTRL
CONTRAL
ENDO
D
HELIX/1450
0,25
0,2
0,15
0,1
0,05
0
*
*
CTRL
CONTRAL
ENDO
E
PHE/1450
0,18
0,16
0,14
0,12
0,1
0,08
0,06
0,04
0,02
0
*
*
CTRL
CONTRAL
ENDO
F
BETA/1450
0,03
0,025
0,02
0,015
0,01
0,005
0
****
****
CTRL
CONTRAL
ENDO
G
PRO/1450
0,06
0,05
0,04
0,03
0,02
0,01
0
*
***
CTRL
CONTRAL
ENDO

Figure 5. Numerical variations of the following band area ratios for the **CTRL**, **CONTRAL** and **ENDO** experimental groups: PROTEINS (1657 cm^{-1}) /1450 (A); TYR-TRP (1615 cm^{-1}) /1450 (B); PHE-TYR (1605 cm^{-1}) /1450 (C); HELIX (1260 cm^{-1}) /1450 (D); PHE (1003 cm^{-1}) /1450 (E); BETA (980 cm^{-1}) /1450 (F); PRO (855 cm^{-1}) /1450 (G). Values are reported as mean±SD. Significant differences were determined as described in the Experimental section (see Statistical analysis). Asterisks above columns indicate statistical differences with respect to **CTRL** (* = $p<0.05$; ** = $p<0.01$; *** = $p<0.001$; **** = $p<0.0001$).

Gene expression analysis

Table 2 shows the numerical variations in the expression of the genes of interest. A significant alteration in the expression was observed for all the genes investigated in GCs from patients affected by endometriosis, collected from both the ovaries. In relation to lipid metabolism, **CONTRAL** and **ENDO** GCs showed a significant increase in both *ppar*α and *ppar*γ expression ($p < 0.01$ and $p < 0.0001$, respectively), and in *fasn* expression ($p < 0.001$ and $p < 0.0001$, respectively). Carbohydrate metabolism is also affected by endometriosis, in both the ovaries, as proved by the increased expression of *glut1* ($p < 0.01$ and $p < 0.0001$, respectively for **CONTRAL** and **ENDO**) and *glut9* ($p < 0.0001$, for both **CONTRAL** and **ENDO**). We analysed the methylation process by studying the gene expression of *dnmt1*, a maintenance methyltransferase, and *dnmt3a*, a *de novo* methyltransferase: we found for both the genes a significant increase in GCs collected from both the ovaries of patients affected by endometriosis (*dnmt1*: $p < 0.01$ and $p < 0.0001$, respectively for **CONTRAL** and **ENDO**; *dnmt3a*: $p < 0.01$ and $p < 0.0001$, respectively for **CONTRAL** and **ENDO**). Finally, cell death/survival was

investigated, by studying the gene expression of anti-apoptotic (*birc5*), pro-apoptotic (*casp3*), and autophagy-related (*becn1*, *lc3a*) signals: we found a significant decrease of the expression of *birc5* ($p < 0.0001$, for **CONTRAL** and **ENDO**), a significant increase of *casp3* ($p < 0.001$ for **CONTRAL**, and $p < 0.0001$ for **ENDO**), a significant increase of *becn1* ($p < 0.05$ for **ENDO**), and a significant increase of *lc3a* ($p < 0.05$ for **CONTRAL**, and $p < 0.01$ for **ENDO**).

Gene	CTRL	CONTRAL	ENDO
pparα	1.43 ± 0.22	3.4 ± 0.88 **	4.7 ± 0.97 ****
pparγ	1.51 ± 0.13	3.3 ± 1.31 *	4.17 ± 0.83 **
fasn	1.32 ± 0.41	4.13 ± 0.12 ***	6.23 ± 1.29 ****
glut1	6.33 ± 0.78	2.19 ± 0.86 ****	1.13 ± 0.39 ****
glut9	9.08 ± 0.44	1.51 ± 0.8 ****	1.19 ± 0.47 ****
dnmt1	1.32 ± 0.42	3.17 ± 0.52 **	6.49 ± 0.97 ****
dnmt3a	1.68 ± 0.13	3.31 ± 0.61 **	7.71 ± 0.83 ****
birc5	27.54 ± 2.27	2.54 ± 0.56 ****	1.09 ± 0.15 ****
casp3	2.29 ± 1.13	54.47 ± 4.36 ***	63.30 ± 2.29 ****
becn1	1.20 ± 0.02	1.52 ± 0.01 ns	3.01 ± 0.21 *
lc3a	1.96 ± 0.01	3.41 ± 0.11 *	4.27 ± 0.59 **

Table 6. Transcription profiles of investigated genes. Significant differences were determined as described in the Experimental section (see Statistical analysis). Green indicates increased expression; red indicates decreased expression; yellow indicates no significant modification in expression. Asterisks indicate statistical differences with respect to **CTRL** (* = $p<0.05$; ** = $p<0.01$; *** = $p<0.001$; **** = $p<0.0001$; ns = not significant).

Discussion

Poor oocyte quality is clearly the factor that impacts the most on the subfertility/infertility of women affected by endometriosis (6). The key role played by GCs in follicles has made them a topic of interest in several studies (8,42,43). Given the importance of these cells, a dysregulation of their functions can lead to severe damage to the oocyte. In this study, we aimed to apply a multidisciplinary approach, consisting in coupling two vibrational microspectroscopies (FTIRM and RMS) with qPCR analysis, to investigate how ovarian endometriosis affects GCs biochemical composition, metabolism, and cell death, not only in the ovary affected by endometriotic lesions, but also in the contralateral "healthy" one. The multidisciplinary approach used in this study revealed several layers of impairment of GCs due to ovarian endometriosis, in both the ovaries. In particular, the macromolecular building blocks of GCs appears to be substantially altered, an oxidative stress mechanism seems to be activated, lipid and carbohydrate metabolisms are deregulated, cell death/survival regulative machineries are impaired, and an alteration in DNA methylation occurs.

Peak fitting performed on FTIRM spectra pointed to a significant increase of =CH groups (CH/LIPIDS ratio) and C=O ester moieties (C=O/ESTERS ratio): these two values, taken together when following the same trend, are attributed to a mechanism of lipid oxidation (44,45). Moreover, both FTIRM and RMS spectra highlighted no difference in the total protein amount, but a significant impairment in secondary structure proper folding (FTIRM: FOLDED/AI ratio increased, and RANDOM/AI ratio decreased; RMS:

HELIX/1450 and BETA/1450 ratios decreased). Both the results of lipid oxidation and alterations in protein secondary structures are consistent with a process of oxidative stress altering the cellular constituents. It is known that in addition to lipids, cellular oxidation targets proteins, leading to their modification and making them prone to misfolding, hence creating internal cell stressors, such as misfolded molecules (46). This oxidation picture is consistent with the known reduced antioxidant ability in infertile women with endometriosis (47) and the elucidated role played by oxidative stress and reactive oxygen species (ROS) in the progression of endometriosis (48,49). It is reported that both GCs and follicular fluid from endometriosis-affected patients display a higher 8-OHdG index, which permits the analysis of DNA oxidative damage (50,51): hence, the oxidative stress characteristic of endometriosis also affects the follicular microenvironment, potentially impacting ovarian folliculogenesis and oocyte quality.

In a previous work focused on the alterations on GCs endocannabinoid system (ECS) due to endometriosis, we reported the activation of the lipid metabolism, probably due to the upregulation of ECS through PPARγ, both with gene expression analysis and with FTIR imaging (Chapter 5, data not published). Consistent with these results, in the present research, we observed a significant increase in lipid content (LIPIDS/CELL ratio obtained by integration of IR spectra), both in **CONTRAL** and **ENDO** experimental groups with respect to **CTRL** ones. Moreover, a modulation of lipid metabolism was confirmed by the increased expression of *pparα*, *pparγ* and *fasn* genes. *Pparα* plays a key role in lipid and lipoprotein metabolism (52,53);

pparγ regulates adipocyte differentiation and fatty acids storage (54); *fasn* has the main function to catalyse the synthesis of long-chain saturated fatty acids (55,56). It is reported that an excessive amount of lipids in cumulus-oocyte complexes, due to high-fat diets or to the *in vitro* exposure to lipid-rich follicular fluids, results in increased oocyte lipid content, induction of endoplasmic reticulum stress, mitochondrial dysfunction, and increased incidence of apoptosis in ovarian cells (12,13).

Six transport systems of amino acids were found in oocytes throughout the growth and maturation phases (57). Moreover, gap junctions and paracrine interactions between the oocyte and cumulus cells seem to be crucial for the uptake of amino acids by the oocyte (58). In the present study, by applying RMS analysis, we observed an alteration in terms of content of some amino acids (an increase of proline, concomitant with a decrease of tyrosine, tryptophan and phenylalanine, both in **CONTRAL** and **ENDO** experimental groups). This decrease could be consistent with the above highlighted lipid oxidative stress, since aromatic amino acid side chains are among the most desired targets for ROS attack (59).

Both FTIRM and qPCR analysis showed a decrease in carbohydrate content (GLYCO/TOT ratio) and metabolism (*glut1* and *glut9*), respectively, in both **CONTRAL** and **ENDO** GCs. Glucose is fundamental for mammalian oocytes, but cannot be utilized unless previously transformed into pyruvate by GCs (60). Glucose is taken up by GCs via sodium-coupled glucose transporters (SGLTs) or through facilitative glucose transporters (GLUTs).

Fourteen paralogous members of the GLUT gene family are known, including GLUT1 and GLUT9 (61).

An interesting result we reported in this study is the increase of the Z-DNA fold form of DNA (Z-DNA/PhII ratio), evidenced by FTIRM analysis, in both **CONTRAL** and **ENDO** experimental groups, consistent with a significant decrease of RNA content (RNA/PhII ratio). Z-DNA is an elongated left-handed conformation of DNA, which can be found in segments with specialized sequences, characterized by alternations of purines and pyrimidines, especially alternating deoxycytidine and deoxyguanosine residues (62). Z-DNA spatial conformation is thought to be able to influence transcriptional activity by excluding transcription factors, normally binding the B-DNA form, from binding to target sequences (63). It is reported in literature that methylated $d(GC•GC)_n$ sequences facilitate B- to Z-DNA structural transitions. Furthermore, in the present study, an increase of *dnmt1* and *dnmt3a* expression was evidenced, consistent with the results obtained by FTIRM.

Finally, we investigated the expression of genes involved in the regulation of cell death and survival, in relation to endometriosis. It is known that apoptosis, carried out via several pathways, plays a crucial role in the adult ovary, and the molecules involved in these pathways regulate follicular survival, atresia, selection and loss, and luteogenesis (64). However, the control of this machinery can be impaired by many factors, such as endometriosis: in literature, a higher incidence of apoptotic bodies in GCs collected from patients with endometriosis is reported (18), and higher rates of apoptosis in GCs

obtained from endometriosis-affected patients (4). It is possible that this impairment is due to the decrease/loss of anti-apoptotic factors, such as survivin (*birc5*), as we observed in **CONTRAL** and **ENDO** GCs, and as reported by Fujino and colleagues, which described a lower gene expression level of survivin in patients with endometriosis (65). In addition, *survivin* inhibits the functionality of caspase-3 and caspase-7 terminal effectors: in particular, it is reported that the disruption of survivin-microtubule interactions determines the loss of survivin's anti-apoptotic function and, conversely, the increase of caspase-3 activity (66). *Casp3* encodes for one of the caspases, the so-called 'executioners of apoptosis' (67); with its activity of proteolytic cleavage of many key proteins, caspase-3 displays a crucial role in apoptosis. In this study, an increase in the expression of *casp3* was evidenced in **CONTRAL** and **ENDO** GCs. Also, autophagy seems to be implied in follicular development, since the accumulation of autophagosomes was detected in GCs and was found to induce apoptotic GCs death (16). The expression of *becn1*, which encodes for a protein regulating autophagy processes (68), increases in **ENDO** GCs. Concomitantly, we also found in **CONTRAL** and **ENDO** GCs an increase in the expression of *lc3a*, which encodes for the light chain 3 subunit of the neuronal microtubule-associated proteins (MAPs), associated to autophagosome membranes after processing (69). All together the obtained results describe a profound impairment caused by ovarian endometriosis in the mechanisms controlling cell death and survival, both affecting apoptosis and autophagy machineries.

In conclusion, the coupling of the two vibrational spectroscopies, FTIRM and RMS, and qPCR let obtain complementary information, which shed new light on the alteration induced by ovarian endometriosis on GCs metabolism, biochemical composition, and cell death/survival. Furthermore, it is important to emphasize a crucial aspect of the results we obtained: almost all the highlighted alterations affect both the ovary presenting endometriotic lesions, and the contralateral one, considered healthy. Although several studies reported that the number of retrieved oocytes is higher in the contralateral ovary with respect to the one with endometrioma (70,71), the results we report suggest a new scenario: endometriosis impairs the overall ovarian functions acting not only through a paracrine/autocrine signalling, but also through an endocrine one.

References

1. Benagiano G, Brosens I. REVIEW: The history of endometriosis: identifying the disease. Hum Reprod 1991;6(7):963–8.
2. Checa, MA; Gonzalez-Comadran, M; Agramunt, S; Carreras R. Fertility and Endometriosis. Clin Obstet Gynecol 2017;60(3):497–502.
3. Tanbo T, Fedorcsak P. Endometriosis-associated infertility: aspects of pathophysiological mechanisms and treatment options. Acta Obstet Gynecol Scand 2017;96(6):659–67.
4. Toya M, Saito H, Ohta N, Saito T, Kaneko T, Hiroi M. Moderate and severe endometriosis is associated with alterations in the cell cycle of granulosa cells in patients undergoing in vitro fertilization and embryo transfer. Fertil Steril 2000;73(2):344–50.
5. Kennedy S, Bergqvist A, Chapron C, D 'hooghe T, Dunselman G, Greb R, et al. ESHRE guideline for the diagnosis and treatment of endometriosis. Hum Reprod 2005;20(10):2698–704.
6. Sanchez AM, Vanni VS, Bartiromo L, Papaleo E, Zilberberg E, Candiani M, et al. Is the oocyte quality affected by endometriosis? A review of the literature. J Ovarian Res 2017;10(43).
7. Xu B, Guo N, Zhang X-M, Shi W, Tong X-H, Iqbal F, et al. Oocyte quality is decreased in women with minimal or mild endometriosis. Sci Rep 2015;5:10779.
8. Chronowska E. High-throughput analysis of ovarian granulosa cell transcriptome. Biomed Res Int 2014;2014.
9. Gilchrist RB, Ritter LJ, Armstrong DT. Oocyte-somatic cell interactions during follicle development in mammals. Anim Reprod Sci 2004;82–83:431–46.
10. Gilchrist RB, Lane M, Thompson JG. Oocyte-secreted factors: Regulators of cumulus cell function and oocyte quality. Hum Reprod Update 2008;14(2):159–77.
11. Downs SM, Mosey JL, Klinger J. Fatty acid oxidation and meiotic resumption in mouse oocytes. Mol Reprod Dev 2009;76(9):844–53.
12. Wu LL-Y, Dunning KR, Yang X, Russell DL, Lane M, Norman RJ, et al. High-Fat Diet Causes Lipotoxicity Responses in Cumulus–Oocyte

Complexes and Decreased Fertilization Rates. Endocrinology 2010;151(11):5438–45.

13. Yang X, Wu LL, Chura LR, Liang X, Lane M, Norman RJ, et al. Exposure to lipid-rich follicular fluid is associated with endoplasmic reticulum stress and impaired oocyte maturation in cumulus-oocyte complexes. Fertil Steril 2012;97(6):1438–43.
14. Tiwari M, Tripathi A, Chaube SK. Presence of encircling granulosa cells protects against oxidative stress-induced apoptosis in rat eggs cultured in vitro. Apoptosis 2017;22(1):98–107.
15. Gioacchini G, Valle LD, Benato F, Fimia GM, Nardacci R, Ciccosanti F, et al. Interplay between autophagy and apoptosis in the development of Danio rerio follicles and the effects of a probiotic. Reprod Fertil Dev 2013;25(8):1115–25.
16. Choi J, Jo MM, Lee EM, Choi D. Induction of apoptotic cell death via accumulation of autophagosomes in rat granulosa cells. Fertil Steril 2011;95(4):1482–6.
17. Duerrschmidt N, Zabirnyk O, Nowicki M, Ricken A, Hmeidan FA, Blumenauer V, et al. Lectin-Like Oxidized Low-Density Lipoprotein Receptor- 1-Mediated Autophagy in Human Granulosa Cells as an Alternative of Programmed Cell Death. Endocrinology 2006;147(8):3851–60.
18. Nakahara K, Saito H, Saito T, Ito M, Ohta N, Sakai N, et al. Incidence of apoptotic bodies in membrana granulosa of the patients participating in an in vitro fertilization program. Fertil Steril 1997;67(2):302–8.
19. Sifer C, Bénifla J-L, Bringuier A-F, Porcher R, Blanc-Layrac G, Madélénat P, et al. Could induced apoptosis of human granulosa cells predict in vitro fertilization–embryo transfer outcome? A preliminary study of 25 women. Eur J Obstet Gynecol Reprod Biol 2002;103:150–3.
20. Matthäus C, Bird B, Miljković M, Chernenko T, Romeo M. Infrared and Raman Microscopy in Cell Biology. Methods Cell Biol 2008;89(8):275–308.
21. Giorgini E, Gioacchini G, Sabbatini S, Conti C, Vaccari L, Borini A, et al. Vibrational characterization of female gametes: a comparative study. Analyst 2014;139(20):5049–60.

22. Lyng F, Ramos I, Ibrahim O, Byrne H. Vibrational Microspectroscopy for Cancer Screening. Appl Sci 2015;5(1):23–35.
23. Baker MJ, Trevisan J, Bassan P, Bhargava R, Butler HJ, Dorling KM, et al. Using Fourier transform IR spectroscopy to analyze biological materials. Nat Protoc 2014;9(8):1771–91.
24. Wolkers WF, Oldenhof H. In situ FTIR studies on mammalian cells. Spectroscopy 2010;24(5):525–34.
25. Baena JR, Lendl B. Raman spectroscopy in chemical bioanalysis. Curr Opin Chem Biol 2004;8(5):534–9.
26. Downes A, Elfick A. Raman spectroscopy and related techniques in biomedicine. Sensors 2010;10(3):1871–89.
27. Conti C, Ferraris P, Giorgini E, Rubini C, Sabbatini S, Tosi G, et al. FT-IR microimaging spectroscopy: A comparison between healthy and neoplastic human colon tissues. J Mol Struct 2008;881(1–3):46–51.
28. Giorgini E, Conti C, Ferraris P, Sabbatini S, Tosi G, Rubini C, et al. Effects of Lactobacillus rhamnosus on zebrafish oocyte maturation: An FTIR imaging and biochemical analysis. Anal Bioanal Chem 2010;398(7–8):3063–72.
29. Lyng F, Faoláin E, Conroy J, Meade A, Knief P, Duffy B, et al. Vibrational spectroscopy for cervical cancer pathology, from biochemical analysis to diagnostic tool. Exp Mol Pathol 2007;82:121–9.
30. Farhane Z, Bonnier F, Casey A, Maguire A, O'Neill L, Byrne HJ. Cellular discrimination using in vitro Raman micro spectroscopy: the role of the nucleolus. Analyst 2015;140(17):5908–19.
31. Efeoglu E, Casey A, Byrne HJ. In vitro monitoring of time and dose dependent cytotoxicity of aminated nanoparticles using Raman spectroscopy. Analyst 2016;141(18):5417–31.
32. Efeoglu E, Casey A, Byrne HJ. Determination of spectral markers of cytotoxicity and genotoxicity using in vitro Raman microspectroscopy: cellular responses to polyamidoamine dendrimer exposure. Analyst 2017;142(20):3848–56.
33. Gioacchini G, Giorgini E, Vaccari L, Ferraris P, Sabbatini S, Bianchi V, et al. A new approach to evaluate aging effects on human oocytes: Fourier

transform infrared imaging spectroscopy study. Fertil Steril 2014;101(1):120–7.

34. Borini A, Sciajno R, Bianchi V, Sereni E, Flamigni C, Coticchio G. Clinical outcome of oocyte cryopreservation after slow cooling with a protocol utilizing a high sucrose concentration. Hum Reprod 2005;21(2):512–7.
35. Baker MJ, Gazi E, Brown MD, Shanks JH, Clarke NW, Gardner P. Investigating FTIR based histopathology for the diagnosis of prostate cancer. J Biophotonics 2009;2(1–2):104–13.
36. Tosi G, Conti C, Giorgini E, Ferraris P, Garavaglia MG, Sabbatini S, et al. FTIR microspectroscopy of melanocytic skin lesions: a preliminary study. Analyst 2010;135(12):3213–9.
37. Giorgini E, Tosi G, Conti C, Staibano S, Ilardi G, Sabbatini S. Molecular and Biomolecular Spectroscopy FTIR microspectroscopic characterization of Spitz nevi. Spectrochim Acta Part A Mol Biomol Spectrosc 2015;141:99–103.
38. Movasaghi Z, Rehman S, Rehman IU. Raman Spectroscopy of Biological Tissues. Appl Spectrosc Rev 2007;42:493–541.
39. Bustin SA, Benes V, Garson JA, Hellemans J, Huggett J, Kubista M, et al. The MIQE Guidelines: Minimum Information for Publication of Quantitative Real-Time PCR Experiments. Clin Chem 2009;55(4):611–22.
40. Pfaffl MW. A new mathematical model for relative quantification in real-time RT-PCR. Nucleic Acids Res 2001;29(9):45e–45.
41. Vandesompele J, De Preter K, Pattyn F, Poppe B, Van Roy N, De Paepe A, et al. Accurate normalization of real-time quantitative RT-PCR data by geometric averaging of multiple internal control genes. Genome Biol 2002;3(7):research0034.1-0034.11.
42. Kordus RJ, LaVoie HA. Granulosa cell biomarkers to predict pregnancy in ART: pieces to solve the puzzle. Reproduction 2017;153(2):R69–83.
43. Papler TB, Bokal EV, Maver A, Kopitar AN, Lovrečić L. Transcriptomic analysis and meta-analysis of human granulosa and cumulus cells. PLoS One 2015;10(8):1–22.
44. Oleszko A, Olsztyńska-Janus S, Walski T, Grzeszczuk-Kuć K, Bujok J, Gałecka K, et al. Application of FTIR-ATR spectroscopy to determine

the extent of lipid peroxidation in plasma during haemodialysis. Biomed Res Int 2015;2015:1–8.

45. Benseny-Cases N, Klementieva O, Cotte M, Ferrer I, Cladera J. Microspectroscopy (μFTIR) reveals co-localization of lipid oxidation and amyloid plaques in human Alzheimer disease brains. Anal Chem 2014;86(24):12047–54.
46. Gregersen N, Bross P, Vang S, Christensen JH. Protein Misfolding and Human Disease. Annu Rev Genomics Hum Genet 2006;7(1):103–24.
47. Prieto L, Quesada JF, Cambero O, Pacheco A, Pellicer A, Codoceo R, et al. Analysis of follicular fluid and serum markers of oxidative stress in women with infertility related to endometriosis. Fertil Steril 2012;98:126–30.
48. Carvalho LFP, Abrão MS, Biscotti C, Sharma R, Nutter B, Falcone T. Oxidative Cell Injury as a Predictor of Endometriosis Progression. Reprod Sci 2013;20(6):688–98.
49. Ngô C, Ché C, Nicco C, Weill B, Chapron C, Dé F, et al. Reactive Oxygen Species Controls Endometriosis Progression. Am J Pathol 2009;175(1):225–34.
50. Seino T, Saito H, Kaneko T, Takahashi T, Kawachiya S, Kurachi H. Eight-hydroxy-2'-deoxyguanosine in granulosa cells is correlated with the quality of oocytes and embryos in an in vitro fertilization– embryo transfer program. Fertil Steril 2002;77(6):1184–90.
51. Da Broi MG, De Albuquerque FO, De Andrade AZ, Cardoso RL, Jordão Junior AA, Navarro PA. Increased concentration of 8-hydroxy-2′-deoxyguanosine in follicular fluid of infertile women with endometriosis. Cell Tissue Res 2016;366:231–42.
52. Komar CM. Peroxisome proliferator-activated receptors (PPARs) and ovarian function--implications for regulating steroidogenesis, differentiation, and tissue remodeling. Reprod Biol Endocrinol 2005;3:41.
53. Froment P, Gizard F, Defever D, Staels B, Dupont J, Monget P. Peroxisome proliferator-activated receptors in reproductive tissues: from gametogenesis to parturition. J Endocrinol 2006;189(2):199–209.

54. Tyagi S, Gupta P, Saini AS, Kaushal C, Sharma S. The peroxisome proliferator-activated receptor: A family of nuclear receptors role in various diseases. J Adv Pharm Technol Res 2011;2(4):236–40.
55. Beloribi-Djefaflia S, Vasseur S, Guillaumond F. Lipid metabolic reprogramming in cancer cells. Oncogenesis 2016;5(1):e189.
56. Wise LA, Palmer JR, Rosenberg L, Haddad SA, Ruiz-Narváez EA. FASN, dietary fat intake, and risk of uterine leiomyomata in the Black Women's Health Study. Fertil Steril 2016;106(5):1136–41.
57. Pelland AMD, Corbett HE, Baltz JM. Amino Acid transport mechanisms in mouse oocytes during growth and meiotic maturation. Biol Reprod 2009;81(6):1041–54.
58. Eppig JJ, Pendola FL, Wigglesworth K, Pendola JK. Mouse Oocytes Regulate Metabolic Cooperativity Between Granulosa Cells and Oocytes: Amino Acid Transport. Biol Reprod 2005;73:351–7.
59. Berlett BS, Stadtman ER. Protein Oxidation in Aging, Disease, and Oxidative Stress. J Biol Chem 1997;272(33):20313–6.
60. Sutton-Mcdowall ML, Gilchrist RB, Thompson JG. The pivotal role of glucose metabolism in determining oocyte developmental competence. Reproduction 2010;139(4):685–95.
61. Joost H-G, Bell GI, Best JD, Birnbaum MJ, Charron MJ, Chen YT, et al. Nomenclature of the GLUT/SLC2A family of sugar/polyol transport facilitators. Am J Physiol Endocrinol Metab 2002;282(4):E974-6.
62. Herbert A, Rich A. The biology of left-handed Z-DNA. J Biol Chem 1996;271(20):11595–8.
63. Rothenburg S, Koch-Nolte F, Haag F. DNA methylation and Z-DNA formation as mediators of quantitative differences in the expression of alleles. Immunol Rev 2001;184(1):286–98.
64. Hussein MR. Apoptosis in the ovary: molecular mechanisms. Hum Reprod Update 2005;11(2):162–78.
65. Fujino K, Yamashita Y, Hayashi A, Asano M, Morishima S, Ohmichi M. Survivin gene expression in granulosa cells from infertile patients undergoing in vitro fertilization–embryo transfer. Fertil Steril 2008;89(1):60–5.

66. Li F, Ambrosini G, Chu EY, Plescia J, Tognin S, Marchisio PC, et al. Control of apoptosis and mitotic spindle checkpoint by survivin. Nature 1998;396(6711):580–4.
67. Cohen GM. Caspases: the executioners of apoptosis. Biochem J 1997;326 (Pt 1:1–16.
68. Liang XH, Jackson S, Seaman M, Brown K, Kempkes B, Hibshoosh H, et al. Induction of autophagy and inhibition of tumorigenesis by beclin 1. Nature 1999;402(6762):672–6.
69. Kabeya Y, Mizushima N, Ueno T, Yamamoto A, Kirisako T, Noda T, et al. LC3, a mammalian homologue of yeast Apg8p, is localized in autophagosome membranes after processing. EMBO J 2000;19(21):5720–8.
70. Kitajima M, Defr S, Dolmans M-M, Colette S, Squifflet J, Langendonckt A Van, et al. Endometriomas as a possible cause of reduced ovarian reserve in women with endometriosis. Fertil Steril 2011;96:685–91.
71. Ferrero S, Scala C, Tafi E, Racca A, Venturini PL, Leone U, et al. Impact of large ovarian endometriomas on the response to superovulation for in vitro fertilization: A retrospective study. 2017.

Chapter 7

How do plasticizers BPA and DGB alter the macromolecular composition of luteinized GCs?

Notarstefano et al.

(manuscript in preparation)

Introduction

In recent years, the concern regarding the impact of plasticizers on human reproduction is growing due to their widespread diffusion in the environment, such as air, soil and water samples, as described in several studies (1,2). Plasticizers are chemicals compounds routinely used to ameliorate plastics in terms of flexibility and workability (3). They are known to have a hormone-like activity, functioning as endocrine disrupting chemicals (EDCs). Bisphenol-A (BPA), one of the most used plasticizer (4–6), is described as an oestrogen-like compound, as it stimulates the activity of the nuclear oestrogen receptors (ERs), ERα and ERβ, leading to variations in gene expression patterns (7). In the field of reproduction, BPA has been shown to adversely correlate with many functionalities and features in males, such as lower sperm concentration, count, vitality, and progressive motility (8). In females, it causes implantation failure, lower antral follicle counts, alterations in oviduct and uterine morphology, and abnormal oestrous cyclicity (9). Less is known about diethylene glycol dibenzoate (DGB), recently approved by the European Chemical Agency as an alternative to phthalates in the manufacturing of plastics (10,11), and used in latex products, industrial coatings and certain printing inks.

The discovery of BPA in human follicular fluid of women undergoing in vitro fertilization (IVF) procedures raised many concerns: the ovarian follicle is an extremely fragile microenvironment, and the presence of EDCs may be a risk factor for impaired oocyte development, as well as for a correct embryo development (12). In this light, we exploited FTIR Microspectroscopy to

examine the effects on human luteinized Granulosa cells (GCs) of two different plasticizers (BPA and DGB), at three doses (1 ng/ml, 10 ng/ml, 100 ng/ml), selected on the basis of BPA concentration found in human follicular fluids. FTIRM is a well-established vibrational technique, extensively applied in life sciences to study the biomolecular makeup of cells and tissues (13,14). The analysis of IR spectral bands in terms of position, intensity and width, makes it possible to detect the presence and relative quantity of functional groups, bonding types and molecular conformation of the most important biomolecules (proteins, lipids, sugars and nucleic acids) (15). FTIRM measurements were carried out on living GCs, using a biocompatible microfluidic device system, which maintain cells viable and in physiological conditions for the time of the study (16).

Experimental section

The study was approved by the Internal Review Board of Tecnobios Procreazione, in full accordance with the Declaration of Helsinki (World Med. Ass. 2013). To participate in this investigation, each patient signed a written consent, which included the donation of GCs. All samples were anonymous and marked by a code and hence it was impossible to correlate them with a physical person.

Luteinized GCs sample collection

15 patients enrolled in an in vitro fertilization program at Tecnobios Procreazione were recruited according to the following inclusion criteria: age

of 32±3.3 years; regular ovulatory menstrual cycles; FSH < 10 IU/I on day 3 of the menstrual cycle; non-smokers, and without ovarian infertility nor endometriosis diagnosis. Controlled ovarian stimulation was induced using leuprorelin (Enantone, Takeda, Rome, Italy) and rFSH (Gonal-F, Serono, Rome, Italy, or Puregon Organon, Rome, Italy). HCG at 10,000 IU (Gonasi, Amsa, Rome, Italy) was administered when one or more follicles reached a diameter of ca. 23 mm (17).

From each patient, luteinized GCs were collected at the end of the treatment from all the follicles, according to the following protocol. The follicular fluid was centrifuged at 1100 x g for 10 min and the pellet was resuspended in 2 ml of gamete medium, overlaid on 1 ml pure sperm 50% (obtained by pure sperm 80 and gamete buffer medium) and centrifuged again at 1600x g for 13 min to separate GCs from the red blood cells. After centrifugation, GCs were recovered, placed in 1 ml of NaCl 0.9% solution and then centrifuged at 300x g for 10 minutes. The supernatant was discarded and the pellet was resuspended in 1 ml of NaCl 0.9% solution and centrifuged again at 300x g for 10 minutes. All retrieved GCs were pooled and then divided into different aliquots, cultured for 48 hours (18) in only DMEM/F12 culture medium (**CTRL**), or also with the addition of BPA and DGB at three different concentrations (1 ng/ml; **1ng**; 10 ng/ml: **10ng**; 100 ng/ml: **100ng**). The experiment was carried out in triplicate.

FTIRM measurements and data analysis

FTIRM measurements were carried out at the infrared beamline SISSI at Elettra Sincrotrone Trieste. A Hyperion 3000 Vis-IR microscope coupled with a Bruker VERTEX 70 interferometer (OPUS 7.1 software package, Bruker Optics, Ettlingen, Germany) was used. The spectrometer was equipped with a HgCdTe (MCT_A) detector operating at liquid nitrogen temperature, which covers the entire IR spectral range from 4000 to 800 cm^{-1}.

GCs were harvested from the culture flask by trypsinization and were centrifuged at 1200 rpm for 5 min. The pellet was washed twice with physiological solution (NaCl 0.9%); then, cells were resuspended in 15 µl of physiological solution and dropped into a specific biocompatible microfluidic device, developed by the team of SISSI (Synchrotron Infrared Source for Spectroscopic and Imaging) beamline, Elettra Synchrotron Trieste. This device was composed by two CaF_2 optical windows (0.5-mm thick, 13 and 10 mm diameter respectively), spaced apart 7.5 µm (19,20). On each sample, ~30 areas containing 3/4 cells were selected by visible microscopy, on which IR spectra were collected in transmission mode. Microscope knife-edge apertures were set at 30×30 $µm^2$ (256 scans, spectral resolution of 4 cm^{-1}, zero-filling factor of 2 in the spectral range 4000−800 cm^{-1}, scanner velocity 40 kHz) using a 15X Schwarzschild condenser and objective (NA = 0.4). Background, taken on 1 mm CaF_2 clean window, and buffer medium spectra were collected using the same parameters.

All the collected spectra were corrected for the contribution of atmospheric carbon dioxide and water vapour with the compensation routine of OPUS 7.1 software (Bruker Optics GmbH). Then to elucidate the cellular spectral details hidden by the prominent water features, the spectral contribution of water medium was subtracted from each GCs spectrum using the in-house optimized Matlab routine described by Vaccari et al. (20). Spectra having at 1660 cm^{-1} a peak height lower than 0.07 a.u. were discarded. The remaining IR spectra were vector normalized and then subjected to PCA (Principal Components Analysis), by using an in-house developed algorithm with R Studio (RStudio: Integrated Development for R. RStudio, Inc., Boston, MA). PCA is a multivariate technique widely used to highlight spectral variability among different groups or to recognize outliers. It allows the discrimination of different spectral groups of similar variability, using Principal Components (PCs) and scores plots; moreover, its usefulness in spectroscopy studies resides in the loadings, in which the variations among groups are highlighted according to wavenumbers (21). Once each spectrum was described by scores in the new space of scores plot, spectra outside 90% confidence ellipse in PC2 *vs* PC1 space were removed.

IR spectra were also integrated under the spectral regions reported in Table 1, by using OPUS 7.1 software.

Spectral Interval (cm^{-1})	Vibrational mode assignment	Cellular functional groups	Ref.
3000−2836	Symmetric and asymmetric $CH_{2/3}$ stretching modes, **Lipids**	Saturated alkyl chains of cellular lipids (mainly) and proteins	(15)
1591−1481	Mainly C-N stretching and N-H deformation in peptide linkage, Amide II, **AII**	Cellular proteins*	(22)
1480-1426	$CH_{2/3}$ bending, **CH2-3**	Methyl and methylene groups of cellular proteins	(23)
1426-1372	Symmetric stretching of COO- groups of glutamate and aspartate, **GLU-ASP**	Glutamate and aspartate	(23)
1286-1191	Asymmetric stretching modes of phosphate groups, **Ph1**	Phosphate moieties of nucleic acids (mainly), phospholipids and phosphorylated proteins	(24,25)
1140-1030	Symmetric stretching modes of phosphate groups, **Ph2**	Phosphate moieties of phosphorylated proteins (mainly), phospholipids and nucleic acids	(26,25)
2990−2899 & 1775−950	Sum of all the vibrations indicated above, **CELL**	Overall cellular biomolecular content	

* Amide I was not taken into account due to its superimposition with the vibrational water contribution.

Table 1. List of the spectral intervals on which the area integrals were calculated, together with the vibrational mode assignment, the assigned name (**bold** characters) and the corresponding cellular functional groups.

Integrated areas were used to calculate the band area ratios reported in Table 2.

Banda area ratios	Biological significance
LIPIDS/CELL	Total cellular lipids
AII/CELL	Total cellular proteins
PH1/CELL	Total cellular phosphate groups
PH2/CELL	
CH2-3/CELL	Methyl and methylene groups of amino acid side chains
GLU-ASP/CELL	Glutamate and aspartate amount

Table 2. Band area ratios of the integrals defined in Table 1, label used and its biological significance.

Statistical analysis

Data were presented as mean ± S.D. Significant differences between experimental groups were determined by means of a factorial analysis of variance (one-way ANOVA), followed by Tukey's multiple comparisons test, using the statistical software package Prism6 (Graphpad Software, Inc. USA). Statistical significance was set at $p < 0.05$.

Results

Human GCs samples treated for 48 hours with different concentrations of BPA and DGB, were analysed using FTIRM. Representative FTIRM absorbance and second derivative spectra of GCs are reported in Figure 1.

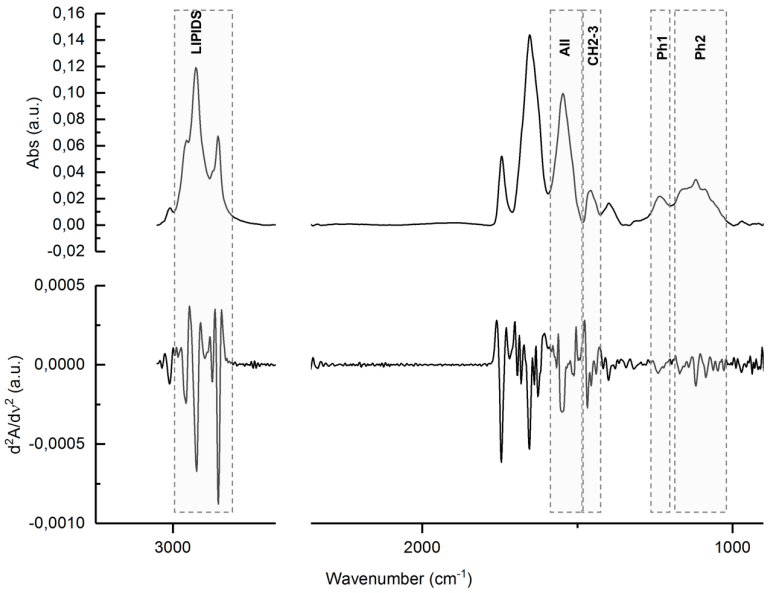

Figure 1. Representative absorbance and second derivative spectra of GCs after subtraction of water contribution. The spectral regions considered in the study are highlighted (3000–2836 cm^{-1}: LIPIDS; 1591-1481 cm^{-1}: AII; 1480-1426 cm^{-1}: CH2-3; 1286–1191 cm^{-1}: Ph1; 1140-1030 cm^{-1}: Ph2).

PCA was carried out to highlight spectral variability among different groups, and to discriminate different spectral groups of similar variability. Regarding BPA treatment, Figure 2A shows the PCA score plot of GCs spectra from **CTRL**, **1ng**, **10ng**, and **100ng** experimental groups. A good segregation of the **CTRL** group respect to the others was observed along the PC1 axis (56.69% of the system variance). The pair-wise comparisons of **CTRL** vs **1ng**, **CTRL** vs **10ng**, and **CTRL** vs **100ng** GCs spectra are shown in Figures 2B, 2C and 2D, respectively. All plots clearly show that PC1 differentiates between the control group and each of the others. The PC1 loadings of all the PCA tests (Figure 2E), showed that the most visible discriminant features among the experimental groups are the spectral regions corresponding to the alkyl chains stretching modes of lipids (3000-2800 cm^{-1}) and Amide II band of proteins (1591-1481 cm^{-1}).

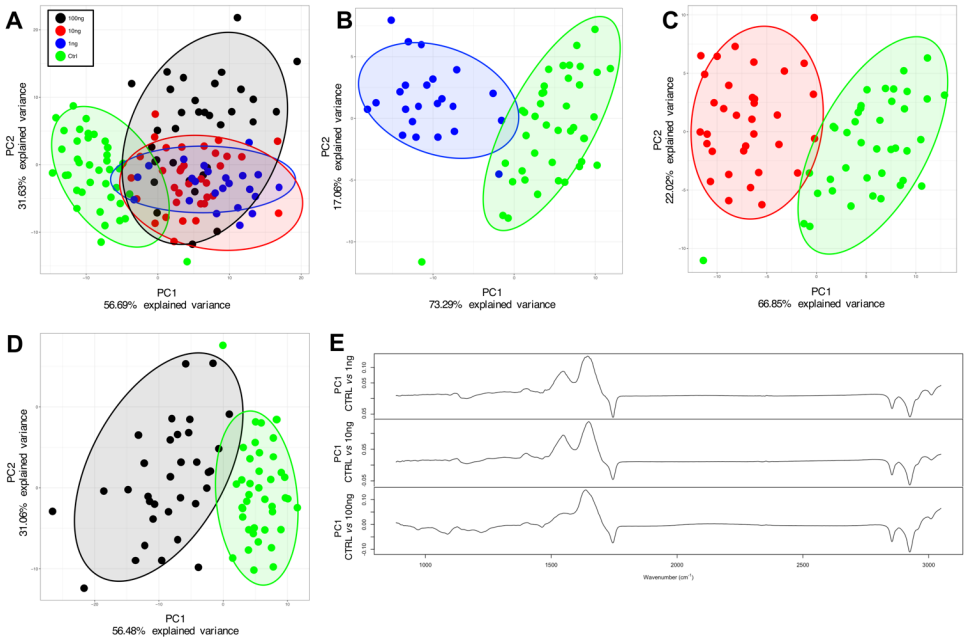

Figure 2. Principal Components Analysis of BPA experiment. PCA score plot of the analysis performed on all the experimental groups (A), and pair-wise PCA score plot of **CTRL** vs **1ng** (B), **CTRL** vs **10ng** (C), and **CTRL** vs **100ng** (D). PC1 loadings of the pair-wise PCA tests (E).

Similarly, regarding DGB treatment, Figure 3A reports the PCA score plot of GCs spectra from **CTRL**, **1ng**, **10ng**, and **100ng** experimental groups. A complete segregation of the **CTRL** group respect to the others was observed along the PC1 axis (53.49% of the system variance). The pair-wise comparisons of **CTRL** vs **1ng**, **CTRL** vs **10ng**, and **CTRL** vs **100ng** GCs spectra are showed in Figures 3B, 3C and 3D, respectively. In all plots, PC1 differentiates between the control group and each of the others. The PC1

loadings of all the PCA tests (Figure 3E), showed that the most visible discriminant features among the experimental groups are the spectral regions corresponding to alkyl chains stretching modes of lipids (3000-2800 cm^{-1}), Amide II band of proteins (1591-1481 cm^{-1}) and phosphates and carbohydrates vibrational modes (1350-1000 cm^{-1}).

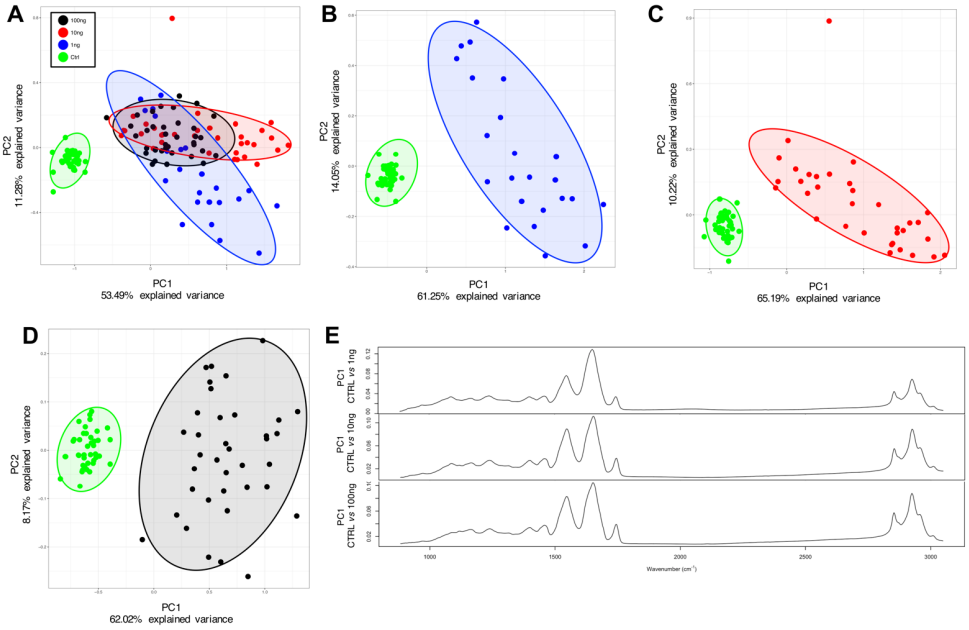

Figure 3. Principal Components Analysis of DGB experiment. PCA score plot of the analysis performed on all the experimental groups (A), and pair-wise PCA score plot of **CTRL** vs **1ng** (B), **CTRL** vs **10ng** (C), and **CTRL** vs **100ng** (D). PC1 loadings of the pair-wise PCA tests (E).

To compare the alterations of the relative content of cellular biomolecules depending of doses of BPA and DGB, specific band area ratios were calculated for all the experimental groups (Figures 4 and 5). Regarding BPA treatment, the analysis of the numerical variations of band area ratios among the experimental groups led to the following considerations: (i) the total amount of cellular lipids (LIPID/CELL), calculated as ratio between the integrated area in the 3000–2836 cm^{-1} spectral region and the CELL value, showed a significant increase in GCs treated with all the doses of BPA (Figure 4A); (ii) the total amount of cellular proteins (AII/CELL), calculated as ratio between the integrated area in the 1591-1481 cm^{-1} spectral region and the CELL value, showed a significant decrease in GCs treated with all the doses of BPA (Figure 4B), in accordance with the ratio CH2-3/CELL, calculated dividing the area integral of the band centered at ~1460 cm^{-1} and the CELL value, assigned to the methyl and methylene groups of amino acid side chains (Figure 4F); (iii) the total amount of phosphate groups, calculated as the ratio between the integrated area in the 1286–1191 cm^{-1} spectral region and the CELL value (Ph1/CELL), and between the integrated area in the 1140–1030 cm^{-1} spectral region and the CELL value (Ph2/CELL), showed a significant increase only in GCs treated with the highest dose of BPA (100 ng/ml) (Figures 4C,D); (iv) the total amount of glutamate and aspartate (GLU-ASP/CELL), calculated as the ratio between the area integral of the band centred at ~1400 cm^{-1} and the CELL value, showed a significant decrease in treated GCs at all the doses (Figure 4F).

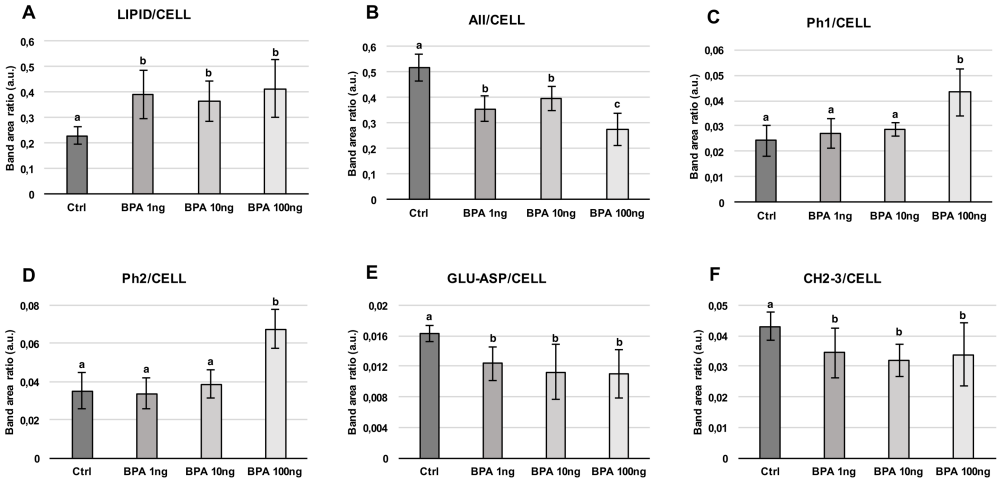

Figure 4. Numerical variations of the following band area ratios for the **CTRL**, **BPA 1ng**, **BPA 10ng** and **BPA 100ng** experimental groups: LIPIDS/CELL (spectral region 3050-2800 cm^{-1}) (A); PROTEINS/CELL (spectral region 1723-1481 cm^{-1}) (B); Ph1/CELL (band at ~1240 cm^{-1}) (C); Ph2/CELL (band at ~1080 cm^{-1}) (D); GLU-ASP/CELL (band at ~1400 cm^{-1}) (E); CH2-3/CELL (band at ~1460 cm^{-1}) (F). Values are reported as mean±SD. Significant differences were determined as described in the Experimental section (see Statistical analysis). Different letters above columns indicate statistical differences with respect to **CTRL**.

The same analysis was conducted on cells treated with DGB and led to the following conclusions: (i) the total amount of cellular lipids (LIPID/CELL) showed a significant decrease in GCs treated with the lowest dose of DGB (1 ng/ml), and a significant increase with the medium dose (10 ng/ml) (Figure 5A); (ii) the total amount of cellular proteins (AII/CELL) did not show a significant alteration with any tested dose of DGB (Figure 5B); (iii) the total amount of phosphate groups (Ph1/CELL and Ph2/CELL) showed a

significant decrease in GCs treated with the medium and the highest doses of DGB (10 ng/ml and 100 ng/ml) (Figures 5C,D).

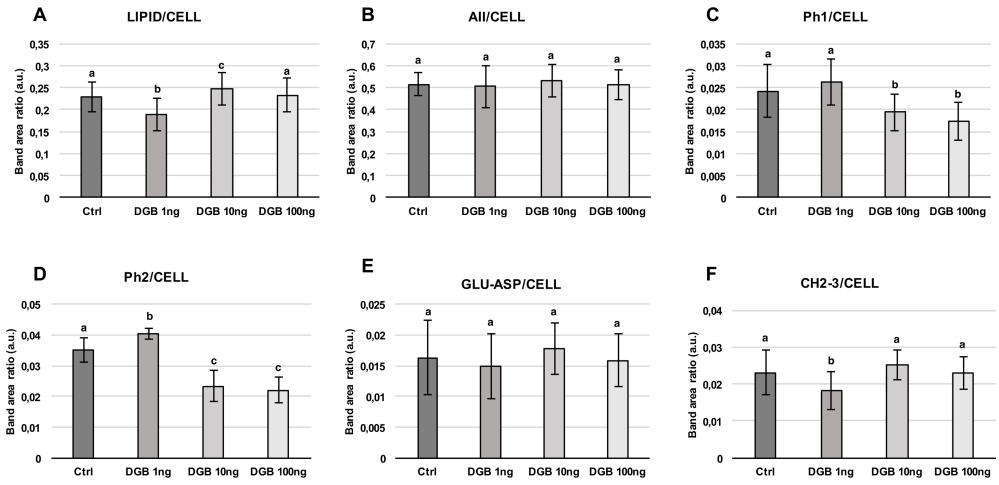

Figure 5. Numerical variations of the following band area ratios for the **CTRL**, **DGB 1ng**, **DGB 10ng** and **DGB 100ng** experimental groups: LIPIDS/CELL (spectral region 3050-2800 cm^{-1}) (A); PROTEINS/CELL (spectral region 1723-1481 cm^{-1}) (B); Ph1/CELL (band at ~1240 cm^{-1}) (C); Ph2/CELL (band at ~1080 cm^{-1}) (D); GLU-ASP/CELL (band at ~1400 cm^{-1}) (E); CH2-3/CELL (band at ~1460 cm^{-1}) (F). Values are reported as mean±SD. Significant differences were determined as described in the Experimental section (see Statistical analysis). Different letters above columns indicate statistical differences with respect to **CTRL**.

Discussion

It is well established that BPA, widely used in the manufacturing of plastics, has a hormone-like activity, functioning as EDCs. It is an oestrogen-like compound, able to induce alterations in gene expression patterns, and to

adversely correlate with almost all the male and female reproductive functionalities (8,9). In addition, the discovery of BPA in human follicular fluids has raised many concerns about the risk of impairing oocyte development (12). Several studies carried out on mammals, showed that BPA affects rat (27), swine (28,29) and murine (30) GCs steroidogenesis, one of the crucial functionalities of these follicular cells. BPA exerts a negative effect also on human GCs *in vitro*: Mansur and colleagues reported that BPA results in a significant decrease in estradiol and progesterone biosynthesis, although only at very high and supra-physiological levels (18). Less is known about DGB, recently approved by the European Chemical Agency as a substitute of phthalates in the manufacturing of plastics (10,11), and used in latex products, industrial coatings and certain printing inks. This use of DGB raises questions as to whether it can have negative effects, or be a good choice as alternative to phthalates.

In this study, we examined the effects on human luteinized GCs of BPA and DGB at three doses (1 ng/ml, 10 ng/ml, 100 ng/ml), selected on the basis of BPA concentration found in human follicular fluids (12). FTIRM was chosen to analyse living GCs, thanks to a biocompatible IR-Vis transparent microfluidic device, which made it possible to keep the cells viable and in physiological conditions for the time of the study (16).

Both for BPA and DGB, PCA scores plots showed a clear segregation of **CTRL** spectra from all the other experimental groups. In particular, in GCs treated with BPA the most discriminant spectral features were linked to lipid and protein vibrational modes, while in GCs treated with DGB, also the

spectral region related to phosphates and carbohydrates was involved, suggesting different effects of the two tested plasticizers on GCs.

For a deeper understanding of the biochemical modifications induced by BPA and DGB on GCs, IR spectra were integrated under the main spectral regions, and specific band area ratios were calculated for all the experimental groups. A general evaluation of the obtained numerical values clearly displays that both BPA and DGB affect the biomolecular composition of GCs, but in a different way, and that apparently DGB induces a less significant alteration.

It is known that BPA plays a role in the occurrence of some gynaecological diseases, such as PCOS (31,32) and endometriosis (33,34), hence the results obtained shed new light on the mechanisms by which this compound impairs ovarian health. In GCs treated with BPA, the increase of lipid amount (LIPID/CELL) in **1ng**, **10ng** and **100ng** experimental groups with respect to **CTRL** suggests a possible activation of lipid metabolism (35–37) in treated GCs. The potential of BPA to impair lipid metabolism has been already described in different organisms and organs (38–40): here, for the first time, the same effects were highlighted in human GCs by using FTIRM.

The decrease in protein amount (AII/CELL) in **1ng**, **10ng** and **100ng** experimental groups with respect to **CTRL** is indicative of a depletion of this class of biomolecules, a known effect already found in various types of cellular stress (41,42). As the signal of Amide II band (taken as total proteins) is given by N-H bending and C-N stretching modes of proteins, this result suggests the possible activation of peptide bond cleavage, presumably due to the attack of

reactive oxygen species on glutamyl, aspartyl, and prolyl side chains (43). To the best of our knowledge, an effect of BPA on protein degradation has not yet been described, hence these results shed new light on the negative effects of BPA on the cell macromolecular architecture.

The band ratios Ph1/CELL and Ph2/CELL, both correlated with the vibrational modes of phosphate groups, follow the same trend: no change was observed in **1ng** and **10ng** experimental groups, while a significant increase was found with the highest dose of treatment.

Due to the lack of literature reports about the effects of DGB on reproductive functions, we aimed to investigate whether also DGB, like BPA, impacts on GCs. The numerical analysis of band area ratios showed that apparently DGB induced a less significant alteration of the biomolecular components of GCs, characterised by a non-monotonic dose-response curve typical of hormones and endocrine disruptors (44). The protein cellular content (AII/CELL) did not significantly change among the experimental groups. Conversely, the lipid amount (LIPID/CELL) was affected: the lowest dose (**1ng**) determined a decrease of lipids in GCs, while the intermediate one (**10ng**) an increase. Ph1/CELL and Ph2/CELL values were consistent with each other, with a significant decrease only in the **1ng** and the **10ng** experimental groups (Ph2/CELL was also characterized by a slight but significant increase with the lowest dose of treatment). All these results demonstrate, for the first time, that also DGB affects the macromolecular architecture of human GCs, but in a completely different way than BPA, suggesting different mechanisms of action of these two compounds.

In conclusion, FTIRM analysis of GCs treated with BPA confirmed the negative effects of this compound on these follicular cells and improved the knowledge of the mechanisms by which it affects the biomolecular building of such important cells, crucial for proper oocyte development and maturation. In addition, a new light was shed on DGB, recently proposed as alternative to phthalates. This preliminary study suggests the ability of this compound to alter the biochemical composition of GCs, making mandatory to further assess at biological level this and other new chemicals, before their employment in everyday objects.

References

1. Staples CA, Peterson DR, Parkerton TF, Adams WJ. The environmental fate of phtalate esters: a literature review. Chemosphere 1997;35(4):667–749.
2. Fromme H, Uchler TK, Otto T, Pilz K, Uller JM, Wenzel A. Occurrence of phthalates and bisphenol A and F in the environment. Water Res 2002;36:1429–38.
3. Horn O, Nalli S, Cooper D, Nicell J. Plasticizer metabolites in the environment. Water Res 2004;38(17):3693–8.
4. Kang J-H, Kondo F, Katayama Y. Human exposure to bisphenol A. Toxicology 2006;226(2–3):79–89.
5. Crain DA, Eriksen M, Iguchi T, Jobling S, Laufer H, LeBlanc GA, et al. An ecological assessment of bisphenol-A: Evidence from comparative biology. Reprod Toxicol 2007;24(2):225–39.
6. Rubin BS. Bisphenol A: An endocrine disruptor with widespread exposure and multiple effects. J Steroid Biochem Mol Biol 2011;127(1–2):27–34.
7. Matthews JB, Twomey K, Zacharewski TR. In Vitro and in Vivo Interactions of Bisphenol A and Its Metabolite, Bisphenol A Glucuronide, with Estrogen Receptors α and β. Chem Res Toxicol 2001;14(2):149–57.
8. Mínguez-Alarcón L, Hauser R, Gaskins AJ. Effects of bisphenol A on male and couple reproductive health: a review. Fertil Steril 2016;106(4):864–70.
9. Ziv-Gal A, Flaws JA. Evidence for bisphenol A-induced female infertility: a review (2007–2016). Fertil Steril 2016;106(4):827–56.
10. Deligio T. Phthalate Alternative Recognized By ECHA [Internet]. 2009;Available from: https://www.plasticstoday.com/content/phthalate-alternative-recognized-echa/97715546012383
11. Kermanshahi pour A, Cooper DG, Mamer OA, Maric M, Nicell JA. Mechanisms of biodegradation of dibenzoate plasticizers. Chemosphere 2009;77(2):258–63.
12. Ikezuki Y, Tsutsumi O, Takai Y, Kamei Y, Taketani Y. Determination of bisphenol A concentrations in human biological fluids reveals significant early prenatal exposure. Hum Reprod 2002;17(11):2839–41.

13. Pilling M, Gardner P. Fundamental developments in infrared spectroscopic imaging for biomedical applications. Chem Soc Rev 2016;45(7):1935–57.
14. Moss DA, Keese M, Pepperkok R. IR microspectroscopy of live cells. Vib Spectrosc 2005;38:185–91.
15. Baker MJ, Trevisan J, Bassan P, Bhargava R, Butler HJ, Dorling KM, et al. Using Fourier transform IR spectroscopy to analyze biological materials. Nat Protoc 2014;9(8):1771–91.
16. Doherty J, Cinque G, Gardner P. Single cell analysis using Fourier transform infrared microspectroscopy. Appl Spectrosc Rev 2017;52(6):560–87.
17. Borini A, Sciajno R, Bianchi V, Sereni E, Flamigni C, Coticchio G. Clinical outcome of oocyte cryopreservation after slow cooling with a protocol utilizing a high sucrose concentration. Hum Reprod 2005;21(2):512–7.
18. Mansur A, Adir M, Yerushalmi G, Hourvitz A, Gitman H, Yung Y, et al. Does BPA alter steroid hormone synthesis in human granulosa cells in vitro? Hum Reprod 2016;31(7):1562–9.
19. Birarda G, Grenci G, Businaro L, Marmiroli B, Pacor S, Piccirilli F, et al. Infrared microspectroscopy of biochemical response of living cells in microfabricated devices. Vib Spectrosc 2010;53(1):6–11.
20. Vaccari L, Birarda G, Businaro L, Pacor S, Grenci G. Infrared Microspectroscopy of Live Cells in Microfluidic Devices (MD-IRMS): Toward a Powerful Label-Free Cell-Based Assay. Anal Chem 2012;84(11):4768–75.
21. Bonnier F, Byrne HJ. Understanding the molecular information contained in principal component analysis of vibrational spectra of biological systems. Analyst 2012;137(2):322–32.
22. Mitri E, Kenig S, Coceano G, Bedolla DE, Tormen M, Grenci G, et al. Time-Resolved FT-IR Microspectroscopy of Protein Aggregation Induced by Heat-Shock in Live Cells. Anal Chem 2015;87(7):3670–7.
23. Movasaghi Z, Rehman S, Rehman I ur. Fourier Transform Infrared (FTIR) Spectroscopy of Biological Tissues. Appl Spectrosc Rev 2008;43(2):134–79.

24. Tosi G, Conti C, Giorgini E, Ferraris P, Garavaglia MG, Sabbatini S, et al. FTIR microspectroscopy of melanocytic skin lesions: a preliminary study. Analyst 2010;135(12):3213–9.
25. Giorgini E, Tosi G, Conti C, Staibano S, Ilardi G, Sabbatini S. Molecular and Biomolecular Spectroscopy FTIR microspectroscopic characterization of Spitz nevi. Spectrochim Acta Part A Mol Biomol Spectrosc 2015;141:99–103.
26. Gioacchini G, Giorgini E, Vaccari L, Ferraris P, Sabbatini S, Bianchi V, et al. A new approach to evaluate aging effects on human oocytes: Fourier transform infrared imaging spectroscopy study. Fertil Steril 2014;101(1):120–7.
27. Zhou W, Liu J, Liao L, Han S, Liu J. Effect of bisphenol A on steroid hormone production in rat ovarian theca-interstitial and granulosa cells. Mol Cell Endocrinol 2008;283(1–2):12–8.
28. Mlynarčíková A, Kolena J, Ficková M, Scsuková S. Alterations in steroid hormone production by porcine ovarian granulosa cells caused by bisphenol A and bisphenol A dimethacrylate. Mol Cell Endocrinol 2005;244(1–2):57–62.
29. Grasselli F, Baratta L, Baioni L, Bussolati S, Ramoni R, Grolli S, et al. Bisphenol A disrupts granulosa cell function. Domest Anim Endocrinol 2010;39(1):34–9.
30. Peretz J, Gupta RK, Singh J, Hernández-Ochoa I, Flaws JA. Bisphenol A impairs follicle growth, inhibits steroidogenesis, and downregulates rate-limiting enzymes in the estradiol biosynthesis pathway. Toxicol Sci 2011;119(1):209–17.
31. Tarantino G, Valentino R, Somma C Di, D'Esposito V, Passaretti F, Pizza G, et al. Bisphenol A in polycystic ovary syndrome and its association with liver-spleen axis. Clin Endocrinol (Oxf) 2013;78(3):447–53.
32. Kandaraki E, Chatzigeorgiou A, Livadas S, Palioura E, Economou F, Koutsilieris M, et al. Endocrine Disruptors and Polycystic Ovary Syndrome (PCOS): Elevated Serum Levels of Bisphenol A in Women with PCOS. J Clin Endocrinol Metab 2011;96(3):E480–4.

33. Rashidi BH, Amanlou M, Lak TB, Ghazizadeh M, Eslami B. A case–control study of bisphenol A and endometrioma among subgroup of Iranian women. J Res Med Sci 2016;21(10):7–9.
34. Itoh H, Iwasaki M, Hanaoka T, Sasaki H, Tanaka T, Tsugane S. Urinary bisphenol-A concentration in infertile Japanese women and its association with endometriosis: A cross-sectional study. Environ Health Prev Med 2007;12(6):258–64.
35. Rodríguez-Casado A, Alvarez I, Toledano A, de Miguel E, Carmona P. Amphetamine effects on brain protein structure and oxidative stress as revealed by FTIR microspectroscopy. Biopolymers 2007;86(5–6):437–46.
36. Vileno B, Jeney S, Sienkiewicz A, Marcoux PR, Miller LM, Forró L. Evidence of lipid peroxidation and protein phosphorylation in cells upon oxidative stress photo-generated by fullerols. Biophys Chem 2010;152(1–3):164–9.
37. Barraza-Garza G, Castillo-Michel H, De La Rosa LA, Martinez-Martinez A, Pérez-León JA, Cotte M, et al. Infrared Spectroscopy as a Tool to Study the Antioxidant Activity of Polyphenolic Compounds in Isolated Rat Enterocytes. Oxid Med Cell Longev 2016;2016.
38. Carnevali O, Notarstefano V, Olivotto I, Graziano M, Gallo P, Di Marco Pisciottano I, et al. Dietary administration of EDC mixtures: A focus on fish lipid metabolism. Aquat Toxicol 2017;185:95–104.
39. Martella A, Silvestri C, Maradonna F, Gioacchini G, Allarà M, Radaelli G, et al. Bisphenol A Induces Fatty Liver by an Endocannabinoid-Mediated Positive Feedback Loop. Endocrinology 2016;157(5):1751–63.
40. Lv Q, Gao R, Peng C, Yi J, Liu L, Yang S, et al. Bisphenol A promotes hepatic lipid deposition involving Kupffer cells M1 polarization in male mice. J Endocrinol 2017;234(2):143–54.
41. Prakash C, Kamboj VK, Ahlawat P, Kumar V. Structural and molecular alterations in arsenic-induced hepatic oxidative stress in rats: a FTIR study. Toxicol Environ Chem 2015;97(10):1408–21.
42. Shivanoor SM, David M. Fourier transform infrared (FT-IR) study on cyanide induced biochemical and structural changes in rat sperm. Toxicol Reports 2015;2:1347–56.

43. Berlett BS, Stadtman ER. Protein Oxidation in Aging, Disease, and Oxidative Stress. J Biol Chem 1997;272(33):20313–6.
44. Vandenberg LN, Colborn T, Hayes TB, Heindel JJ, Jacobs DR, Lee D-H, et al. Hormones and Endocrine-Disrupting Chemicals: Low-Dose Effects and Nonmonotonic Dose Responses. Endocr Rev 2012;33(3):378–455.

CONCLUSIONS

Granulosa cells are crucial for the proper development and maturation of the companion oocyte. They are responsible for many important follicular functions, such as the production of estradiol during follicular growth, the production of essential nutrients used as an energy source during oocyte maturation, the accumulation of oocyte secreted metabolites and the secretion of progesterone after ovulation. Hence, helpful information on oocyte quality can be derived by the study of these somatic cells, in terms of their functionality.

In this PhD project, FTIRM was applied for the first time for GCs characterization, to develop an innovative method for evaluating the quality of human oocytes. The vibrational fingerprint of GCs was evaluated and statistically correlated with the corresponding oocyte clinical outcome. This could represent a new, reliable, objective and fast tool to be applied in ART routine for oocyte quality assessment.

Besides this main topic, the impairment induced by endogenous and exogenous factors on the biochemical composition, metabolism and cellular activity of GCs was also investigated by Fourier Transform Infrared and Raman spectroscopies together with the qPCR assay, shedding new light on the mechanisms governing folliculogenesis.

FTIRM analysis was first carried out on living GCs, by using a specific IR transparent microfluidic device which maintained cells in physiological conditions. The same samples were also analysed after air-dehydration, in

order to test the effects induced by this procedure on lipids and proteins structure and conformation. The one-to-one correlation study performed revealed that the air-drying procedure does not significantly affect the consistency and reliability of the spectral data: hence, the air-dehydration of GCs can be considered a satisfactory procedure for the FTIRM study of these cells.

Another important issue addressed in this PhD project was whether the metabolic processes of GCs could be affected by *in vitro* culture procedures. FTIRM analysis of cultured GCs pointed out significant changes in lipid metabolism, probably due to the absence of the companion oocyte and in turn of the bidirectional cross talking between germinal and somatic cells.

Several aspects related to the impairment of GCs functions by endogenous and exogenous factors were also analysed. The first important topic discussed was the role played by age in GCs functionality. FTIR Imaging and qPCR analyses, highlighted several signals of age-related stress, which profoundly impact the biochemical composition of GCs, in terms of lipids metabolism and peroxidation, and protein quantity and folding.

Another endogenous factor which could impairs GCs functionality is ovarian endometriosis. The modulation of GCs endocannabinoid system highlighted by qPCR, suggests a novel molecular network throughout endometriosis affects GCs metabolism. These findings were confirmed by FTIRM and RMS tools, shedding new light on the alteration induced by ovarian endometriosis on GCs metabolism, biochemical composition, and cell

death/survival, not only on the ovary presenting endometriotic lesions, but also on the contralateral one, considered “healthy”. These results suggest that endometriosis acts not only through a paracrine/autocrine signalling, but also through an endocrine one, hence impairing the overall ovarian functions.

BPA and DGB, chemical compounds widely used as plasticizers, were investigated as possible exogenous factors affecting GCs functions. FTIRM analysis of GCs treated with BPA confirmed the well-known negative effects of this compound on follicular cells, and moreover advanced the knowledge of the mechanisms by which it disturbs the biomolecular building of such important cells. Conversely, almost nothing is known about the effects of DGB; the results obtained by this preliminary study suggested the ability of this compound to alter, even if throughout different molecular pathways than BPA, the biochemical composition of GCs. The lack of information about DGB biological activity and our preliminary results, make it imperative to further assess at biological level this and other new chemicals, before their employment in everyday objects.

In conclusion, the overall results of the present PhD project show that vibrational spectroscopies can provide precious information, confirmed and enriched by qPCR analyses, about human Granulosa cells: hence, these techniques have been revealed to be valuable tools for basic research studies in the field of reproductive biology, and also for targeted and applied studies in biomedicine.

ACKNOWLEDGEMENTS

First and foremost, I want to thank my supervisor Elisabetta Giorgini. It has been an honour to be her first PhD student. She introduced me to the fascinating world of molecular spectroscopy, teaching me everything she knows with enthusiasm, patience and warmth, and supporting me during the rollercoaster of my PhD.

Profound gratitude goes to Oliana Carnevali, who was the first to believe in my potential and who was a truly devoted mentor during all the years of my PhD, and still to this day.

I am also hugely appreciative to Giorgia Gioacchini, whose joy and enthusiasm for research was contagious and motivational, even during tough times of my PhD. She was an indefatigable proof-reader, advisor and guide for me.

I gratefully acknowledge Andrea Borini, for believing in the project I worked on during my PhD, and hence for letting me discover the amazing and challenging world of Reproductive Biology.

I want to acknowledge the flamboyant Francesca Maradonna, whose perpetual energy, personal support and scientific expertise helped me a lot in many aspects, from planning the work, to understanding situations and people.

Special mention to Chiara Piccinetti, whose strength, love, friendship, joy, generosity and warmth, make her one of the most inspiring people I've ever met.

My acknowledgements travel up to Ireland, in particular to the FOCAS Institute of DIT, directed by the polite, generous and open-minded Hugh Byrne. He welcomed me in his group, teaching me everything I needed for my PhD, and even more, as a spectroscopist and also as a person.

I am grateful to all the people from the Laboratory of Developmental and Reproductive Biology, who shared with me these tough but irreplaceable years. We experienced together all the ups and downs of our work, the shared happiness of success and the sadness of failure.

Finally, but by no means least, a million thanks go to mum, dad and Gianluca for the unbelievable support. They are the most important people in my world and I dedicate this thesis to them.